Università degli Studi di Ferrara
Facoltà di Scienze Matematiche, Fisiche e Naturali
Corso di Dottorato di Ricerca in Fisica, XVIII Ciclo

SUPERCONDUCTING MAGNETIC SYSTEMS FOR HIGH ENERGY POLARIZED PHYSICS

Dottorando:

MARCO STATERA

Tutore:

Prof. PAOLA FERRETTI DALPIAZ

Anni 2003/2005

Contents

Introduction

The experimental program to investigate the nucleon structure, using polarized beams and targets, is giving many interesting results,[1, 2, 3, 4, 5, 6, 7] and opens new perspectives [8, 9]. Since more then ten years the gas polarized target group of the Ferrara University and INFN is active in the field. At present the group is involved in the HERMES experiment and in the PAX and SMILE projects [8, 9]. In this frame, my personal responsibility concern the requested magnetic systems.

In particular, this thesis work has been dedicated to the interaction region of the new generation experiments using internal storage cell . The items addressed concern both the gas polarized target and the tracking magnet, that are strictly connected. The gas target consist of the combination of a polarized atomic source, and a storage cell coaxial with the beam. In the atomic source, a system of small sextupoles polarizes and focalizes the atoms, that are injected in the storage cell. The cell is immersed in a holding magnetic field that assures longitudinal or transverse polarization. The field of the tracking magnet, surrounding the interaction region, must be null where the cell is located, to keep the polarization in the cell.

The choice to use superconducting magnets offer many advantages that are discussed in the thesis.

Polarized gaseous targets internal to the beam lines has now become a mature technology. They provide fast-reversible high-degree polarization without dilution by non-polarizable material. However, the luminosity until now achieved with such targets is lower than the one reached with solid targets and extracted beams, see Chapter 1 of this thesis for more details. The increase in density of the target is the goal for the next generation of polarized high-energy physics experiments at accelerators.

The design of a superconducting atomic beam source, able to increase by roughly one order of magnitude the intensity of polarized gaseous targets is reported in Chapter 1.

With an enhanced atomic flux the beam attenuation may become a severe issue. For instance, the focalizing system should cope with the increase pressure due to the defocalized flux component. An original solution is presented using the cryostat of the superconducting magnets as a cryopump to increase the evacuation capability of the system

Atomic beam source of high intensity require focalizing system of great acceptance and large field gradients, reachable only with superconducting multipoles.

The thesis work comprises the design, commissioning and operation of a cryogenic test bench for mapping the field of small superconducting multipolar magnets in working conditions, at liquid He temperature and full current. Such a device,unique of this type, is necessary to test magnets like the one manufactured in Ferrara where an iron core was added to the coils to enhance the maximum field at the pole. This activity is reported in Chapter 2.

As a part of this thesis work, the preliminary studies about the feasibility of the

magnetic system of the PAX experiment are presented in Chapter 3. The magnet system of the spectrometer of the detector should not limit the performances of the particle identification detectors or degrade the target and beam polarizations. Original solutions has to be met to address these stringent requirements. The proposed system is a compact superconducting toroid for tracking complemented by a couple of Helmholtz coils for the holding field of the target polarization.

I have profited for this item of the experience acquired working on the recoil detector magnet of the HERMES experiment. There it has been my responsibility the revision of the inlet and outlet He-lines of the existing cryostat, the design of the cryogenic system up to the cryostat and of a reliable interlock system, and the definition of the best working parameters, as can be seen in chapter 4.

The PAX physics program, at the core of which is the realization of a polarized antiproton beam, is briefly described in Appendix A, while as an useful reference, the HERMES target is presented in Appendix B.

Chapter 1

A high intensity superconducting atomic beam source

The next generation of polarized high energy physics experiments accelerators employing internal targets, like PAX, require a significant increase in density of the target. In an atomic beam source (ABS) electron polarization is obtained from Stern-Gerlach separation by sextupole magnets and then transferred to nuclei by means of RF transitions. The Università di Ferrara and INFN group is developing a new ABS characterized by an high intensity beam, using small bore ($5 - 10$ cm) high pole tip field (6 T) superconducting sextupoles. Preliminary studies have been presented at Applied Superconductivity Conference 2004 [10] indicate that such systems would allow a sizable increase in the source intensity, up to an order of magnitude.

1.1 Introduction

High energy physics experiments that study the spin composition of nucleons require a target of dense spin-polarized material. Solid targets with extracted beams has been extensively used in the past, since they provide high luminosity thanks to the high-density, of the order of 10^{23} $\frac{\text{at}}{\text{cm}^2}$. These targets are characterized by a low fraction of polarized nuclear targets respect to the total number of nuclei, called dilution factor f, which largely reduces the effective target polarization and spoils the luminosity performances. So far the maximum dilution factor, achieved for ^6LiD target, is of the order of only $f \approx 0.5$ [11]. Moreover the inversion of target polarization requires hours. Over the last 10 years, the combination of an atomic beam source (ABS) and a storage cell internal to the beam line has provided a remarkably stable and reliable target of polarized atomic gas for several experiments [12]. Such targets has no dilution ($f = 1$) and the polarization can be reversed in milliseconds. However, so far the low density of gaseous targets could be only partially compensated by the multiple interaction with the stored beam, thus limiting the achievable luminosity.

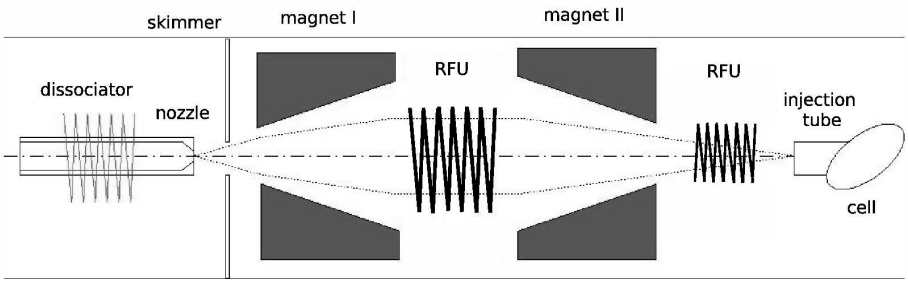

Figure 1.1: Scheme of an atomic beam source. From left to right: the dissociator, the nozzle, focussing sextupolar magnets, Radio Frequency Units, injection tube and the accumulation cell.

The next generation of spin experiments requires a significant increase in luminosity which is proportional to the rate of atoms collected at the end of the ABS into the injection tube of the accumulation cell. For instance the PAX project, described in Appendix A, requires high intensity targets to efficiently polarize antiproton beam by the spin-filtering method and to achieve large enough luminosity to measure the Drell-Yan process in fixed-target configuration. Recent studies seems to suggest that the intensity of current ABS systems (see Fig. 1.1) is limited by beam attenuation [13, 14]. A maximum in intensity is observed while increasing the input flux that corresponds to an upper limit to the density of the beam, above which the beam starts to be destroyed by beam-beam interaction called Intra Beam Scattering. Since the density has an upper limit, the way to increase the intensity would be to enlarge the focussing system inner diameter to increase its acceptance, at the same time keeping a similar or better focussing efficiency and comparable beam density with respect to the existing systems. This approach requires superconducting sextupoles with high field gradients and promises roughly a factor of 10 increase in the beam intensity and thus in target density. In this Chapter the conceptual design of a superconducting ABS is presented. The technological issues of such a device are discussed in detail.

1.2 Polarized Atomic Beam Sources

An atomic beam source begins with a molecular gas, typically hydrogen or deuterium, (we will refer to only hydrogen from now on), flowing inside a glass vessel within a high-frequency cavity. The discharge produced by the cavity dissociates the molecules into atoms. The gas of neutral atoms passes from the glass tube into vacuum through a narrow tube called a nozzle. The gas rapidly expands as it leaves the nozzle, reaching an average speed in the range 1000-2000 m/s, and can be treated like a point source. A skimmer defines a beam of atoms by selecting a small solid angle of the point source for entrance into the magnet system. The beam intensity of the ABS, which corresponds to

the flux of atoms entering the injection tube (see Fig. 1.1), can be estimated as

$$I_{ABS} = \frac{k}{N_H}(2\ \alpha Q_i)\ f\ t(1-A) \tag{1.1}$$

where k is the number of focussed hydrogen hyperfine states (1 or 2) over the total number of states, $N_H = 4$ in case of hydrogen, α is fraction of atoms dissociated over the total amount of atoms exiting the nozzle, Q_i the input flux inside the dissociator, f the ratio of atoms that pass through the skimmer, t the fraction of atoms focussed into the injection tube by the focussing system (called magnet transmission factor) and A the beam attenuation.

1.2.1 Focussing system

The focussing efficiency of an ABS depends on many geometrical factors, one of the most importance is the acceptance of the first sextupole magnet. The parameter characterizing a magnet are the radius, the maximum value of the magnetic field and the tapering of the inner bore. The maximum magnetic field value is on the pole and is called pole tip field B_{pt}. A good estimate of a single magnet acceptance is obtained with a simplified model, consisting of a cylindrical magnet and a point source located on the axis at the magnet entrance [15]: the accepted solid angle at a radius r is

$$\Omega = \pi \frac{2\,\mu_B}{mv^2} B_{pt} \left(1 - \frac{r}{R}\right) \tag{1.2}$$

where μ is the atom's magnetic moment, m and v the particle's mass and velocity, B_{pt} is the pole tip field of the magnet, R is the magnet radius and r the radius at which the particle enters the magnet. Averaging the acceptance over the magnet radius and integrating over velocity one obtains the following equation

$$\bar{\Omega} = \frac{1}{R}\int_0^R \int_0^\infty \Omega f(v) dv dr = a\frac{\mu B_{pt}}{kT_b} \tag{1.3}$$

where $f(v)$ is the velocity distribution, approximated by a Maxwellian distribution, a is a geometrical constant ($\frac{2\pi}{3} = 2.09$ for sextupoles), k is the Boltzmann's constant and T_b the beam temperature (proportional to the width of the velocity distribution). According to equation 1.3, the largest acceptance is obtained with the highest pole tip field. It has to be pointed out that while equation 1.3 is applicable to a single (cylindrical) magnet, it might not reliably predict the situation in a practical focussing system because the geometrical situation strongly influence the beam intensity. Results from a focussing systems designed by ray-tracking calculation will be shown in Section 1.3.2.

When the beam of atoms traverses a magnetic field gradient, the atoms are separated by their spin. Sextupoles have the particular characteristic that, for a given velocity,

an atom leaving a point like source and entering the magnet is focused onto an image point independent of its initial direction. This is true in the case of a magnet with zero longitudinal length and no fringe field, acting as a optical lens. The magnetic field of an ideal sextupole is given by

$$\begin{aligned} B_r(r,\theta) &= \frac{B_{pt}}{R_{pt}^2} r^2 \sin 3\theta \\ B_\theta(r,\theta) &= \frac{B_{pt}}{R_{pt}^2} r^2 \cos 3\theta \end{aligned} \tag{1.4}$$

where B_{pt} is the pole tip field and R_{pt} is the corresponding radius. The force that focuses or defocuses atoms with magnetic moment $\pm\mu$ is

$$\vec{F} = \pm\mu \frac{\partial |\vec{B}|}{\partial r} = \pm\mu \frac{2B_{pt}}{R_{pt}^2} r\hat{r} \tag{1.5}$$

and atoms whose spin is parallel to the field are pushed radially inward and those whose spin is anti-parallel to the field are pushed radially outward. The beam has a large range of velocities and the magnets has to be designed to focus as much of this distribution as possible into the collection tube.

1.2.2 Beam attenuation

The beam attenuation in an atomic beam has two sources: the interaction of the beam particles with the molecules in the vacuum (called Rest Gas Attenuation) and with other beam particle (called Intra Beam Scattering).

The rest gas attenuation can be estimated by

$$S_{RG}(z) = e^{-\frac{\sigma_{H-H_2}}{k\,T_{RG}} \int_0^z p_{RG}(l)dl} \tag{1.6}$$

where σ_{H-H_2} is the cross section between beam's atomic hydrogen and molecular hydrogen from the residual gas inside the chamber, k is the Boltzmann constant, T_{RG} is the rest gas temperature, z is the distance from the nozzle (at z=0) and p_{RG} is the rest gas pressure. The rest gas attenuation is a quite well known phenomenon [16].

In an atomic beam source the pressure inside the focussing volume have to be kept below 10^{-4} because of rest gas attenuation. In the systems using permanent magnets it is possible to subdivide the magnets into subunits to improve pumping inside the magnet's inner bore, where the defocussed atoms hitting the magnets became rest gas. In a superconducting ABS [1] it is possible to exploit the cold surfaces of the cryostat itself to cryopump the hydrogen (see Section 1.5).

[1] In the apparatus built at Novosibirsk, the superconducting magnets are subdivided to allow pumping similar to the standard systems (Fig. 1.7)

The intra beam scattering has been neglected in most atomic beam source designs until now since it was assumed to be negligible due to the low beam densities. With the increase of beam density, especially in the focussing region, the intra beam scattering could affect the final beam intensity. Studies on a model for the intra beam scattering [14], conceptually similar to the one used for the rest gas attenuation, are under development. The parameters used for the model are the cross section between beam's atomic hydrogen particles σ_{H-H}, the relative velocity between the hydrogen particles Δv, the mean beam velocity v_B, and the effective transversal beam density n; the beam attenuation is then given by

$$S_{IB} = e^{-\sigma_{H-H}\frac{\Delta v}{v_b}\int_0^z n(l)dl} \tag{1.7}$$

Direct measurements of σ_{H-H} at the atomic beams energies are needed. First promising results on the estimation of the effective transversal beam density comparing simulations results with existing systems is presented in [14].

1.2.3 Nozzle regeneration

A small amount of oxygen is introduced into the ABS dissociator to improve hydrogen atomic dissociation. This causes water formation inside the dissociator and ice deposition inside the nozzle. When the ice layer, growing with time, partially occludes the nozzle aperture, the dissociator performances start to degrade. The nozzle has to be warmed up regularly to room temperature to let the ice to evaporate. This operation, called nozzle regeneration, requires approximatively 3-4 hours. The continuous running time for an ABS does not exceed 24-48 hours, which is the typical time interval between two nozzle regenerations.

1.3 The Ferrara SC-ABS

The intensity of current ABS systems seems to be limited by beam attenuation. As mentioned above, since the density has an upper limit, another way to increase the intensity is to increase the transverse dimension of the beam focussed in the collection (injection) tube while keeping the density constant. In other words the beam physical dimension can be increased, at the same time leaving the particle density constant, by increasing the inner diameter of the focussing system.

The use of superconducting sextupoles with their high pole tip fields respect to the permanent magnets' ones lets the ABS designer to increase both the total number of particles entering the focussing system and the number of focussed particles, thus increasing the intensity. The magnet diameter and the pole tip field, the magnet length, the magnet tapering and the distance between magnets are the main parameters for the focussing system design. All these parameters influence the beam focussing. Increasing

the magnets diameter, increases the number of atoms entering the focussing system. The focussing force (the field gradient) has to be adequate to deviate and to focus the atoms. The tapering have to follow as much as possible the beam expansion and the focussing to improve the system efficiency.

Note that in case of superconducting magnets the current supplied and thus the maximum pole tip field, the gradient and the focussing force can be varied. This is a real tuning of intensity and focus position that is not possible with permanent magnets systems.

An ABS design has many constraints. The ABS needs to allocate radio-frequency transitions for the spin selection, the distance between nozzle and focussing system has to allow the beam to develop. Concerning a final design of the ABS for an experiment, the total length and diameter have to be compatible with the available space taking into account the volume occupied by cryostat and power supplies in case of superconducting magnets.

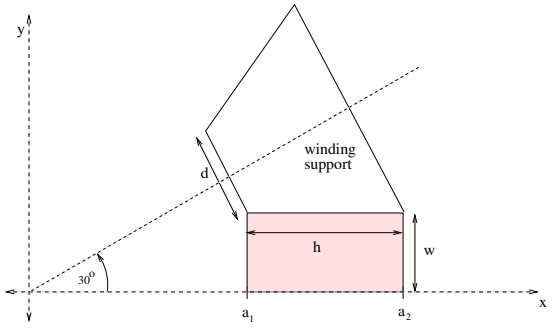

Figure 1.2: The sextupole superconducting magnets coils geometry. A part of a transversal cross section is shown. The coil is the dark area. a1 is the minimum radius for the coil, a2 is the maximum one. d is the minimum pole (winding support) dimension. When a1 increases, if d is constant, coils' width w increases, the ideal maximum is reached when d=0.

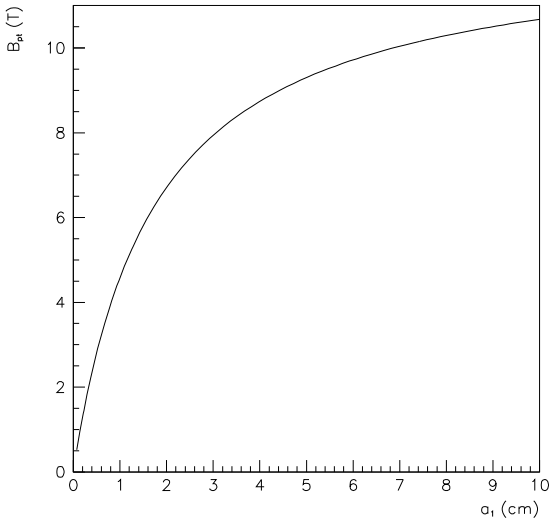

Figure 1.3: Maximum pole tip field in function of the coil radius (see fig. 1.2). The plot is in the limit case in which d=0 and the coil has no limitations in h values. The wire considered is the NbTi available for tests in Ferrara.

The pumping of the non focussed part of the beam is a critical issue. Since a considerable quantity of not focussed hydrogen atoms stick on the cryostat's cold surfaces, a regeneration, i.e. the warming up of those surfaces and then the pumping of the evaporated hydrogen, will be needed. To be regenerated, the surfaces have to be warmed up by only few kelvin since the hydrogen saturation pressure increase rapidly with temperature. The nozzle and cryostat cold surfaces regeneration times should be comparable to

maximize the running time. Finally the running time, and the regeneration times in case of superconducting systems, have to be compatible with the accelerated beam duty cycle.

The reliability is an important parameter during data taking, when several hours of good working conditions are usually requested. While the current permanent magnet atomic beam sources have reached a very high reliability, R&D work is still needed in the case of superconducting ABS to obtain comparable performances.

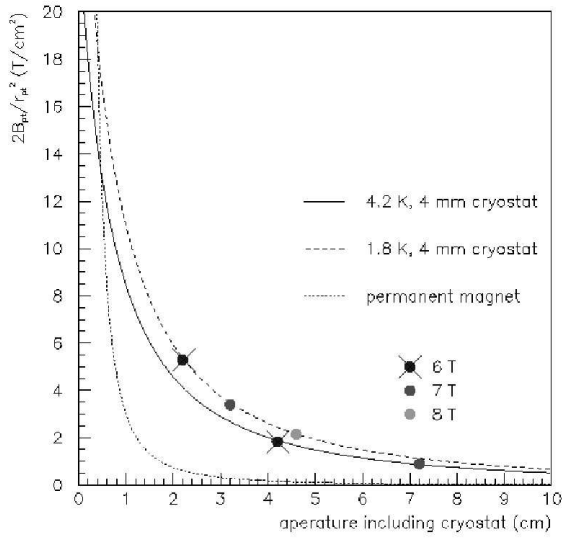

Figure 1.4: A comparison of the gradient of a sextupole field as a function of the physical inner aperture. The critical current density $J_c = 1.2\,\mathrm{kA/mm^2}$ is the current density inside the superconducting phase. Permanent sextupole magnets have a fixed pole tip field of 1.5 T while the maximum pole tip field for a superconducting sextupole magnet increases with aperture.

1.3.1 Superconducting magnets

Permanent sextupoles have a fixed pole tip field around 1.5 T, independent of the magnet's aperture, so that the radial gradient is fixed by the inner radius R_{pt} (see Eq. 1.5) and the acceptance can be improved only by lowering the beam temperature (see Eq. 1.3). Instead, the maximum pole tip field for a superconducting sextupole increases with the radius. The reason is that increasing the inner radius, the space available for the superconducting wire coil increases (see Fig. 1.2), and so does the total current. As a consequence the pole tip field and the maximum field on the coils (roughly 1.5 T above the pole tip field) increases at a given maximum current density. Figure 1.3 shows the maximum pole tip field in case of zero thickness pole and no limits in coil height. The wire considered is the one available for tests in Ferrara laboratory. Several coils of NbTi wire, with engineering critical current

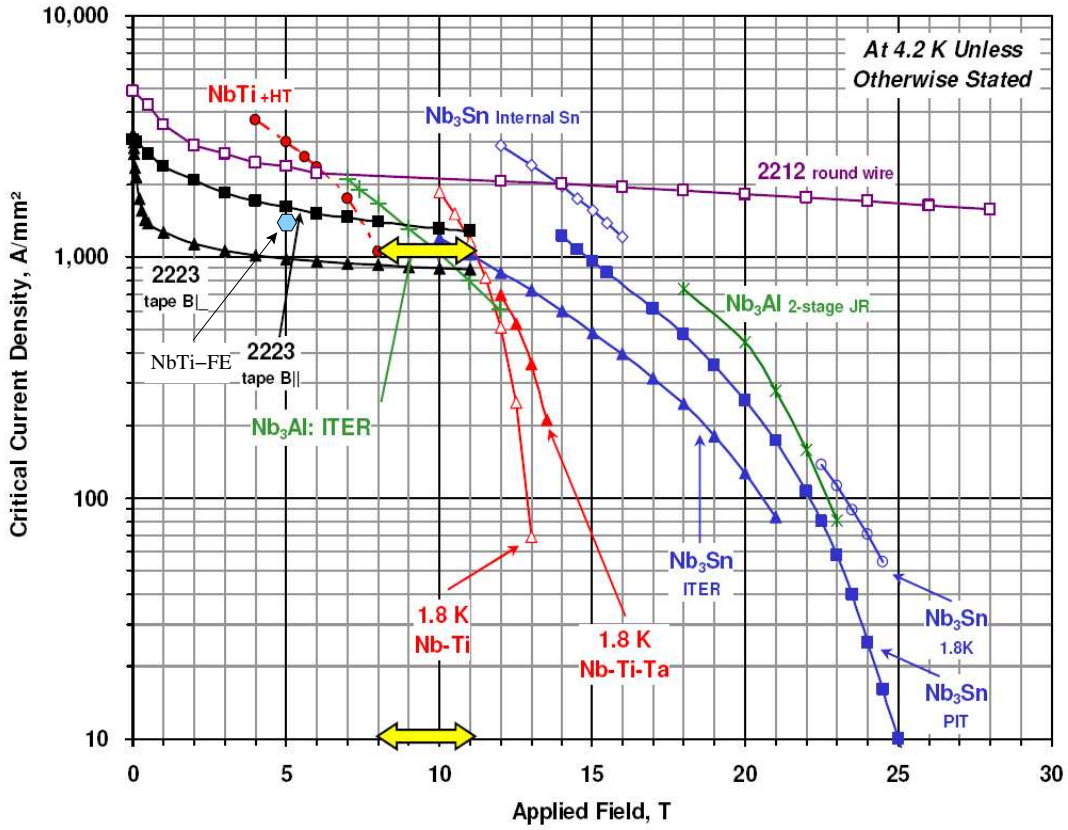

Figure 1.5: Performance comparison [17] for different superconducting wires.In particular NbTi, Nb_3Sn maximum working conditions for different working processes are plotted. For NbTi is reported the improvement in critical current due to the cool down to 1.8 K. MgB_2 Bi-2212 modified tape and wire critical currents are also shown. The critical current of the NbTi wire available for tests in Ferrara (NbTi-FE) is also plotted.

(current density averaged over the total wire cross section) $J_e = 0.7$ kA/mm^2 at 4.2 K and 5 T, 1.2 $\times$ 0.75 mm^2 cross section and copper over superconductor mass ratio equal to 1.6, have been acquired by Ferrara University from Europa Metalli in 1990. The wire was partially used to build a first superconducting prototype described in Section 1.4. A comparison between permanent and superconducting sextupoles' gradient field is shown in Figure 1.4, the wire used for the calculation regarding superconducting coils is the NbTi Ferrara one.

For small magnets' diameters (below 1.5 cm diameter), the permanent magnet sextupole focussing force is higher. As shown in Figure 1.4, the focussing force of superconducting magnets is several times higher when the diameter is greater than 1.5 cm.

The superconducting magnets using low temperature superconductors require a cryostat to reduce the cooling liquids consumption and ensure a stable and safe operation

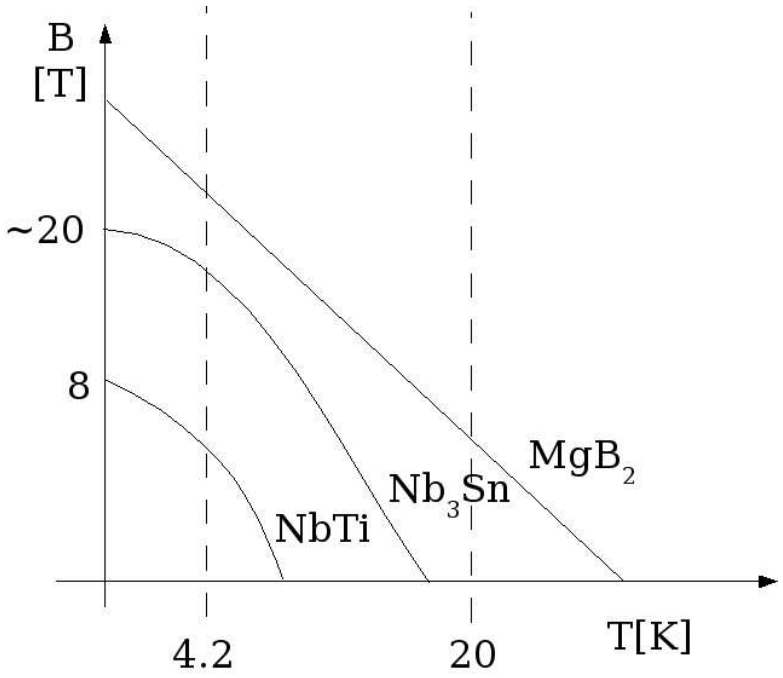

Figure 1.6: Critical field for NbTi, Nb_3Sn and MgB_2 superconductors. Liquid helium and oxygen temperatures are indicated by vertical lines, respectively 4.2 K and 20 K.

for the magnet keeping it in contact with the cooling liquid. In the case of an ABS the beam requires a vacuum better than 10^{-4} mbar to reduce beam attenuation phenomena. The same vacuum can be used for the cryostat thermal insulation. In the inner part of the magnet, a cryostat reduces both the inner radius and thus the maximum field in the focussing region where the beam develops. A cryostat as much thin as possible is foreseen to increase the geometrical acceptance in the inner part. The solution chosen is to use a total 4 mm thick cryostat made up of a liquid layer of helium and a less than a mm thick stainless steel vessel.

The superconducting materials technology is increasing the wires' performance, by improved production methods or new materials. The critical current densities J_c (averaged over only the superconducting material cross section) of several materials are plot in Figure 1.5. These data are obtained using wire's strands in an external magnetic field. The NbTi wire available at Ferrara has critical current $J_c = 1.2$ kA/mm^2 at a 5 T magnetic field. Actually NbTi superconducting wires working up to $J_c = 1.5$ kA/mm^2 are available applying a specific heat treatment (NbTi-HT in Fig 1.5). The maximum achievable magnetic field increases by about 3 T, at a given critical current, when a Ta modified NbTi wire cooled at superfluid helium temperature is used. In the figure, the arrows indicate the 3 T increase obtained at $J_c = 1\,\mathrm{kA/mm^2}$. Higher critical current densities can be reached by Nb_3Sn wires. As an example at 13 T the Nb_3Sn wire produced

by internal tin process [17] has 1.8 kA/mm^2 maximum critical density increase respect to $NbTi-Ta$ wire at 1.8 K. The Nb_3Sn technology is still not mature for small multipolar magnets because there are problems of instability at fields below 12 T. MgB_2 Bi-2212 modified wires are under development and represent an interesting alternative to $NbTi$ for magnet fields below 7 T and to Nb_3Sn for magnet fields above 14 T. to Nb_3Sn. This material has also interesting critical current densities at higher temperature than liquid helium as can be seen in Figure 1.6. Until now, for small superconducting sextupoles the NbTi technology is more reliable and several times cheaper than the others. An important parameter is the minimum bending radius, very important for the small sextupoles coils winding. Actually NbTi wires only provides reliable performance at 1 mm bending radius, which is typical for small sextupoles.

1.3.2 Ray-tracking simulations

An algorithm developed at CERN for ray tracing has been expanded in Ferrara. The code has been tested with the data of existing devices: the permanent-magnet ABS of HERMES and Wisconsin University, and the superconducting-magnet ABS of Novosibirsk. Some geometrical parameters together with measured and calculated intensity of existing systems are listed in Table 1.1. The intensity predictions of the HERMES and Wisconsin (now in Ferrara laboratories) atomic beam sources are compatible with the measured ones and the difference between the values can be attributed to beam attenuation.

In the case of Novosibirsk ABS, the low throughput implies low beam density in the focussing volume, so that the difference between calculated (without attenuation) and the measured values can be attributed to rest gas attenuation or to the formation of hydrogen solid layers on the magnets. The Novosibirsk system is designed to pump out not focussed particles by splitting the magnets (Fig. 1.7), as usually done in the permanent magnet systems, so that a much higher rest gas attenuation with respect to standard systems is not expected. However, the superconducting magnet built for this ABS are relatively small and the formation of solid layers on first magnet surfaces can affect their acceptance and thus the beam intensity.

The ray-tracking algorithm is used to optimize the geometry of the magnets.

In Figure 1.7, two existing systems are sketched along with the Ferrara superconducting ABS design to demonstrate how the use of SC magnets increases the focussing system acceptance. The HERMES ABS (see Appendix B) is constructed with permanent sextupoles and can be considered the standard for such systems. The Novosibirsk system consist of superconducting sextupoles with entrance diameter and maximum pole tip field increased by a factor around 2 with respect to the HERMES ABS, i.e. the larger magnets have a pole tip field of 4.3 T. This ABS has an input flux 2.5 times lower than the HERMES one but similar intensity thanks to the improved focussing system using superconducting magnets, see Table 1.1.

	Hermes	NOVOS	WISC	FE
$Q_{in}(mbar \cdot l/s)$	1.5	0.6	1.7	3.0
α	0.82	0.90	0.75	0.6
B_{pt} (T)	1.5	3.2	1.5	6.0
d_{mag}	0.86	1.4	1.04	2.0
v_{drift} (m/s)	1953	1750	1494	1250
$T_{beam}(K)$	25.0	30.0	16.5	15.0
$length$ (m)	1.16	1.4	0.99	1.0
$D_{ct}(cm)$	1.0	2.0	1.0	2.0
Q_{calc} (at/s)	6.8 10^{16}	10.6 10^{16}	9.5 10^{16}	100 10^{16}
Q_{ct} (at/s) meas	6.5 10^{16}	6.7 10^{16}	7.8 10^{16}	

Table 1.1: Comparison between some existing atomic beam sources and the Ferrara design parameters and simulation results. The magnet diameter in the table is the minimum one, at the entrance of the focussed system. The calculated intensity is reported without attenuation.

1.3.3 Conceptual Design

Following the above indication, the Ferrara design opens the magnet system even more, and thus requires higher pole tip fields to maintain a comparable focusing gradient. The Ferrara ABS design, the skimmer diameter, the diameter and tapering of the magnets (especially for the first one) and the cryostat have been optimized taking into account the issue of the beam attenuation. In particular the cryostat is used as a cryopump, and an additional pumping cold surface is added between the two helium vessels containing the magnets. In the Ferrara design, the inner diameter of the magnets is greater than the Novosibirsk ABS, so that the solid layer formation influence on beam intensity is lower. The designed system (see Fig. 1.7 1.8 and 1.9), with an input flux only doubled with respect to the HERMES one and a focussing system using big inner bore superconducting magnets, reaches an expected intensity 10 times higher than the HERMES one, see Table 1.1 and Figure 1.9. The estimated intensity of the system is 10^{18} at/s into a 2 cm diameter compression tube.

The magnets of the project (Fig. 1.8 and 1.9) has been designed with the maximum pole tip field achievable using the NbTi wires available for test Ferrara, which is 5-6 T at 4.2 K and 8-9 T at 1.8 K. The upstream magnet is 40 cm long and the minimum and maximum diameter are 2 cm and 10 cm respectively. The minimum diameter of the first magnet implies a pole width (d in Fig. 1.2) reduced to 2 mm, forcing the wire to bend with a radius of 1 mm at the base of the support. Such a winding of the tapered magnet is challenging. The downstream magnet is 30 cm long and the maximum and minimum diameter are 10 cm and 8 cm, respectively. The magnets outer diameters are roughly 23 cm.

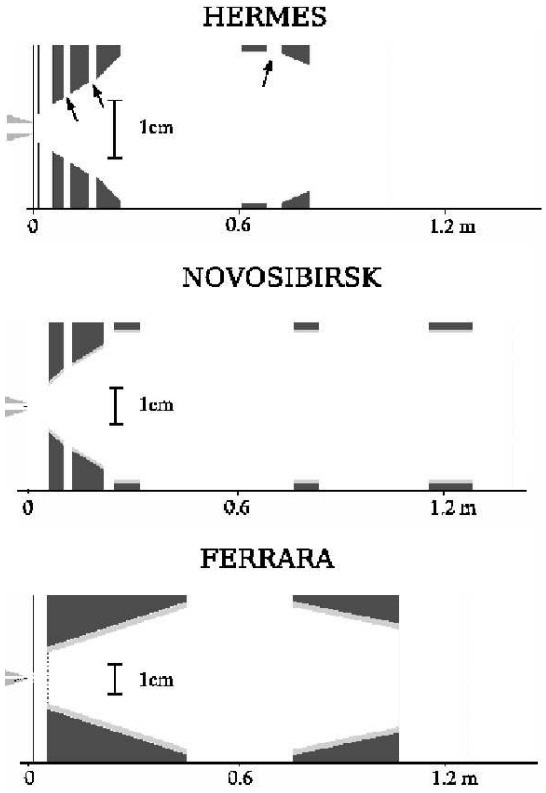

Figure 1.7: The geometry of the Ferrara SC-ABS, compared to the HERMES permanent magnet ABS and SC Novosibirsk ones. The division of permanent magnets in HERMES' ABS is due to pumping issues (arrows), while in NOVOSIBIRSK's ABS the aim is to follow the beam envelope and maximize the pole tip field, limited by the smaller inner diameter of the magnet.

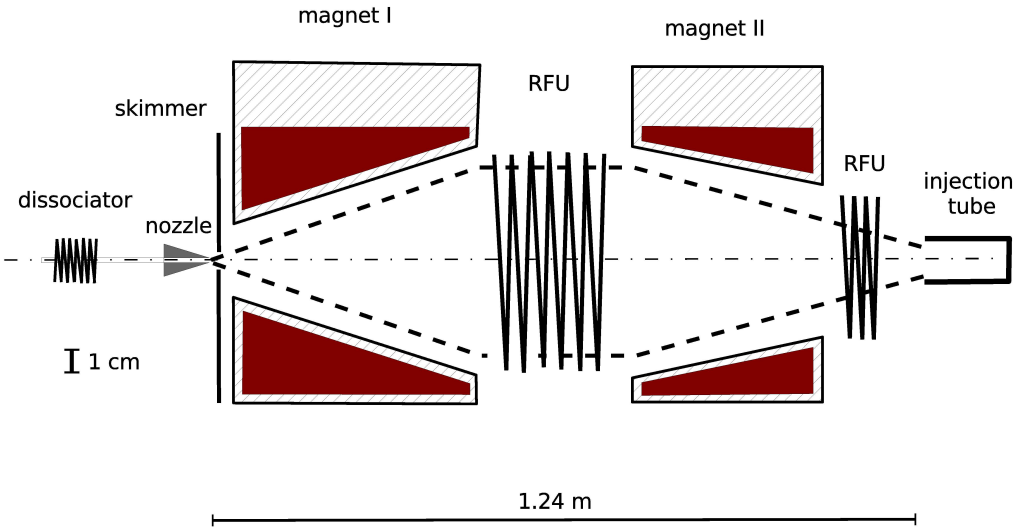

Figure 1.8: Scheme of the designed high intensity Atomic Beam Source based on superconducting magnets. The helium vessel surrounding the magnets are drawn.

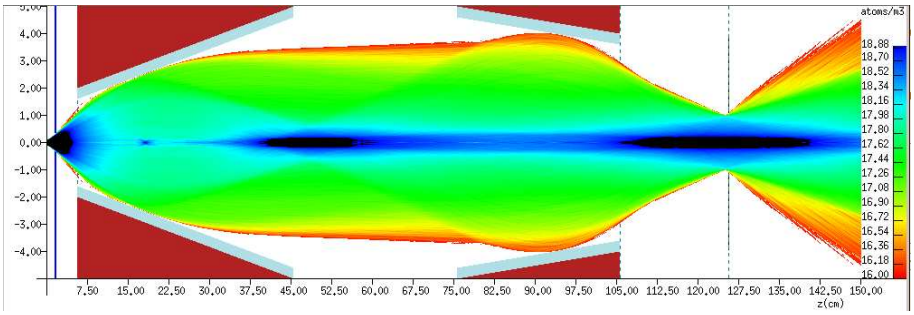

Figure 1.9: Focussed beam density, the unfocussed particle are not plotted. The vertical scale is in cm, while the horizontal one in dm. In the simulation a 4 mm cryostat thickness was considered, a cold surface is placed at r=11.5 mm, the system counts the number of atoms colliding on the cold surfaces to evaluate the solid hydrogen buildup on cold surfaces. The nozzle diameter is 2 mm.

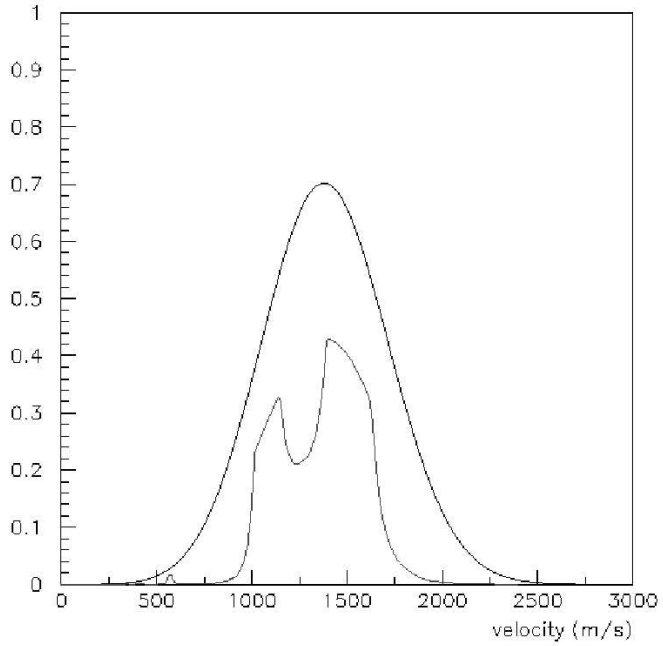

Figure 1.10: Velocity distribution (upper curve) and selected velocities (lower curve) for the Ferrara SC ABS using a 60 K *nozzle.*

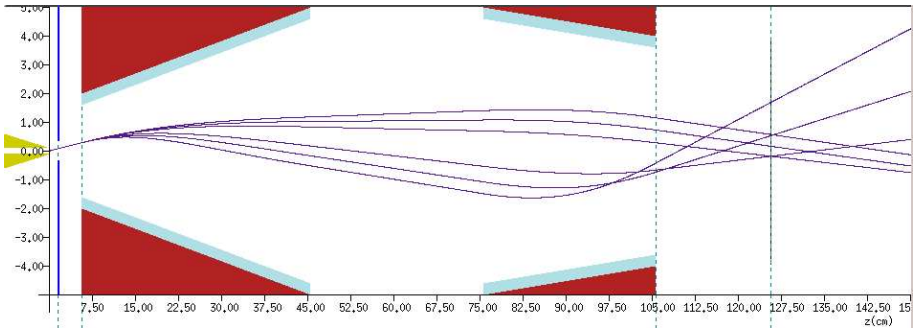

Figure 1.11: Ray tracing of some focussed particles. The tracks have same angle exiting from the nozzle, but different velocities. In this figure the presence of two focussed 'harmonics', depending from velocity, is clear. The lower energy atoms are strongly bent inside the first magnet, they represent the first peak in fig.1.10. The higher energy atoms have an almost horizontal trajectory between the two magnets. Both 'harmonics' are focussed in the same region on the beam axis increasing the final intensity.

The distance between the upstream and downstream magnets is critical when different mean velocities have to be focussed. The velocity distribution of the atoms exiting the nozzle cooled at 60 K (solid line) and collected (dashed line) in the 2 cm injection tube is shown in Figure 1.10. The two peaks in the collected distribution show how two velocity ranges are better focussed. The focussed atoms with slower velocity are defined as second focussed harmonic: these atoms with lower energy move along a path crossing once the beam axis between the two magnets (see Fig. 1.11). The distance between the two magnets has been optimized to focus both harmonics in the same point increasing intensity. In particular, both harmonics peaks close to the maximum of the velocity distribution of the beam thanks to the optimization of the magnet geometry.

1.4 Prototype of a superconducting sextupole

A prototype has been constructed in the Ferrara laboratories to match the requirements of the downstream section of a SC-ABS focussing system. The magnet is a sextupole made of six coils of superconducting NbTi wire ($J_e = 0.7$ A/mm^2 and copper over $NbTi$ mass ratio $\frac{Cu}{NbTi} = 1.63$), see [18].

The coils are wound around a steel support with an iron core (often called iron pole) and encased in a cylindrical iron yoke. When the magnet is powered, the iron pole magnetize and add a component to the field external to the coil. This unconventional design is intended to increase the pole tip field of the magnet of about 1 T with minor increase of the field inside the superconducting coils and resultant effect on the critical current. In a tapered magnet, the pole width (d in Fig. 1.2) is not constant since the free space increases with the inner bore radius. As a consequence the pole tip field given by the superconducting coils is not constant but decreases with the rising radius. The contribution added by a iron pole should partially compensate such a behavior.

The coils of the prototype contain 14×22 turns of wire, with a cross section of 19.2×19.5 mm^2. The wire's section is 1.35×0.75 mm^2. Figures 1.12 and 1.13 show the layout of the magnet.

The coils are electrically connected in series by pairs of slabs. Each connection of two coils are fixed mechanically between the slabs pairs by 4 screws. Figure 1.14 shows the connections 1, 2 and 4. The electrical connections of the current leads are shown in Figure 1.15. In this case 3 slabs have been used for each connection, their dimensions are 5 x 40 x 30 mm. The connection is split into two parts: the superconducting wires are connected between the first and second slab whereas the normal conductive part of the current leads is connected between the second and third slab.

The measured inductance at 300 K is 158.4 ± 0.1mH. The magnet was trained in Ferrara, and reached 517 A. The maximum field measured at 517 A was 4.8 T.
The average liquid helium consumption per quench was 5.5 l/quench.

The magnet dimensions were measured (see fig.1.16) by a high precision three dimensional numeric control machine. The bottom holed disk of the magnet was unscrewed

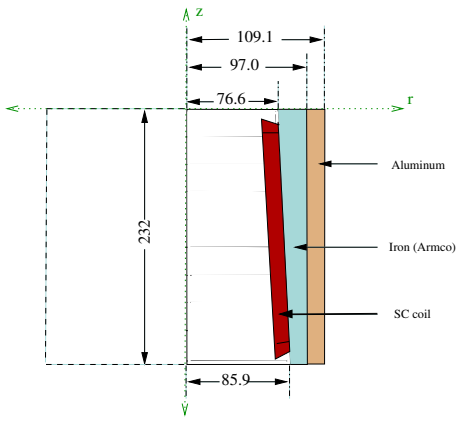

Figure 1.12: The magnet layout in the rz-plane. The coils are hidden by rings of vetronite which hold the coils in place. The magnet is 232 mm long, and the inner bore is tapered with diameter 100-109 mm. All numbers are in mm.

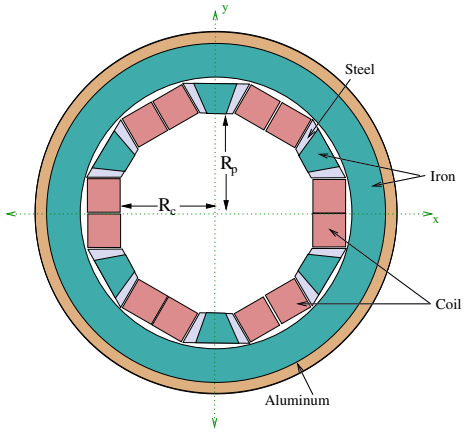

Figure 1.13: A transverse cross section of the prototype superconducting sextupole magnet in the $r\phi$ -plan. In the center of the magnet, the pole is at a radius of $R_p = 50.4$ mm and the coil is at a radius $R_c = 49.7$ mm.

Z mm	x-center mm	y-center mm	diameter cm
89.47	0.177	0.003	10.3830
79.51	0.037	0.069	10.4278

Table 1.2: Inner circumferences measured on the pole tips. The center of the coordinates is the center of the outer aluminum cylinder of the magnet.

and removed so that the reference plane is the bottom of the aluminum outer cylinder (Fig 1.13) i.e. 10 mm above the bottom of the magnet itself.
The outer diameter, several inner points both at the pole and the coils intersection, and thus internal diameters, were measured. The outer cylinder has been measured and used as reference, the axis origin has been set in the center of the outer diameter and at the center of the magnet in vertical direction. The geometrical axis of the outer cylinder is almost coincident with the axis of the coils: the difference is less than 0.18 mm. Two inner circumferences diameters and center with respect to reference are reported in Table 1.2, while points at the mechanical connections of the oils and respective distance from center are reported in Table 1.3.

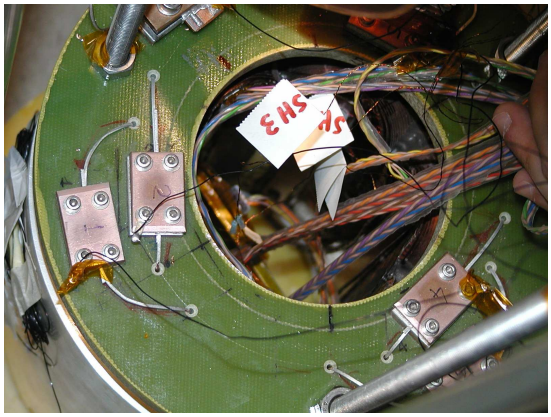

Figure 1.14: Connections between two magnet coils. The six coils are connected in series.

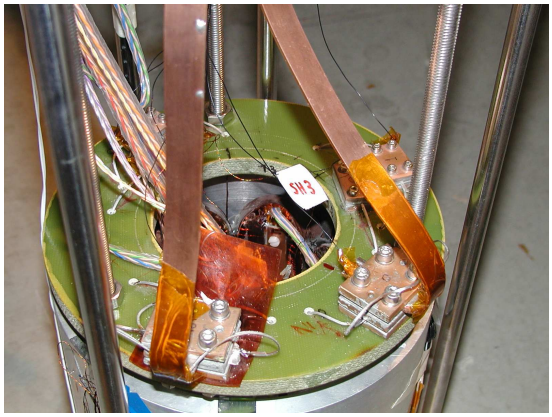

Figure 1.15: Electrical connections of the current leads.

coils	point z=83	radius cm	point z=43	radius cm
1-2	1	48.8	2	50.2
2-3	3	48.5	4	49.7
3-4	5	48.3	6	49.8
4-5	7	48.4	8	49.9
5-6	9	48.4	10	50.1
6-1	11	48.1	12	49.2

Table 1.3: The coils are glued by epoxy resin. The inner radius corresponding to the coils mechanical connection have been measured at z=83 mm and z=43 mm.

1.5 Cryostat conceptual design

The working temperature of the focussing magnet system is between 4.2 K (NPT) and 2.5 K. The magnets have to be maintained at the set temperature inside the helium bath also in case of quench. Decreasing the magnet temperature below 4.2 K improves the magnet's superconducting wire performance and also reduces the base pressure of the system thus increasing the ABS performance as will be shown in this Section. The designed cryogenic system is made up of two cryostats, one per magnet, which are thermally and mechanically connected by a cylindrical surface which is cooled by two helium pipes connected to the helium vessels. Each helium vessel containing the magnet has an inner bore which is the volume in which the atomic beam develops and is focussed. There is no other insulation in the inner side to maximize the free volume for the beam with respect to

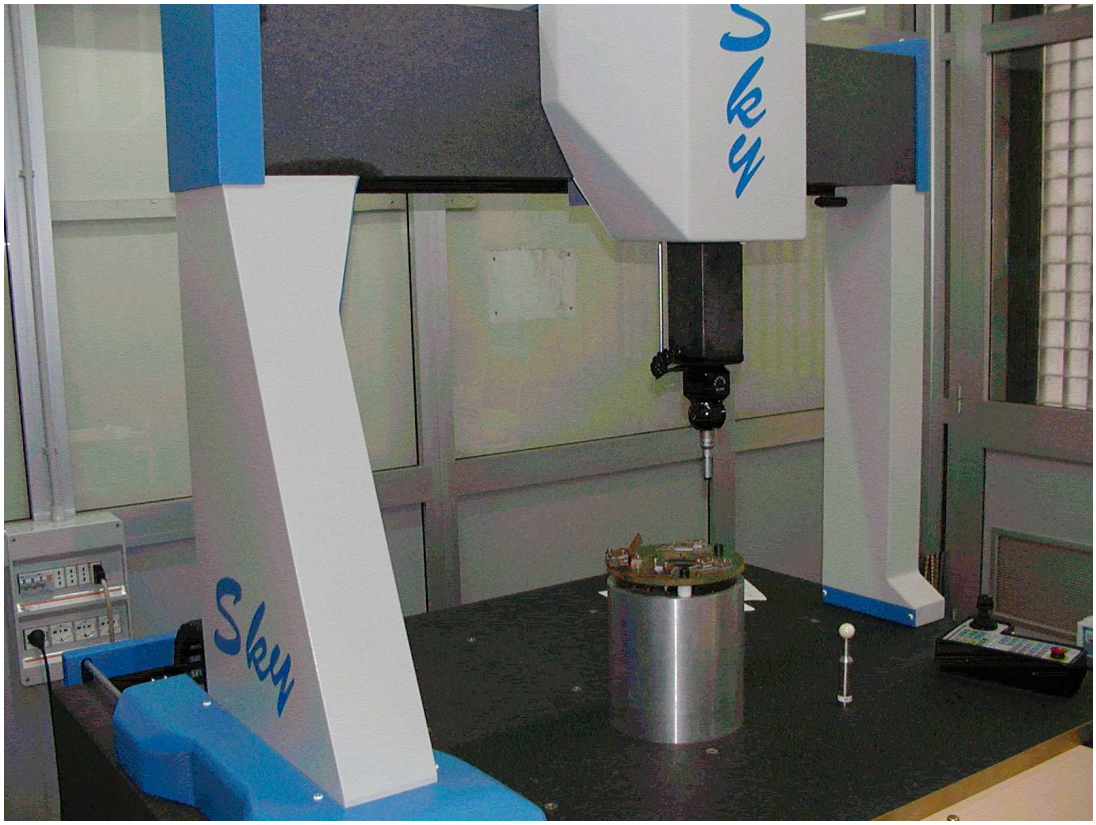

Figure 1.16: A moment of the mechanical measurement of the sextupole magnet.

the magnet diameter. The reason is that increasing the diameter of the magnet, at a given pole tip field, the radial gradient and thus the focussing force on atoms decreases (see Figure 1.4). Externally, the thermal insulation comprises a multilayer insulation (MLI) by alumined mylar, and a liquid nitrogen vessel. The two nitrogen vessels are mechanically and thermally connected by a metallic surface which thermally insulate the inner cylinder connected to the helium vessels. The system is sketched in Figure 1.17. The outer part of the cryostat is a room temperature vacuum chamber, as the usual ones used for the atomic beams. This flexible design allows to change one of the two single cryostats for example in case of failure, maintenance or modification during the R&D without cutting and welding the structure in place.

Two radio frequency transitions are needed to focus one hyperfine state only: one has to be placed between the two magnets and the other downstream the cryostat. The cylinders connecting the two magnets' vessels have to be removable, so that a radio frequency transition, properly insulated by a surface thermally connected with nitrogen shields, can be installed and unistalled.

The proposed cross section is the one sketched in Figure 1.18. The magnet outer

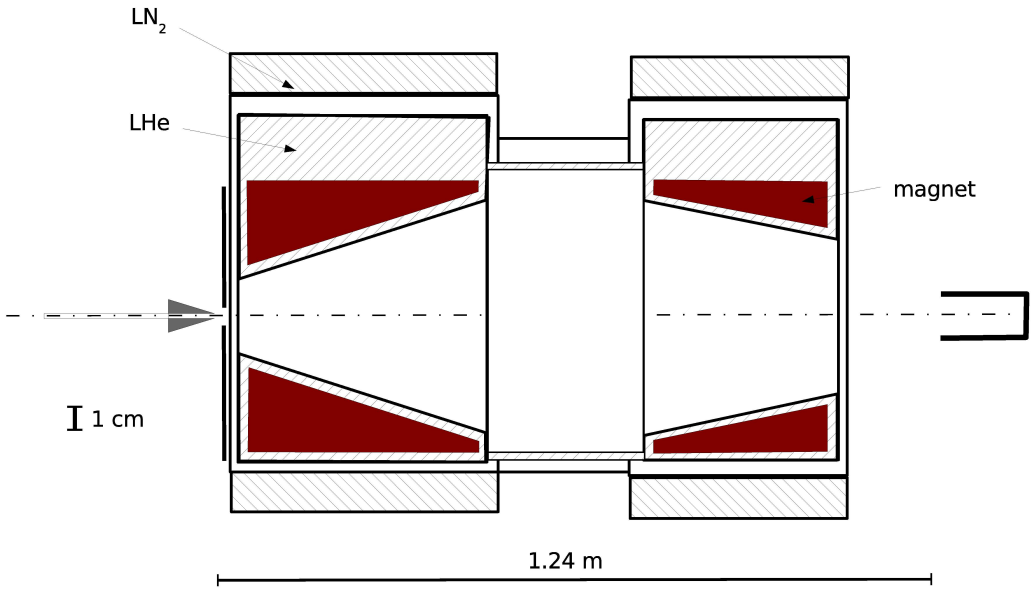

Figure 1.17: Longitudinal section of the cryostat for a superconducting ABS. Two main vessels, one for each magnet, are connected by a cylindrical surface which is cooled by contact with the magnet vessels in order to increase the pumping surface. The vessels and the cold surface are thermally insulated by vacuum and super insulation, and a nitrogen vessel. The helium vessels have a tapered inner surface, as the magnets have. That is the volume available for the beam focussing. The beam enter the system from left and is focussed on the right of the cryostat.

diameter is the lower circle in Figure 1.18, it lays on a Teflon support, conceptually similar to the LHC magnet supports. Series of Teflon supports (one for each vessel) arrive to the bottom of the room temperature outer vessel.

This solution is relatively simple respect to the ones using arms to suspend the cold mass. The thermal load by conduction can be lowered by holes into the Teflon mass to reduce the cross section. The 10 cm left from the bottom of the nitrogen vessel and the helium vessel are useful to increase the thermal conduction length, and again reduce the thermal heat load on the helium vessel. The ABS (and magnets) axis is not aligned with the cryostat's one, so that a sufficient amount of helium is around the magnet and the most is the helium reserve for the running time. This kind of geometry is not much more complicated, and expensive respect to to a coaxial design. The upper part of the volume between the helium and the nitrogen vessels is instead useful to install High Temperature Current Leads (HTCL). These are 30 cm long at least before the thermal contact with the helium vessel, so that the heat load per each current HTCL is 0.2 W on helium.
Important parameter of the design are both the overall dimensions (radial and longitudinal) and the running time. For a superconducting ABS also the regenerating time strongly

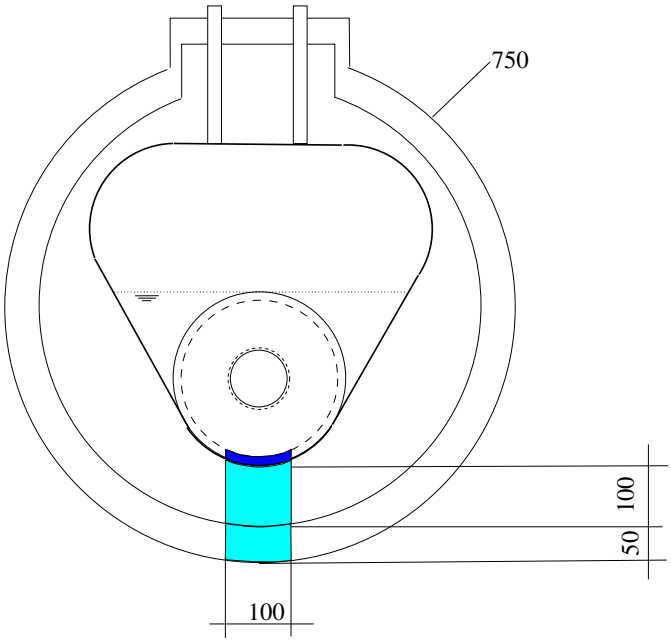

Figure 1.18: Cryostat transverse section. The helium vessel has that non circular shape to optimize the reserve of liquid helium available to run the magnet, the dashes circumferences are the inner and outer diameter of the magnet. In the inner side of the magnet can be noticed how a 4 mm thickness was considered to increase the volume useful for the beam to develop. The dotted line represent the minimum helium level to run the magnet. the G10 support for the magnet is also sketched.

influences the operating time over non operating time ratio.

Pumping

Half the atoms entering the magnet system are defocused due to their spin. These must be pumped out, otherwise the beam attenuation by the background gas (RGA) became fatal for the beam. ABS systems with permanent magnets place annular gaps between the magnets, indicated by arrows in Figure 1.7, in order to pump away the defocused atoms by turbo pumps. The inner bore of the cryostat can also serve as a cryopump, but the saturation of the cryopumping surface can create a too high pressure inside the magnet. Indeed the particles hitting the saturated surface does not stick on the surface and became rest gas, increasing the pressure inside the magnet. The simulations show how the first part of the first magnet experiences the higher flux of not focussed particles. This high flux rapidly saturates the cold surface of the magnet vessel. This increase in pressure have to be pumped and a possible solution is to add a cold surface near the first magnet. An optimal position is the space between the two magnets. Adding a cryogenic surface

in the large gap between the two magnets, the final assembly is a 1 m long cryostat that works also as a cryopump. A scheme of the proposed design is sketched in Figure 1.17.

When atoms collide with the surface, they recombine into molecules and release 7.2×10^{-19} J (4.49 eV) of heat per recombination. With an estimated flux of atoms $\simeq 1\ 10^{19} at/s$, the total heat flux due to recombination is estimated just below 4 W and constitutes an important part of the total heat load on the cryostat.

A further complication exists when hydrogen is used for the atomic beam because the saturation pressure of hydrogen is reasonable ($\leq 10^{-9}$ mbar) only for temperatures below 3 K. The temperature of the liquid helium in the cryostat can be lowered and eventually reach the superfluid helium temperature by lowering its pressure (pumping out the vapor).

1.5.1 The vacuum and the duty time

A layer of solid hydrogen or deuterium grows on the inner bore over time. Assuming that all the atoms stays on the surface when hit it (sticking factor [19] equal to 1), it is possible estimate the buildup rate

$$br\ \left[\frac{mm}{day}\right] = \phi_H\ [at/s] \cdot \frac{8.64\ 10^4\ [s/day]}{\rho_a\ \ [at/m^3]} \tag{1.8}$$

using a solid hydrogen density of $\rho_a = 4\ 10^{28} at/m^3$, see Fig. 1.19.

The continuous running time for the ABS is the time interval between two nozzle regenerations, of the order of 24-48 hours. Although the solid hydrogen layer slightly reduces the acceptance of the magnets, the output intensity is not measurably affected in this short time.

The defocused atoms are concentrated in a small fraction of total cryostat surface area, inside the first magnet. When this spot of surface begins to saturate, the arriving atoms become rest gas. Those atoms are pumped by the not saturated part of the cryostat downstream. The local saturation results in region of high pressure but only minor beam attenuation, as estimated below. The hitting particles are 1.1×10^{19} atoms/s and the throughput is $q_{pv} = \frac{R_0}{N_A} T$ atoms/s $= 1.3 \times 10^{-2}$ mbar·l/s, where R_0 is the universal gas constant, N_A the Avogadro's number and T=90 K the beam equivalent temperature. Considering the cryostat inner bore as a 400 mm long cylinder with 45 mm diameter, the conductance is $C = 12.1 \frac{4.5^3}{40} = 27.6$ l/s. The pressure step through first magnet is then $\Delta p = \frac{q_{pv}}{C} = 3.6 \times 10^{-4}$ mbar, and the beam attenuation is a few percent [16].

The regeneration of the cryopumping surface can be performed warming up few Kelvin the surface and then pumping the evaporated hydrogen. The time to perform this regeneration is compatible with the 3-4 hours needed to remove the ice from the nozzle, so that the duty cycle is almost not affected by the cryostat.

The reliability of a superconducting system is lower than a permanent magnet system because of the cryogenic system, the power supply system and the protection system.

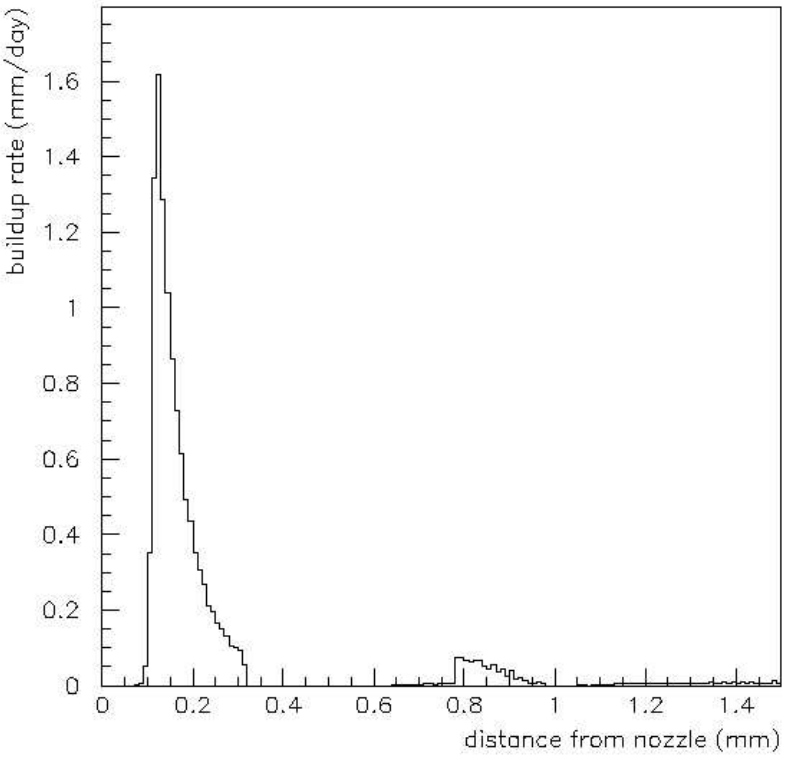

Figure 1.19: The particle deposition rate in mm/day on the cryogenic surface. The maximum layer thickness in a working cycle (24-48 hours) does not strongly affect the beam intensity.

The reduction of reliability correspond in a sizable increase in intensity and a significative increase in flexibility.

Cryostat helium consumption

The heat load on the helium vessel has several components: the radiation between the facing surfaces, the conduction through the inlet and outlet helium pipe, the Teflon magnets' support and the atomic hydrogen recombination when the beam is on.

The external area of the helium vessel is approximatively 1.3 m^2. In order to simplify the heat exchanged between the inner vessel in stainless steel and the nitrogen vessel made up of copper, the surfaces are considered planar and the emissivities are respectively [20]

0.07 and 0.019 (polished Copper). The heat exchanged by radiation can be evaluated by

$$\dot{Q} = \sigma\, A \left(T_2^4 - T_1^4\right) \frac{\epsilon_1\, \epsilon_2}{\epsilon_1 + \epsilon_2 - \epsilon_1\, \epsilon_2} \tag{1.9}$$

where $\sigma = 5.67\,10^{-8} \frac{\mathrm{W}}{\mathrm{m^2\,K^4}}$ is the Stefan's constant, A is the area which are exchanging heat, T_2 and T_4 the temperatures of the surfaces that are 4.2 and 77 K respectively and ϵ_1 and ϵ_2 the emissivity of the materials of the faced surfaces. A multi layer insulation composed by 10 layers of alumined Mylar foils that decrease of a factor 10 the heat exchanged between the faced surfaces has also been considered. A couple of high temperature superconductor current leads have been considered, each current lead 24 cm long connecting the nitrogen vessel and the helium one introduce a maximum heat load in the inner vessel of 0.2 W. The magnet is supported by a G10 structure long as the magnet and having a width of 10 cm (fig. 1.18). The effective area of the support can be reduced to $40\,\mathrm{mm}^2$ to reduce the heat load to 0.10 W in the helium vessel mechanically working the support. The vertical force due to the cryostat weight can be estimated in roughly 600 N considering for safety the stainless steel and copper wall thickness of 1.5 and 3 mm respectively. The vertical force due to the weight of the magnet is $\sim$ 470 N and the G10 stress is then F/A=2.35 Mpa, where F is the force and A the area. Considering that the yield strength of G10 is 10 Mpa, the safety factor is above 4. The heat load in the helium vessel by conduction is $\sim$ 0.1 W, while in the nitrogen vessel is about 1 W. The total heat load heating the inner vessel is estimated in 2.5 W considering the radiation, the conduction of the helium inputs and outputs and the conduction of magnet support.

The circumference inside the liquid helium vessel in Figure 1.18 have a 25 cm diameter: 23 for the magnet diameter (dashed) and 2 cm added for liquid bath.
The minimum liquid needed to keep the magnet inside the bath can be estimated as a first approximation to be 15 l considering the part of the helium vessel containing the magnet as a trapezium 25 cm hight and whose bases of 25 and 50 cm. The maximum liquid helium volume for each magnet is then approximatively $V_{MX} = 2 \cdot \frac{\pi \phi^2\, l}{4} + 15$ l.

Single magnet helium consumption at at 4.2 K

The 23 cm long prototype tested in Ferrara helium consumption per quench is 5.5 liters, for a safe calculation we consider an 8 liters per quench reserve. The useful volume for the ABS operating is then 32 l when the magnet are kept at 1 bar and 4.2 K
The total thermal heat load has been evaluated to be around 5 W for radiation and 4 W for the hydrogen wall recombination contribution. At 4.2 K that 2.5 W heat load takes a 2.5 W $\cdot$ 1.38 l/h/W = 3.43 l/h of liquid helium evaporation. The duty time before an helium refill is then $\Delta t_{4.2\mathrm{K}} = \frac{32\ \mathrm{l}}{3.43\ \mathrm{l/h}} = \mathbf{9.33\ h}$.

Single magnet helium consumption at 2.5 K

In case of a required magnet bath cool-down to temperatures below 4.2 K, the cooling down time and the amount of helium that evaporates must be evaluated. The liquid lost during the liquid bath under cooling from 4.2 K to 2.5 K is roughly the 30%, so that the residual liquid is $43.4 \cdot 0.7 = 30.4$. 11.4 liters are fixed for the magnet safety (minimum bath and quench protection), so that 19 l are available for the duty time, corresponding to **7 h**. With a 250 m^3/h effective pumping speed pump, the time required for the 43.4 l bath cool-down to 2.5 K is roughly 20 min (considering for example a 50 cm long pipe with a 5 cm diameter). The duty cycle is influenced by the cool-down operation.
The heat load is constant (5.0 W). The helium latent heat is $\frac{h_{2.5}^{vap}\,\mathrm{J/mol}}{M\ \mathrm{g/mol}}\rho_{2.5\mathrm{K}}\frac{\mathrm{g}}{\mathrm{l}} = \frac{92.5}{4}144.8 =$ 3348.5 J/l and the helium consumption is then 298.6 10^{-6} l/s=**2.7 l/h**.

1.6 Conclusion

A high intensity atomic beam source design based on cryogenics and low temperature superconductor technology has been presented. With such a novel device, a sizable increase in the source intensity is envisaged, up to an order of magnitude. This new application of superconducting sextupoles requires small magnets with high pole-tip fields. The prototype manufactured in the Ferrara laboratory demonstrates the feasibility of such kind of magnets and, at the same time, tests a new concept design based on superconducting coils strengthened by an iron magnetized core. The design of a cryostat suitable for a superconducting ABS has been presented: it does not to restrict the beam aperture more than necessary, it is designed to efficiently pump the defocused hydrogen atoms and to match the running time of a typical ABS system.

Chapter 2

A test bench for low temperature small superconducting multipole magnets pole field mapping

As part of the thesis work, a low temperature test bench has been developed in Ferrara modifying an existing cryostat to map the field of small superconducting magnets, up to 40 cm long and up to a 34 cm of outer diameter, at their working conditions, i.e. at 4.2 K and full current. The test bench has been presented at 19^{th} Magnet Technology conference [21]. To measure the field at nominal current is important especially in case of not-conventional magnets. When the inner pole is built by iron, as in the case of a small sextupole manufactured in Ferrara, the saturation effects are important. The field can only be measured in working conditions since at low temperature and with the magnet fully powered, all the saturation effects which are source of uncertainty in TOSCA simulations, are directly measured.

2.1 Introduction

Superconducting sextupole magnets with small tapered inner bore ($5 - 10$ 'cm of radius) and high pole tip field (6-9 T) are an important part of the design of a high intensity atomic beam source (ABS) characterized by the use of superconducting magnets [10].

Inside the magnet bore of a multipole magnet the field can be expressed as Fourier expansion both for radial and tangential components:

$$B_r = \sum_{n=1}^{\infty} \left(\frac{r}{R_{pt}} \right)^{(n-1)} \left[A_n sin(n\theta) + B_n cos(n\theta) \right] \tag{2.1}$$

$$B_\theta = \sum_{n=1}^{\infty} \left(\frac{r}{R_{pt}} \right)^{(n-1)} \left[A_n cos(n\theta) - B_n sin(n\theta) \right] \tag{2.2}$$

where A_n and B_n are respectively normal and skew $2n$-pole components, while R_{pt} is the pole tip radius. Sextupoles are used for the focalization of electrically neutral particles because of their particular beam spot geometry reproduction, therefore any other field component is unwelcome. In real magnets non ideal fields harmonics are introduced by the non zero assembly tolerances, just like a possible misalignment between the geometrical and magnetic axis. These imperfections have to be mapped and properly accounted for in the application the magnet was designed for.

The optimization of a high intensity superconducting ABS requires a high precision sextupoles magnetic field map in order to measure the position of the magnetic focalizing axis and the field distribution in the focalizing volume. There are three typical field measurements of the multipole fields: pole tip field measurement and harmonics measurement by rotating coil or moving Hall probes.

- The pole tip field measurement can be easily performed during a normal cool-down. For example in the sextupole manufactured in Ferrara, the pole tip field was measured during the training [22]. The pole tip field is the most characterizing single parameter, but has no information about the quality of the focalizing field, such as the focalizing axis respect to the geometrical axis, or the real radial gradient and the different field harmonics.

- The rotating coil measurement, consisting in the output reading of the voltage across a coil that rotates inside the magnet bore, measures the field harmonics but not the field value.

- The moving probe measurement measures the field in a finite number of points inside the magnet bore in a defined direction. Choosing an adequate number of positions and orientations of the probe it is possible to attain a good measurement of absolute value of the field in a (selected) finite number of points, of its harmonics, its gradient, and the exact position of the zero field (focalizing) axis. The latter method requires a bigger effort in terms of costs and manpower, but the resulting measurement is much more complete to characterize the multipoles used for the design of a high performance superconducting ABS.

A magnetic field map is a direct measurement of the magnet performances and of the magnet manufacture quality. It allows to calculate the maximum pole tip field (extrapolating), to measure the radial field gradient, which is directly proportional to the focalizing force in an ABS, the magnetic axis and finally the field harmonics. If test bench designed

to work at low temperature are not available, the map characterizing the field has to be measured at room temperature and low currents. In this case the working conditions have to be extrapolated by simulations performed with specific codes like TOSCA [23].

Both a room temperature measurement and a low temperature measurement of the prototype sextupole manufactured in Ferrara [22] are presented in this section. The room temperature field map has been performed at CERN using an existing measuring device. A dedicated test bench, whose design and construction was part of the thesis work, was employed for the low temperature field map in the Ferrara laboratory.

2.2 High temperature measurement

The field mapping of the sextupolar prototype (see Sec. 1.4) at room temperature is a first test of the construction quality of the magnet. Moreover the data taken can be used to refine the TOSCA simulation including saturation effects of the iron placed inside the magnet pole supports and to develop a fit program to calculate the measured field harmonics of a multipole.

The magnetic field of the sextupolar prototype has been measured at room temperature and low current as a preliminary field measurement at CERN in 2003. The magnetic field has been measured by a single Hall probe moved by numeric control motors along the 3 axes while the magnet was supplied by 1 A. The magnet was fixed to a bench coupled to the movement system of the Hall probe (see fig 2.1). The probe is positioned at the end of a 0.5 m long Aluminum bar, its measuring direction being orthogonal to the bar. The probe is in a resin shell so that error in the position of active area of the probe in y direction is 0.5 mm. The bar is connected to the moving system by screws (see fig. 2.2). The orientation of the probe has been set for measuring magnetic fields with vertical orientation. The magnet can be rotated in six different positions thanks to the rotation support machined in the Ferrara workshop. Since the angular precision of each rotation is fundamental for the measurement, the holding support of the magnet have to provide a precise positioning of the magnet with respect to the system bench. The support is screwed on the systems bench and when the magnet is in position its axis is parallel to the bench surface with a 0.1° error. The magnet position with respect to the support is fixed by three screwed holder and one positioning pin (Figure 2.2) and can be rotated by 60 ± 0.1 degrees. The angular precision of each rotation was attained by a precise numerical control machinery in Ferrara workshop.

For each 60° rotation of the magnet, the field along x (horizontal) and y (vertical) axes is measured with a 1 cm step from the center (r=0) up to four centimeters of radius (r=4), (see Fig. 2.3). Whenever possible depending on the tapering of the inner bore, the measurement was extended up to 4.5 cm. As a result the measured points for each traversal plane are 108 or 132. The transverse planes are measured with 1 cm step along the z axis (corresponding to the geometrical axis). The measurement has been extended

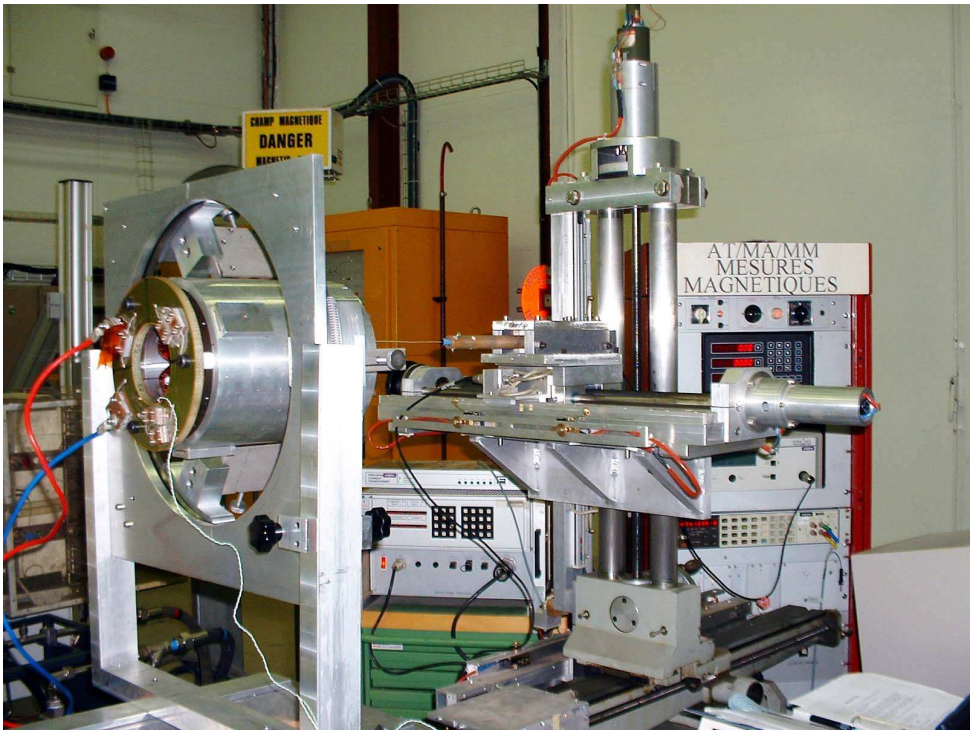

Figure 2.1: Overview of the numerical control apparatus during the high temperature field mapping performed at CERN

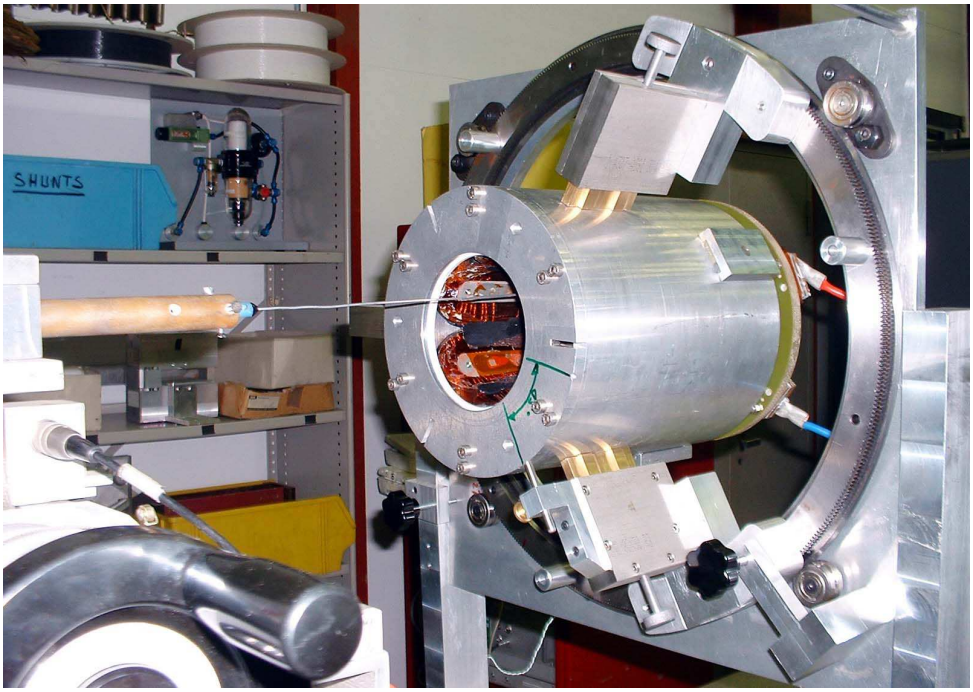

Figure 2.2: Ferrara prototype sextupole during high temperature field measurement, the magnet is hold by a high precision custom tool machined in Ferrara workshop, the bar on which is fixed the Hall probe used for the measurement is entering the magnet.

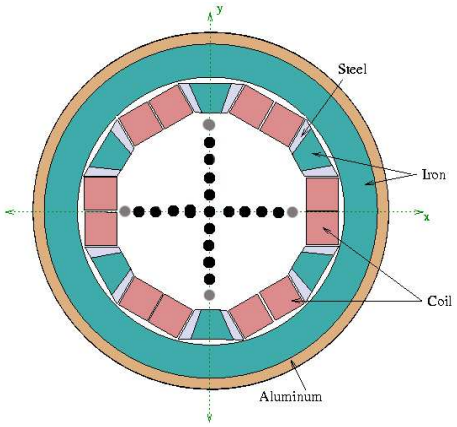

Figure 2.3: Points where the magnetic field is measured; the extreme points (in grey) are taken whenever possible depending on the tapering of the inner bore. Note that in the measured points the field orientation is vertical.

7 cm outside the magnet bore on both sides, so that the fringing field can be estimated.

2.2.1 Data analysis

The data have been analyzed to find the field harmonics expressed in equations 2.1 and 2.2 by a Fortran program using MINUIT.

The field harmonics measured at maximum current are reported in Figure 2.4, where the vertical dashed lines represent the geometrical limits of the magnet. The normal field harmonic A_i, the ratios of the component respect to the sextupolar component A_i/A_3, the skew components B_i and the ratios of the skew components respect to sextupolar component B_i/A_3 are plotted. The results are reported for each measured transversal plane. The sextupolar skew component is not evaluated because the field is measured where the sextupolar field A_3 component is maximum, while by definition the skew sextupolar one B_3 vanishes, so the fit is not sensitive to the latter component.

The field outside the magnet approaches zero in few centimeters. The quadrupolar component A_2 is lower than 10^{-2} and the 8-polar one is almost constant and around 10^{-2} of the sextupolar one A_3. Such a quadrupole contribution is acceptable for an ABS magnet. The skew quadrupolar and 8-polar components A_2 and A_4 have an almost constant ratio with respect to the sextupolar component.

The almost constant A_2/A_3 value for all transversal planes inside the magnet confirms the mechanical measurement about the mechanical precision of the sextupole. The mechanical precision have to tested also at low temperature. The low current and thus low field involved in the high temperature field map implies that the iron works in the linear part of the saturation curve.

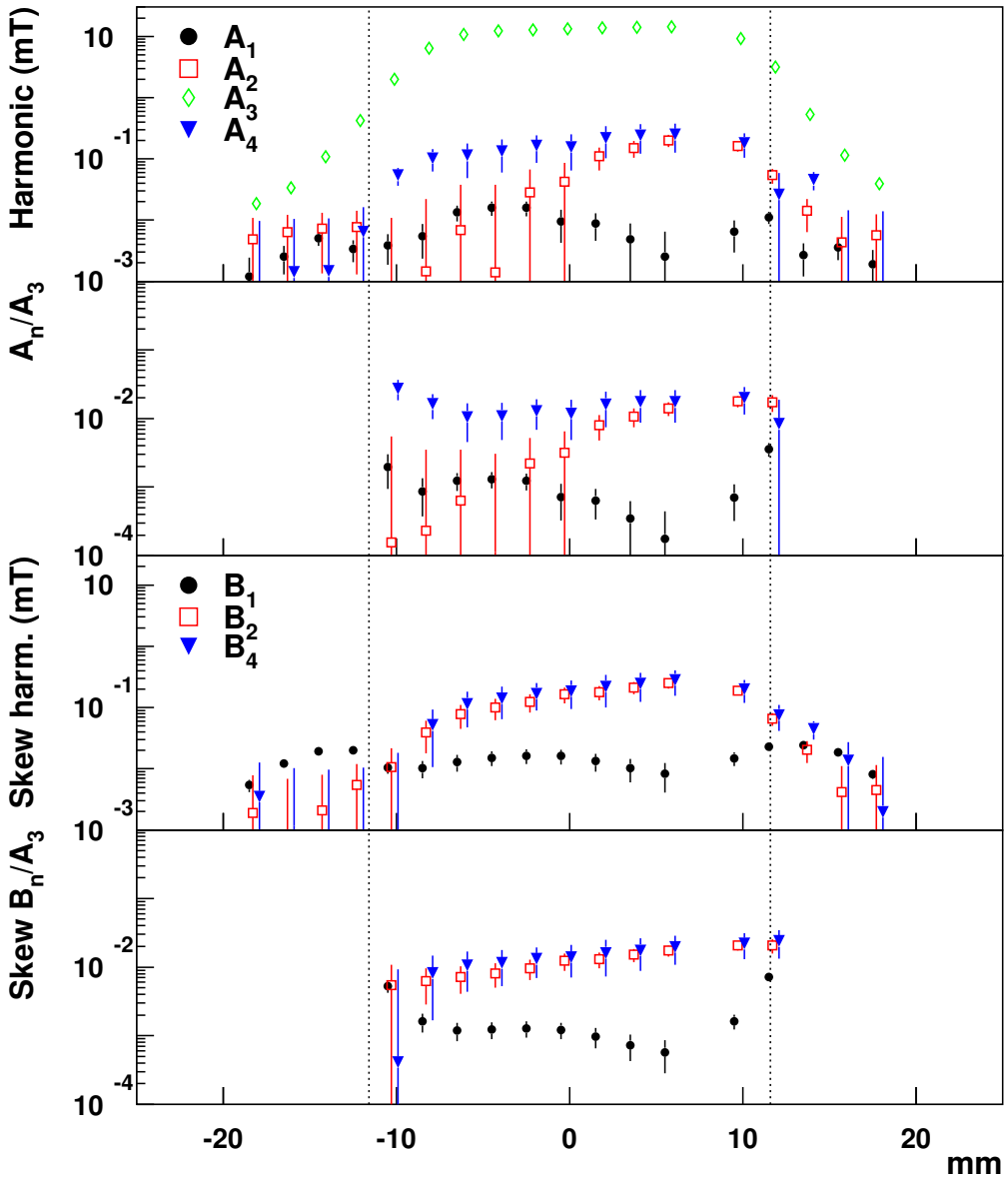

Figure 2.4: Measured harmonics at room temperature and 1 A.

2.3 The test bench for low temperature magnetic measurements

The field mapping test bench for low temperature field mapping is realized modifying a top access cryostat (Fig. 2.5): a measuring chamber kept in vacuum is inserted in the cryostat to access the magnet inner bore. Ten Hall probes are fixed to a plate moved by a 1.8 m shaft connected to the movement system. The movement system is in placed on top of the cryostat in air at room temperature.

2.3.1 The field measurement

The field mapping is performed by ten CMI Hall probes whose position is set with a maximum error of 0.5 mm during the measurement. Their active area is a surface of 1.0 mm^2 and the magnetic field measurement error is below 3% for a magnetic field flux between -15 and 15 T. The range of field to be measured in our case is ± 3.5 T. The signal read from the probes is a voltage, each probe has it own sensitivity varying from 16 to 114 mV/T and the ones characterized with higher sensitivity are placed at lower radius since the measured field is lower. Every probe is calibrated by the manufacturer at 9,000 T and the voltage output error is 5 10^{-7} V so that the expected error of the probe in the 3.5 T range is less or equal to 0.1 mT (1 Gauss).

The probes are mounted on the probe holder shown in Figures 2.6 and 2.7; the ones measuring radial field are placed at ± 30, ± 35 and ± 40 mm from the axis, while the probes measuring the tangential field are placed on only one side at +15, +26 and +37 mm. The probes are fixed to the holder by screwed wedges to reduce probe misalignments and movements during assembling and measuring. The field is measured on planes orthogonal to the magnet's geometrical axis with a vertical 1 *cm* step. On this plane, at each 60° step rotation of the probe holder, the Hall probes have the optimal orientation to measured the maximum radial and tangential component of the sextupolar field. Using the data from all the six 60° rotations, which corresponds to 60 measured points, the Fourier fields components [24] up to 12-pole component can be measured. The ratio $\frac{A_3}{A_n}$ is measured with an error less then 10^{-2} for each plane.

The whole measurement is driven by a Visual C++ program, which controls two motors to move the probe holder and acquires the signal from the Hall probes. The data are written on a file, which is analyzed offline. Each reading of a probe has two steps: first positioning ($\sim$ 15 seconds) and then measuring. The measurement is not performed during a continuous movement in order to reduce the problems in synchronization between motors and data acquisition and take rid of mechanical oscillations during the positioning. The measurement lasts one hour thanks to the fully automated movement (details in Sec. 2.3.4).

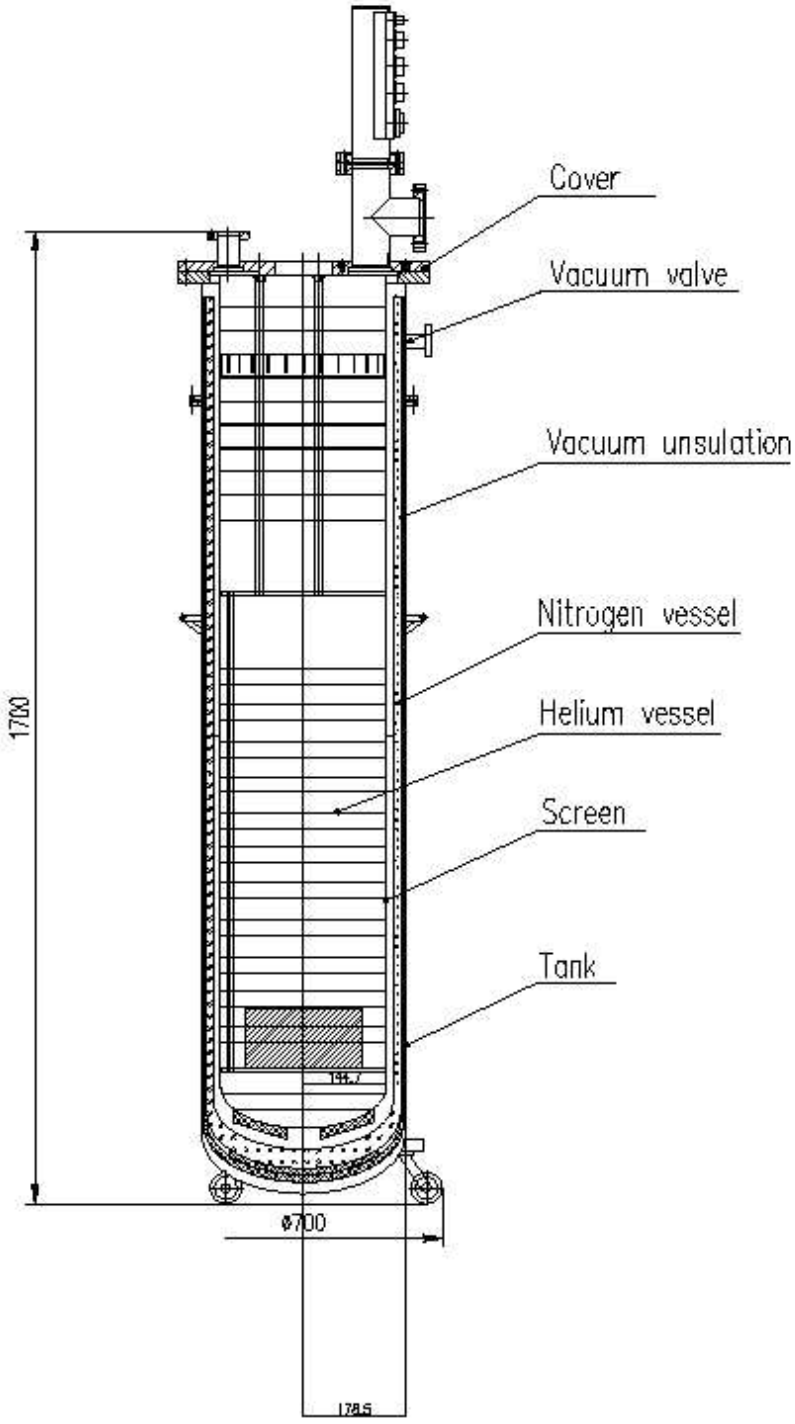

Figure 2.5: Cryostat layout before the modification. The helium is kept at 4.2 K (1 atm). The top flange is thermally insulated by mylar aluminum plates. On the top flange is visible the CF100 flange where the measuring chamber is connected. The magnet is connected to the an intermediate plate by 3 bars (one is shown).

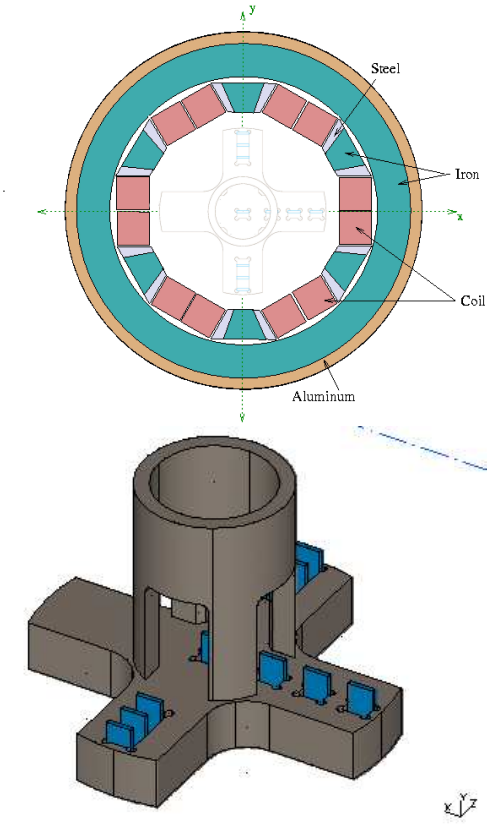

Figure 2.6: The probe holder (cross shaped) and the connection to the shaft. The Hall probes are fixed to the holder by screwed wedges (not shown).

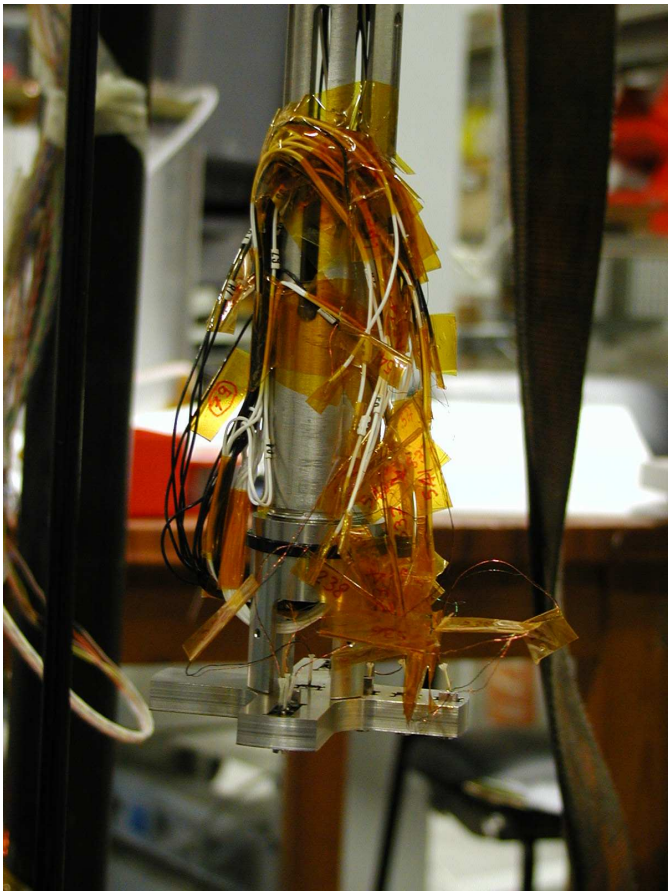

Figure 2.7: Probe holder during assembly. The holder is fixed to the hollow shaft and all the Hall probes are cabled and fixed by wedges.

2.3.2 The cryostat

The cryostat used for the test (Fig. 2.5) has a helium 60 l bath kept at ambient atmosphere and is designed to test small multipoles magnets.

Three stainless steel bars fixed to the top flange hold the magnet to be tested inside the cryostat. The lateral and bottom thermal insulation comprises a standard double vacuum layer separating the inner helium vessel at 4.2 K, the intermediate nitrogen vessel at 77 K, and the external vacuum vessel at room temperature. The top thermal insulation is fixed to the top flange and composed by seven mylar alumined plates plus an intermediate copper plate in good thermal contact with the 77 K nitrogen vessel. The 25 liters of liquid nitrogen is poured inside the vessel by an inlet on the top of the cryostat.

The cryostat performances where tested in Ferrara [22], the static helium consumption is 0.4 l/h with no cold mass and 2.7 l/h with a magnet inside.

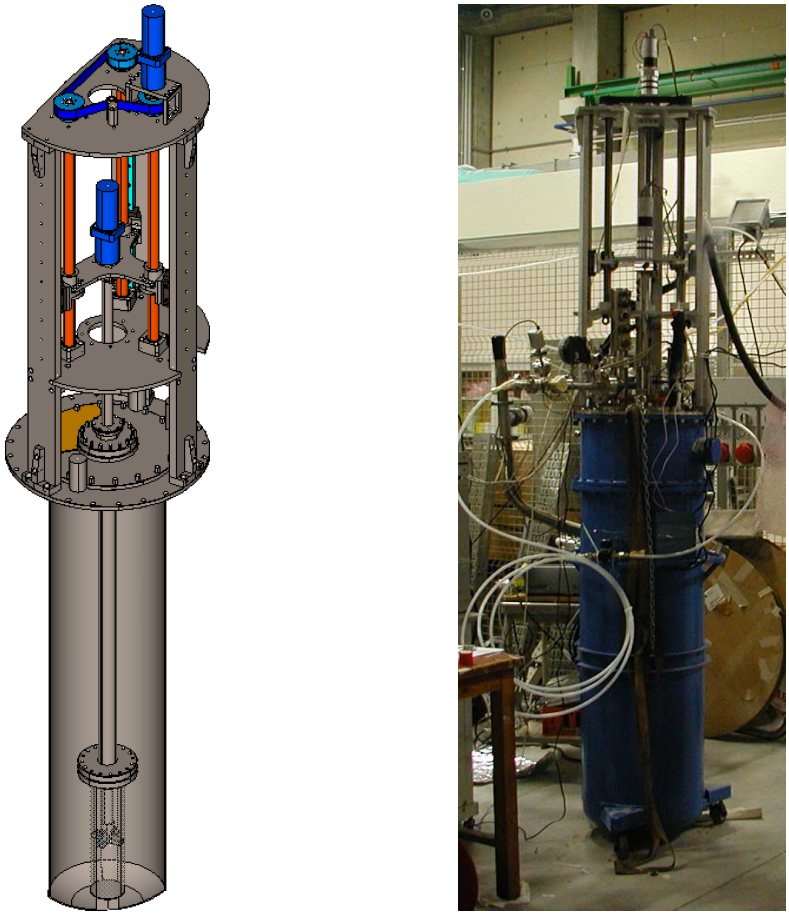

Figure 2.8: Overview of the liquid helium vessel, cryostat's top flange and movement system CAD model (left) and of the apparatus after the assembly. The shaft entering the measuring chamber and the Hall probes holder are visible.

2.3.3 Cryostat modification

The movement for the probes holder must be at room temperature, so a rigid structure is fixed on the top of the cryostat (see Fig. 2.8). A plate is moved vertically by one of the two motors. On the movable plate is fixed a second motor with rotates a 2 m stainless steel hollow shaft holding the probe holder. The magnet inner bore is accessed by a 45 mm diameter stainless steel pipe fixed on a CF100 flange on the cryostat top flange and ending in a stainless steel small chamber. The probe holder is inside the bottom small chamber and connected to the upstream motor by the shaft. A scheme of the measurement apparatus is sketched in Fig. 2.8.

The materials entering the magnetic field must have negligible magnetic behavior, in order to avoid any magnetic force on parts nor any magnetic field shielding that could

decrease the measurement precision. The allowed materials have magnetic permeability μ below 1.005 like stainless steel AISI 316LN, Aluminum ($1 - \mu = 3.5\ 10^{-4}$) or copper ($1 - \mu = 4.5\ 10^{-4}$). For safety, all the parts to be inserted inside the magnetic field have been heat treated in nitrogen atmosphere to reduce any possible magnetic behavior due to the severe machining (all of them are machined from bulk material). The nitrogen atmosphere prevents the oxidation of the surfaces of the parts. The heat treatment begins with a 1.5 h warming up to 850° and then the components stay half an hour at that temperature. Then the temperature is increased in 40 minutes to the maximum temperature of 1050°, the parts stay 3 hours at that temperature and are quenched as fast as possible by nitrogen gas at room temperature.

The introduction of the measuring pipe reduces both the liquid helium reserve and the operating time. The time required for a measurement is an important parameter since the inner vessel decrease the total amount of liquid helium inside the cryostat, reducing the time available for the measurement. The helium capacity of the unmodified cryostat is 60 l. The magnet, to be kept at 4.2 K, must be completely inside the bath and an amount of helium is required to avoid that in case of a quench, the helium bath does not cover the magnet. The helium vessel inner diameter is 34.0 cm. The sextupole height is 23.0 cm, considering an overall 30 cm occupied, there are 34 l of helium available for the measurement. After the modification the amount of helium available for the measurement are 33 l. The average helium consumption for the tested sextupole magnet is 5.5 l.

A small pipe diameter compared to the cryostat inner diameter was chosen to reduce heat flux into the helium bath and decrease as much as possible the reduction of liquid helium available for running the magnet. The vessel containing the shaft is under low vacuum. Main reason is to avoid ice formation on the inner walls which reduces the available space for the measurement and the movement of the shaft. The vessel is in contact with liquid helium, so that the wall temperature is 4.2 K at the bottom and room temperature at the upper flange. The small amount of space available, especially inside the magnet's inner bore forced to use a thin stainless steel wall vessel instead of any other insulation. The small diameter reduces the pumping down conductance. The measuring chamber is kept at low pressure ($p \sim 1.0\ 10^{-2}$ mbar) at room temperature by a small turbo pump to avoid the risk of ice formation on the walls of the measuring chamber. The low pressure is reduced to 10^{-6} mbar when the inner cryostat vessel is at 4.2 K strongly reducing the heat flux due to conduction through gas. The pressure inside the measuring chamber is strongly reduced by cryopumping when the cryostat is cold, the lower part is in fact at direct contact with liquid helium. The shaft is moved vertically and rotated during the measurement. The vacuum tightness at the shaft entrance in the measuring chamber is an important issue: a double o-ring system has been used. Turbo pump oil has been used to improve the vacuum tightness instead of standard vacuum grease it did not stick to the shaft, the pressure has been constantly below 10^{-3} mbar. An example of the vacuum quality during measurement is shown in Figure 2.9.

The measuring chamber introduce a heat flux due to conduction through the pipe

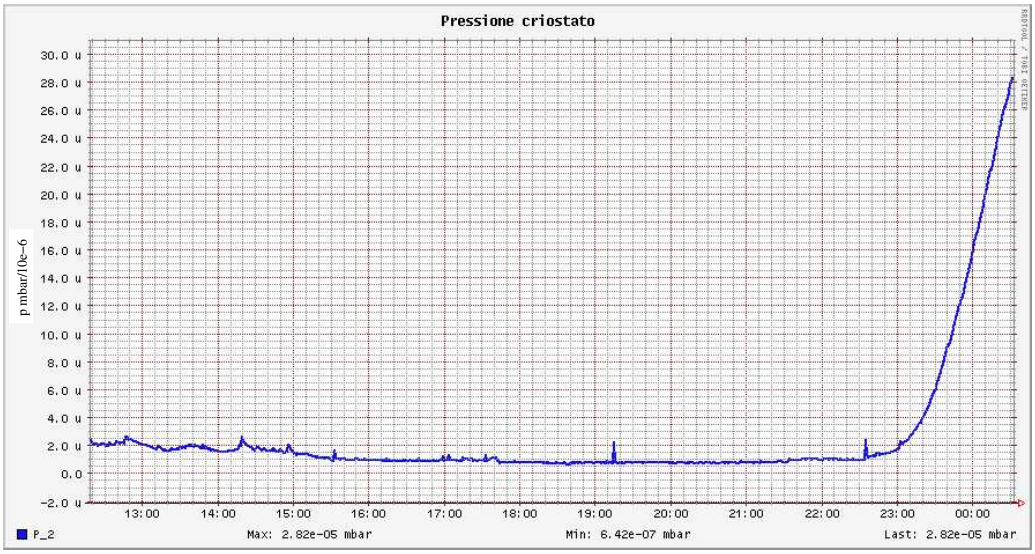

Figure 2.9: Pressure inside the measuring chamber during measurement.

stainless steel, the residual gas and the probe wires. The heat conduction through metals is easily estimated by the Fourier law, $\dot{Q}_{CSS}= -\lambda_1^2 A\frac{\Delta T}{l}$, where A is the conducting cross section, $\Delta T = T_2 - T_1$ is the difference between the temperatures at the extremes of the conductor, λ_1^2 the thermal conductivity averaged between the T_1 and T_2 temperatures, and l the length of conduction. The stainless steel thermal conductivity averaged from $T_1 = 4.2$ K and $T_2 = 300$ K is 10.3 $\frac{\mathrm{W}}{\mathrm{mK}}$. The worst condition for the outer pipe connecting room temperature with liquid helium is with the bath at maximum level, in that case the conducting length is 1 m, giving a heat flux of $\dot{Q}_{CSS}= 0.94$ W.

The heat conducted by the helium gas can be estimated [20] as

$$\dot{Q}_{CHe}= A_0 a_0 P_{torr}(T_2 - T_1)A_{cm^2} \tag{2.3}$$

where A_0 is a constant (0.0028 for helium), $a_0 = \frac{a}{2-a}$ is the effective accommodation coefficient for the case of faced surfaces with equal area and same accommodation coefficient. A conservative value $a = 0.5$ was taken for helium. The pressure in torrs P_{torr} has been set to 10^{-2} torrs for safe calculations, $T_2 - T_1$ is the temperature difference between the two surfaces ($\sim 300\ K$) and A_{cm^2} the area in squared centimeters. The total heat flux due to conduction is then

$$\dot{Q}=\dot{Q}_{CSS} + \dot{Q}_{CHe}= 0.94 + 0.69 = 1.63\ W, \tag{2.4}$$

corresponding to 2.3 l/h of liquid helium. The system can state more than 6 hours at low temperature without helium refilling, which is three times the time required for a complete field mapping.

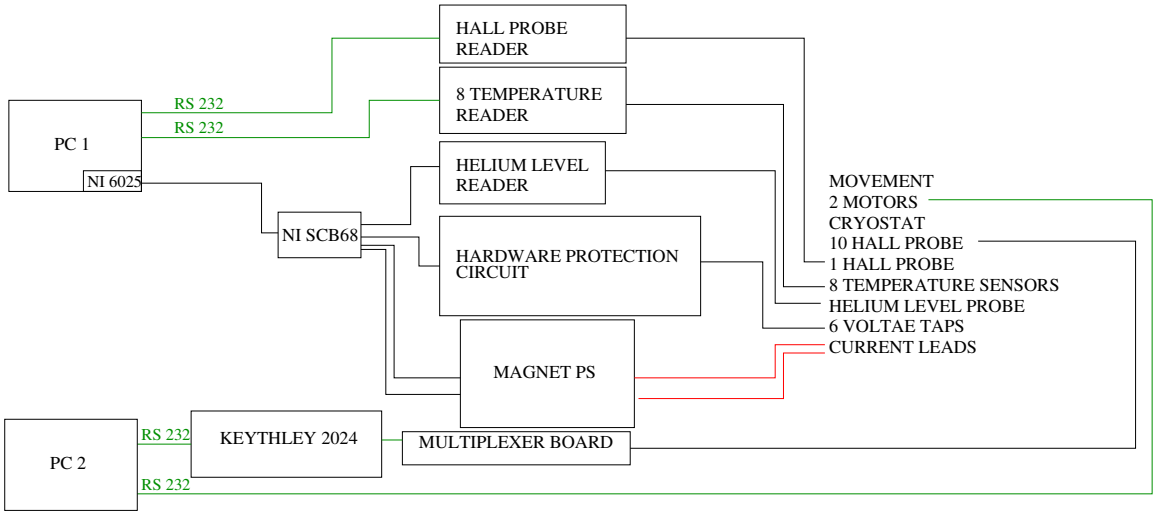

Figure 2.10: Data acquisition scheme. PC1 provide a fast software quench protection and monitors the cryogenics. Its acquisition is based on National Instruments hardware and LabView. PC2 controls the movement system and reads the probes used for the field mapping by a high precision Keithley multimeter. The multiplexer board is custom made in Ferrara. Its acquisition program is based on Visual C++ and the communication is by RS232.

2.3.4 Quench protection and DAQ

The quench protection system and the DAQ are partially connected. Figure 2.10 is a simplified scheme for the DAQ and quench protection system.

Quench protection

There are two quench detection systems: a hardware system, which provides the main control, and a software system. Both protections read the voltage across each single magnet coil. The voltage taps are connected to the slabs connecting the coils (Fig. 1.14) and are opto-insulated in the hardware protection board. The opto-insulation electrically splits the protection circuit (and the monitoring PC) from the magnet coils. The signal height is reduced by a factor 2.5 by the opto insulation.

When the hardware protection system detects a quench simultaneously turns off the power supply and dumps the magnet on a protection resistance. The power supply can provide 600 A at a maximum voltage of 12 V and has its own dump circuit. A 19 kJ stainless steel resistance was installed inside the power supply cabinet for magnet protection only. When the power supply is turned off the magnet current is directly dumped on the protection resistance. The protection dump is activated by a normally closed relay whose reaction time is 100 ms, this is then roughly the activation time for the protection.

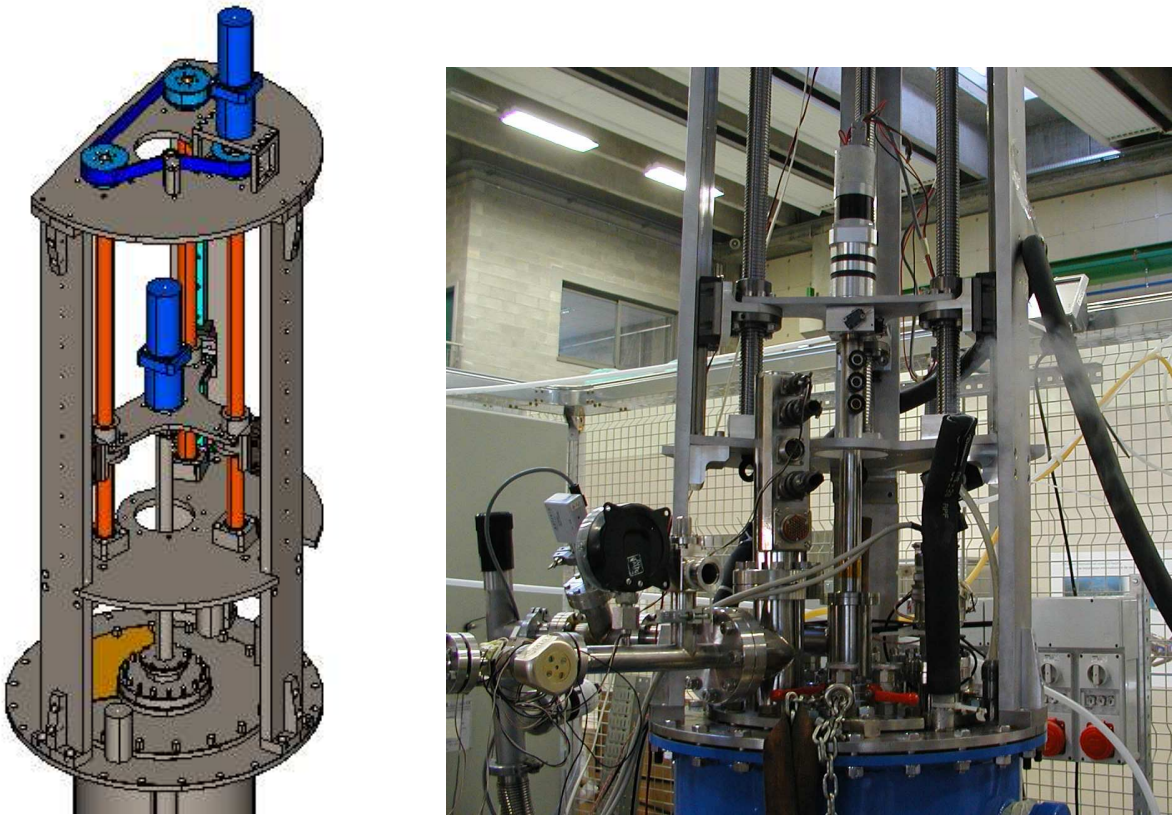

Figure 2.11: Top cryostat's flange and precision movement system CAD model (left) and final assembly (right). The vertical movement of the t-shaped plate is driven by the motor on the top of the structure that rotates the three recirculating spheres screws. All the drawn parts outside the cryostat are in aluminum. The shaft entering the vacuum is rotated by the central motor fixed on the t-shaped plate.

In case of failure the protection circuit is activated automatically (Figure 2.12).

DAQ

The DAQ system is based on two PCs. The first runs a LabView program monitoring the magnet status and providing software quench protection. The second controls the two motors of the probe movement and the acquisition of the ten Hall probes for the field mapping (see Fig. 2.10).

The LabView program controls the magnet temperature, the helium level inside the cryostat, the supplied current to the magnet, the fast software quench detection reading the voltage across each coil through the hardware quench protection circuit, and one Hall probe placed on a magnet pole at half of the magnet height. The magnet's current is controlled by a feedback loop (of 0-10 V) with the current supplier.

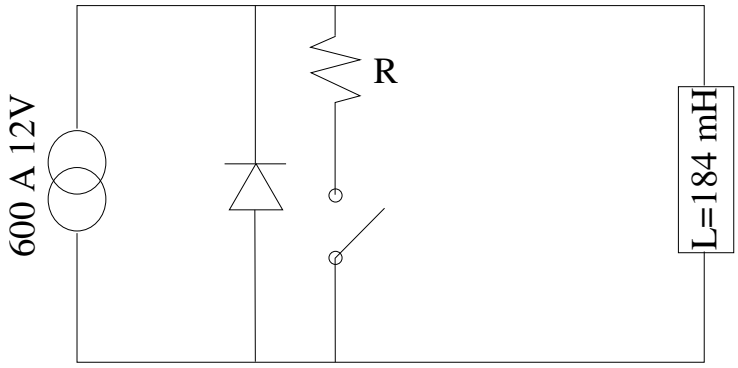

Figure 2.12: The protection circuit for the magnet power supply. The power supply can supply 600 v ±12 V. The power supply has its protection diodes (not shown). The magnet (the inductance in the scheme) is protected by the resistance R. The protection is activated by the relay that closes the current loop over the magnet, the relay is normally closed.

The movement of the Hall probes holder and the Hall probes reading is driven by a Visual C++ program on a PC.
One of the two motors (master) is directly connected by RS232 to the PC, the other one is connected to the master motor by CAM bus. The 'intelligent' motors have an internal program communicating with the PC.

Both motors have a resolution of 2000 steps for each turn and a 1/50 gear ratio reduction. The master one drives the vertical movement by its connection to one of the endless recirculating spheres screws that move the tee shaped plate (see fig 2.11). The motion is transferred to the others screws by a belt. The slave motor gear reductor is directly connected to the probes movement shaft.

The 10 Hall probes reading is a four wires measurement with differential reading by a Keithley multimeter. The Keithley supply 100,000 mA to all Hall probes, connected in series, and reads the output voltage by a multiplexer board which relays set the read probe. The current stability is one important part for the measurement, since the probe output is proportional to the current supplied. The multiplexer board can also short circuit the 100 mA on a resistance to perform calibrations on the probes (see section 2.4.1). The ten Hall probes have the 100 mA supply circuit connected in series: the main power supply loop connects all the probes, two others power supply couple of wires split the power supply in series of 3, 4 and 3 probes. All the power supply lines are connected to the multimeter power supply by relays on the multiplexer board so that which lines are activated is remote controlled by PC. The spare power supply lines have to be used in case that a probe fails and has not any more electrical continuity so that the probes in the small 3 (or 4) series containing the failed probe are not read, but the others can be read. The multimeter and the multiplexer board are on the same serial line, a microchip on the board decide who is the destination of the command sent on that line and let the

command arrive to that instrument only.

All the signals and power wires of the Hall probes pass inside the hollow shaft. They enter the vacuum by 3 feedthroughs that are visible in Figure 2.11. The probe holder is shaped to provide space for the wires connecting the probes, if Figure 2.7 is reported the final cabling.

The system is able to read the Hall probes in a range $\pm 200\ mV$ with a μV resolution. The measurement is completely automatized by the DAQ program, and driven by the starting parameters given to the fully programmable motors for the movement, to the probes reading and data logging. This provides a fast, safe, reliable measurement.

The C++ program is able to control several operations:

- to move the Hall probe holder in vertical direction or rotate it;
- to open o close the current loop on the probes;
- to select the probe to be read by Keithley multimeter;
- to read the Hall probe output by the multimeter.

All these single operations can be activated by screen selection, or the program can interpret a list of commands.

The user is able to short circuit the 100 mA supplied letting the multimeter to read by four wire measurement the probes (as if in normal measurement) while they are not powered. This is important to measure the pedestal (see sec. 2.4). The operating mode driven by a list of commands supplied by the user guarantees an important flexibility in the measurement, i.e. the choice about the number of measured position, ranges and steps in movement is completely free and can be easily modify. If needed, the user can decide which probes are read, as an example this can be used to increase the measuring speed. The program basic control loop is: first move the two motors in the nominal position, then measure each single Hall probe. The first movement is in the vertical direction, and after the motor responded that the positioning is finished, the angle is set by the second motor. The internal parameters of the motors i.e. maximum speed, positive and negative accelerations and maximum current absorbed are set by a specific program supplied by manufacturer. The relays used for the multiplexer board are specific for very low voltage signals and they have to be turned on for short periods in order not to vary the temperature of the relay itself which can modify the contact resistance and thus the measured value. The relays connected to the probes signals are turned on only for the time needed for the measurement and then turned off; multimeter has been set to average 50 measures to achieve the required resolution, so each probe requires few seconds to be measured. The multimeter is triggered by the PC program to start measuring and sends back the measurement which is saved on disk. The program is able to force the motors to take the actual position to be the absolute zero position. This is used for the zeroing procedures. At the system startup, in case of power failure or in case of motors failure,

the absolute referring system have to be set. It has to be noticed that the motors have been programmed so that in each of the listed cases they stop and keep the position: that means that if they are powered on, the system does not move. Moreover in case of power failure or motors not powered, the 1/50 gear ratio epicycloidal reductor makes any movement very difficult. These specifications where chosen to guarantee safe operation for the system.
The rotation positioning error of the shaft is $\sim 0.1°$, the motor can read its rotational position with a precision of 4 10^{-3} degrees (corresponding to 10000 steps/round), the precision of the rotation has been set to 0.005° to increase the positioning speed and because the error in angle is affected by the zeroing procedure. The motor moving the shaft in vertical direction in principle resolve the vertical screw step of 5 mm in 100000 parts, but the error in the positioning in zed direction is limited by the screw mechanical clearance and is equal tp 0.1 mm.

The zeroing procedure for the vertical direction is manual: the vertical axis is moved until a visual positioning is reached. This procedure has a precision of around 0.1 mm. The angular zeroing is more delicate and is automated: the 'slave' motor is forced to rotate in a fixed direction until the end of run switch is pressed, then the motor stops and move in the opposite direction by 60°. The reached position is the zero of the motor. This procedure reproduce the positioning with an error below 0.01°. The program synchronizes the movement and the data acquisition reducing dead times.

2.4 The low temperature test

The cool-down from room temperature to 100 K lasted around 70 hours (Fig 2.13) because the cooling speed have to be lower than 10 Kelvin per hour (Fig. 2.14). The magnet is composed by different materials having different thermal expansion coefficients so that a too fast cooling speed can generate stresses that permanently damage the coils. The behavior during the cool-down of temperatures taken at six positions in the inner part of the magnet, one below the magnet and one connected to the vetronite plate placed on top of the helium vessel are shown in Figure 2.13. The cool-down has been very homogeneous and the probe showing faster temperature rates is the one placed on the vetronite plate and measuring the gas temperature. The difference between the magnet temperature and the gas temperature is the parameter used to tune the cooling rate of the magnet. The magnet cool-down has been performed in two steps: the first step ranges from room temperature to $\approx 90 - 100$ K and the second step ranges from the latter temperature down to 4.2 K. During the first part of the cool-down the helium vessel has been filled by gaseous helium at one atmosphere and was cooled by radiation. The nitrogen vessel (see Fig. 2.5) was cooled first by gas nitrogen and then by liquid. The liquid nitrogen level was monitored by two temperature sensors connected to a liquid level controller. The controller opens and closes the nitrogen input valve (by a 220 V normally open relay) to

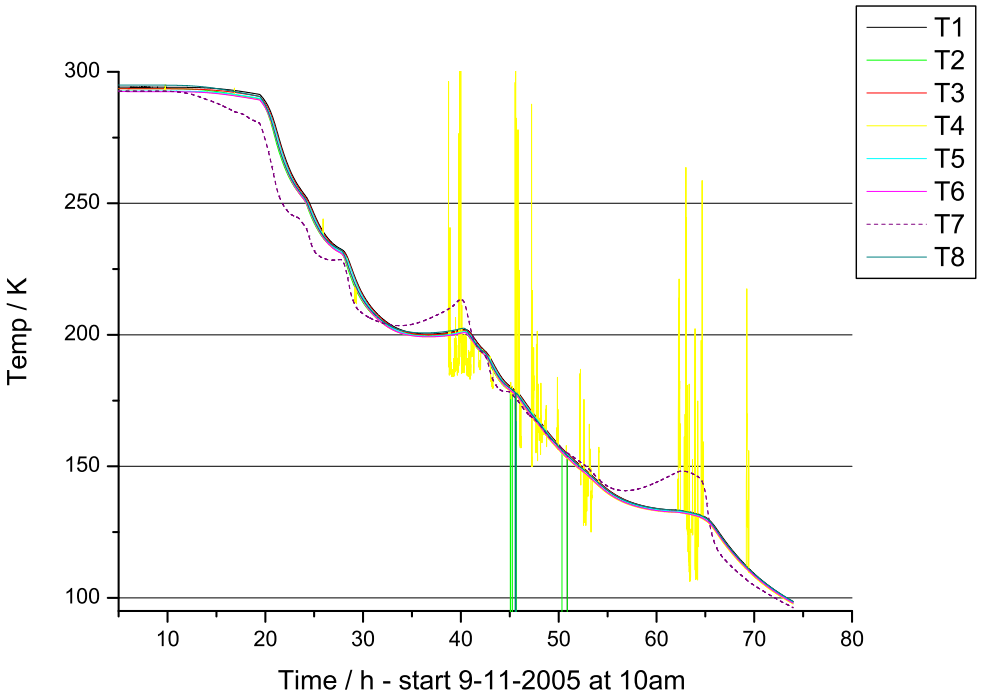

Figure 2.13: Temperatures of the system during the cool down. Eight temperature sensors are shown. T1 to T6 sensors are in the inner bore of the magnet in good thermal contact with the magnet, T7 is placed on the top of the helium vessel and measures the gas temperature, while T8 is connected to the bottom of the magnet. The magnet temperature has been very homogeneous during the cool-down. The probe with a different behavior is T7, as expected. The spike are bad readings.

keep the nitrogen level between the two probes. During the night ($\simeq$ 8 hours) the input valve into the nitrogen vessel was closed. Thanks to the liquid inside the nitrogen vessel, the magnet reduce the cooling rate to almost zero, but does not invert it, see Fig. 2.13. The first part of the cool-down ends when the the magnet temperature is lower than 100 K. The magnet can be then cooled fast to 4.2 K since the thermal expansion is not dangerous in this temperature range. The second part of the cool-down was performed flowing cold helium.

At the end of the cool-down, only the upper half of the magnet volume has been accessible to the probe holder. The estimated reason is a detected curvature of the shaft of the probe holder corresponding to a maximum 1 mm displacement from the ideal axis: the external workshop who machined the shaft from an AISI 316LN bulk round bar and

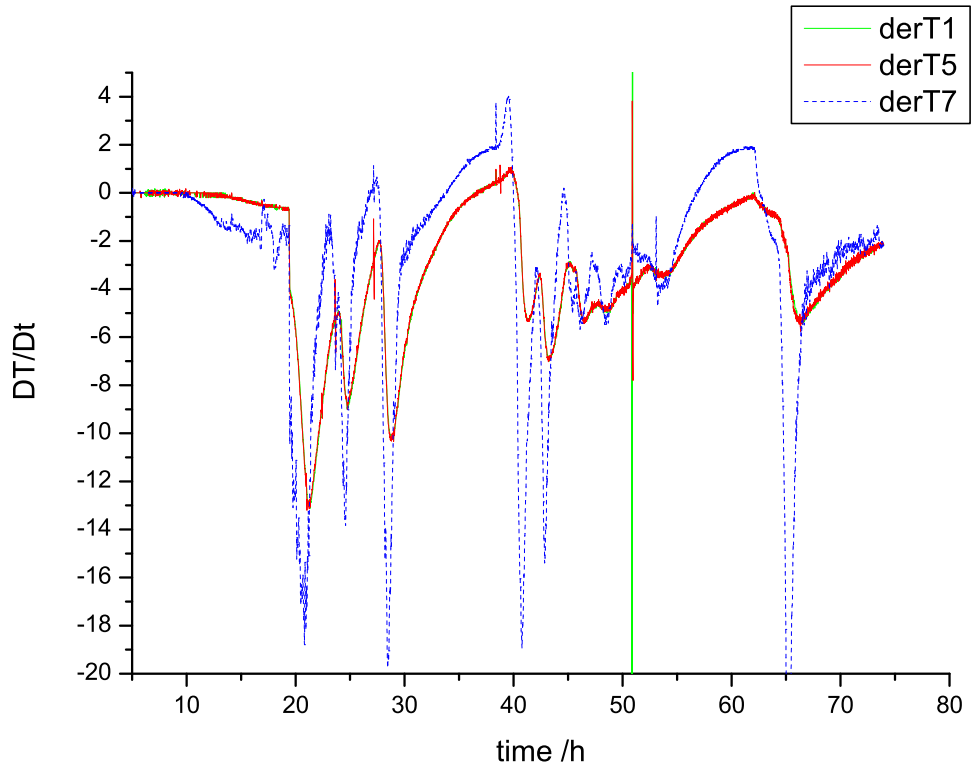

Figure 2.14: Cooling rates during the cool down. Not all sensors are shown. The cooling speed of the magnet (T1 and T5) and of the helium gas in the vessel (T7) are plotted.

heat treated the shaft did not respect the 0.1 mm tolerances requested in the project[1].

Several test have been performed before the field map measurement. A preliminary 70° scan was performed with 5° steps to find the exact position of the pole field. Scans of a single plane at different currents were performed. The field have been mapped several times at maximum current (500 A). Four complete field map where performed in three days. The quote at 117 mm from the bottom of the magnet was chosen as a reference plane. The reference plane field was measured at different currents: 51, 76, 101, 200, 250 and 300 A.

Before any measurement set, the system was calibrated measuring the pedestal signals. The Hall probes are measured by four wires, to measure the pedestal the current supply is turned off and the read values are saved in the log file.

[1]A new shaft will be manufactured in Ferrara workshop to solve this problem.

An Hall probe has been fixed to one pole tip in the center of the magnet[2].

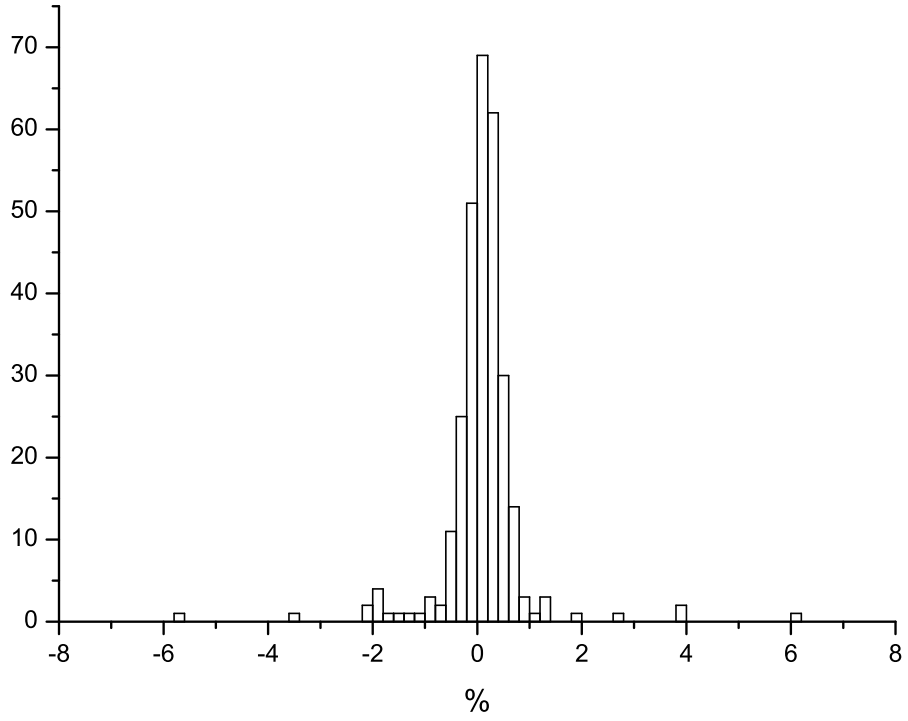

Figure 2.15: Comparison between two field map performed in two different days. The distribution of the difference between the measured values is expressed in percent.

2.4.1 Preliminary results

The measuring system showed great reliability. The measured values of two field maps performed in two consecutive days are compared in Figure 2.15. The difference between the read values are in the order of one percent, with a mean error of 0.094% and a standard deviation of $0.80 \pm 0.05\%$. Less than 10 readings were not considered because they are bad readings. The two field map have been performed at 500 A. It has to be pointed out that the differences have mainly two sources, the electronic readout that was disconnected and reconnected each day and the positioning of the measuring movement system.

The magnetic field has been measured also by a Hall probe placed on the pole tip at half of the magnet height. The measured field as a function of the currents supplied to

[2]The probe holder cannot reach the pole tip of the magnet.

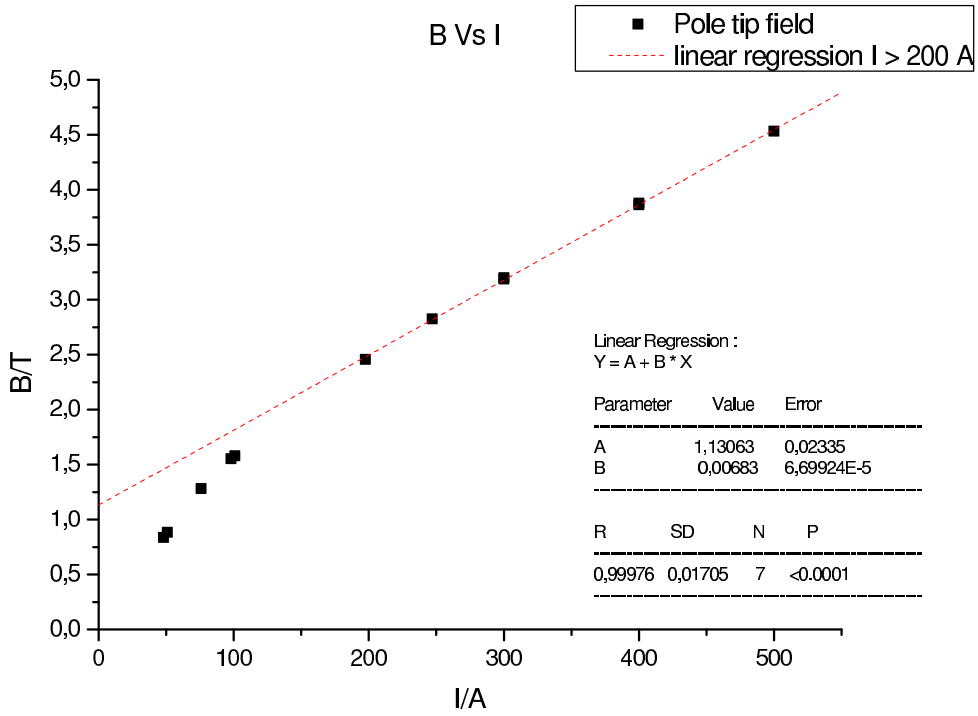

Figure 2.16: Measured pole tip field at different currents and linear regression (dashed line) of the points above 200 A. The non linearity of the points at currents below 200 A is due to the inner iron pole saturation. For currents above 200 A the pole tip field is linear, A parameter of the linear regression is the increase in pole tip field due to inner iron pole.

the magnet is plotted in Figure 2.16. The effect of the iron saturation inside the pole is indicated by the non linear behavior for currents below 200 A. Above 300 A the iron saturation is complete and the field behavior is linear. From a linear regression of high current measurements, also shown in Figure 2.16, it can be estimated that the contribution to the maximum pole tip field of the iron inside the pole is above 1 T.

The result of a scan in z direction is plotted in Figure 2.17; at nominal current the fringing field decreases rapidly.

In order to be sure to measure the field at the exact position of the pole a 70° angular scan was performed. The results are plotted in Figure 2.18. The angles used in the plot are the angles defined by the motor that rotates the hollow shaft. Table 2.1 shows the position of each channel respect to the center of the probe holder (see Fig. 2.6 and Fig. 2.7). The 60° periodicity is evident. The pole was set at 0 (or 60°) and the measurements were taken from $-2°$ to $+2°$ from the ideal position with a 1° step.

Pedestal measurement were taken before the field mapping. The pedestal signal in

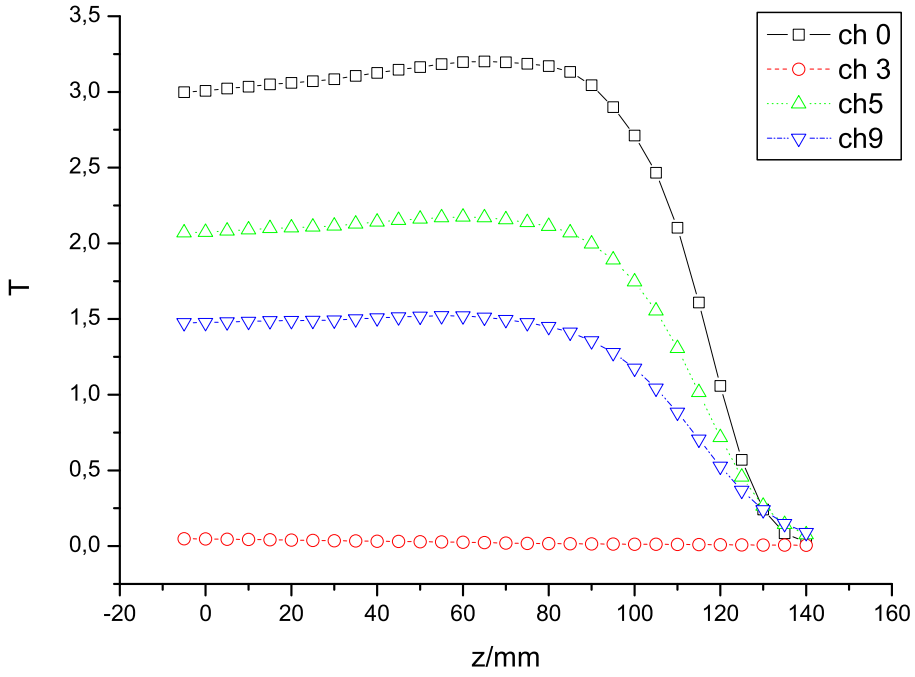

Figure 2.17: Scan along zed axis, the results are with no pedestal subtraction. The showed probes measure the radial field.

our case is the voltage read at the end of the signal wires while the current supplied to the probes is null. The 100.000 mA supplied to Hall probes during the measurement is short circuited by a relay on the multiplexer board (see Fig. 2.10) and remote controlled by PC. The current supply of the Keithley multimeter has to be turned on and short circuited because the device requires several minutes to warm up and guarantee the current stability ± 0.5 μV and if no current is flowing makes the multimeter to stop for an error when working in four wire mode. The reading mode during pedestal calibration is the same used for the normal measurement. A pedestal measurement has been performed for each measured point, all the results reported for the field mapping have the pedestal subtracted.

The field harmonics measured at maximum current are reported in Figure 2.19. The normal field harmonic A_i, the ratios of the component respect to the sextupolar component A_i/A_3, the skew components B_i and the ratios of the skew components respect to sextupolar component B_i/A_3 are plotted. The results are reported for each measured transversal plane, the lower part of the magnet was not accessible due to the mechanical

Ch0	Ch1	Ch2	Ch3	Ch4	Ch5	Ch6	Ch7	Ch8	Ch9
R -45	T +15	R +40	R +00	T +26	R -35	R +30	R +35	T +37	R -30

Table 2.1: Channel number used for the ten Hall probes, in second line is reported if the probe measures radial (R) or tangential (T) field and the distance in mm from the center of the probe holder (see 2.6 and 2.7)

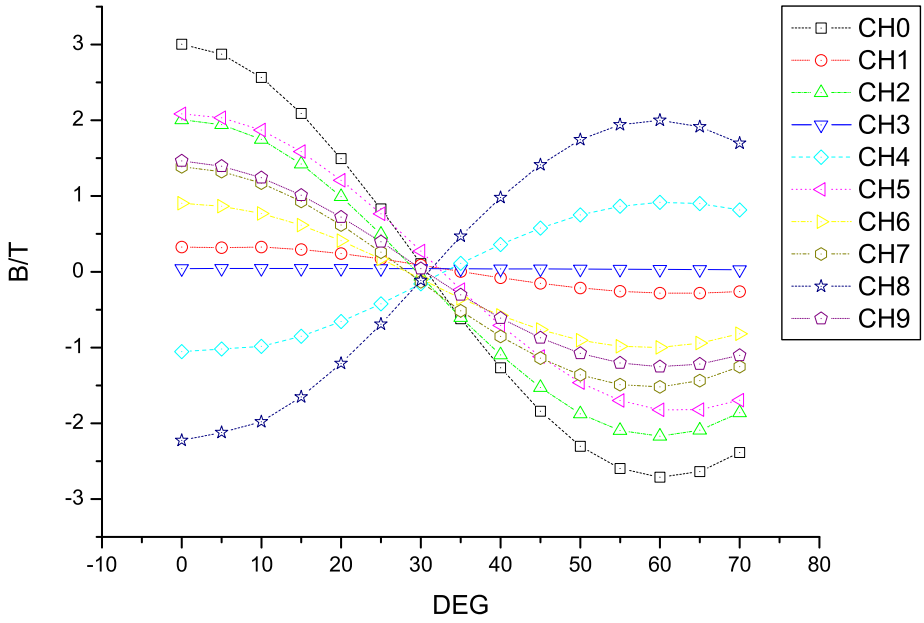

Figure 2.18: Field measured by all ten Hall probes in the 70° scan to search the pole position.

problems mentioned above. The magnet harmonics are quite constant along z direction in the measured half of the magnet. The measured magnetic field has important quadrupole and 8-pole harmonics, the relative magnitude (respect to sextupolar one) are approximatively 10^{-2}. This not-sextupolar components contribution is compatible with an atomic beam source application. The field harmonics measured and the relative intensity respect to the sextupolar component for different currents from 1 A to 500 A are reported in Figure 2.20. The measurement at 1 A was performed at room temperature (see section 2.2) while all the others were performed with the magnet in helium liquid bath at 4.2 K. The iron inside the poles of the magnet saturates in the 200-300 A current range. Field components ratios A_n/A_3 and B_n/B_3 for measurements at low temperature and moderate currents (before iron saturation) are compatible with the ones performed at high

temperature at CERN. The quadrupole component A_2 at currents above 300 A increases while the 8-pole component is compatible with the measured values at low current. At high currents also the skew quadrupole component increase and the 8-pole component is constant. The increase of the quadrupole component at full current, which can originate from a non complete uniform saturation of the iron poles, is modest and does not spoil the sextupole performances in an ABS.

Magnet voltage

The LabView program that monitors the cryostat and include the software quench protection has been implemented to save the coils voltages in case of quench. In Figure 2.21 is reported a screen shot of the control panel after a quench. The voltage across coils, magnet temperatures and liquid helium level monitors are visible in the lower part while the buffering system dedicated to the acquisition of voltage waveform are visible in the upper part where the signal from the hardware quench protection system and the voltage across the six coils read by a digital scope are shown (right). The voltage across the coils is saved in a circular buffer. Figure 2.22 shows the voltages saved by the program; the moment in which the (software) quench protection system triggered is also shown. The voltages of this magnet do not show peaks before the quench. The magnet was not able to support currents above 505 A, the coil number 5 quenched several times in the 500-505 A range. This coil resulted the most delicate one already during the training of the magnet (see [22]).

2.5 Conclusion

A test bench for precise fast and reliable multipolar mapping, developed as a part of the thesis work, was here presented. An update of the setup is planned to solve the problems encountered. The cool-down and field mapping of a prototype sextupole magnet characterized by iron inside the pole support has been reported. The magnet field mapping at room temperature and low temperature has been presented. The effect on the field due to iron magnetic saturation have been measured. The magnet was manufactured in the Ferrara workshop. The field properties are suitable with the use in an atomic beam source focalization system and will be used for a superconducting ABS prototype.

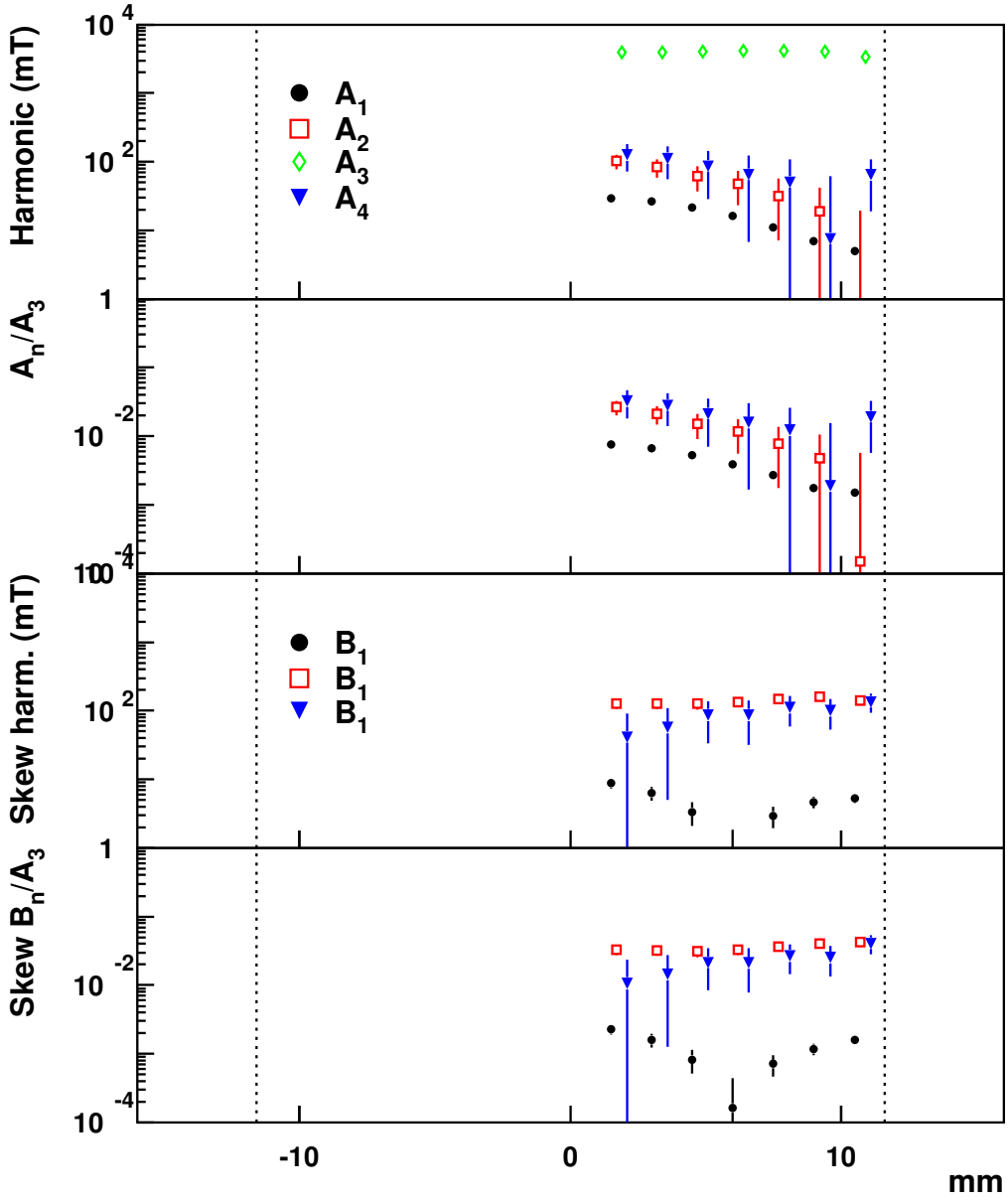

Figure 2.19: Measured harmonics at 500 A.

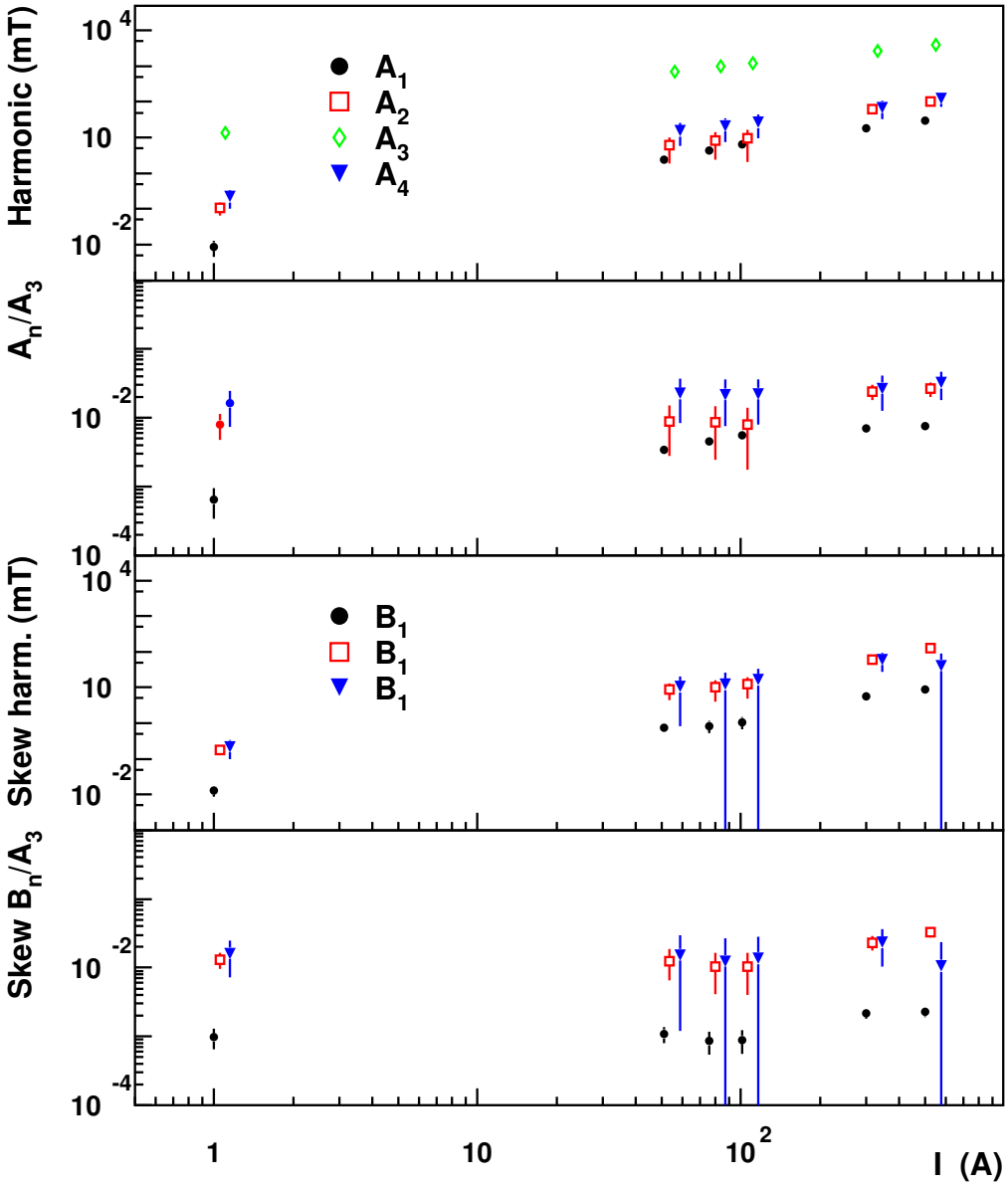

Figure 2.20: Measured harmonics in the reference plane (z=0 mm at the center of the magnet) at different currents.

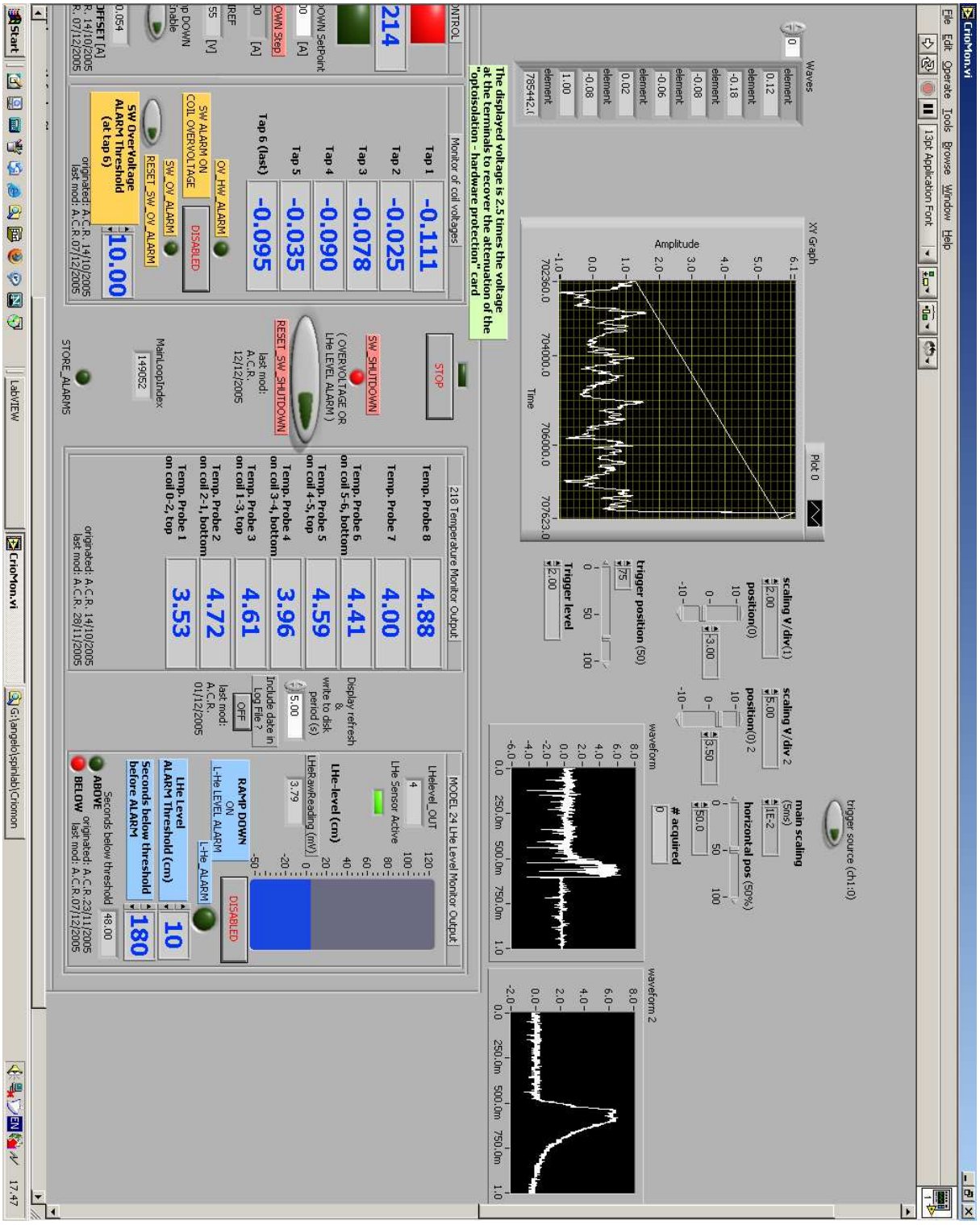

Figure 2.21: Screen shot of the LabView program monitoring the cryostat, the magnet and providing software (secondary) quench protection. 'Wavwform 2' is the voltage across the six coils and is read from a scope.

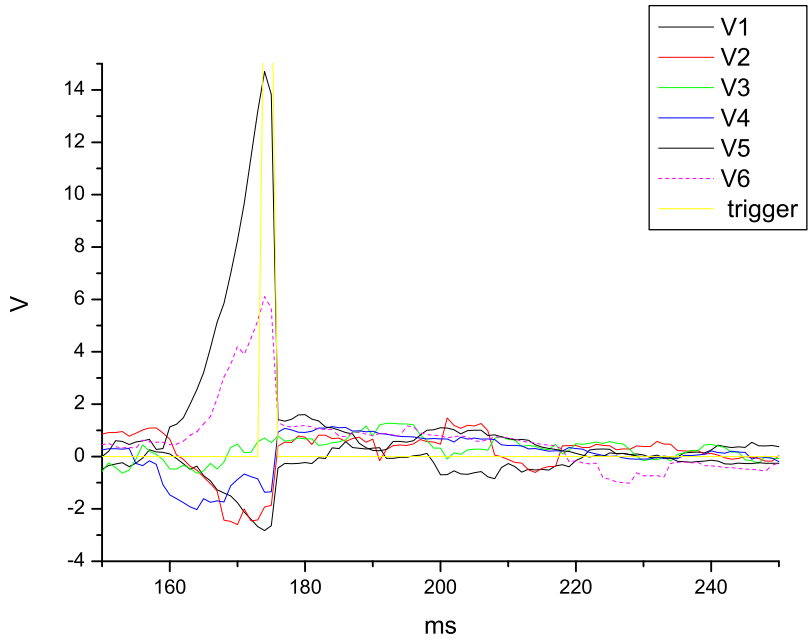

Figure 2.22: Voltages across the six coils during a quench. Trigger shows the position in the circular buffer where quench occurred.

Chapter 3

The PAX toroidal superconducting magnet

The design of the toroidal superconducting magnet of the PAX [1] detector tracking system is presented. Details on the field requirements, constrains and the proposed solution are explained in this section.

3.1 Magnetic Field Configuration for tracking

The spectrometer magnet has to be compatible with the holding field of the target polarization and the Čerenkov detector which needs to work in a field free region to efficiently identify leptons, see for details Appendix A. A toroid configuration satisfies both requirements resulting in a negligible fringe field both along the beam line and inside the external volume where the Čerenkov detector is located. A toroid field is always orthogonal to the particle momentum, hence the bending effect is optimized regardless of the scattering angle. An eight–coil configuration can be designed to give excellent coverage over the azimuthal angles, facilitating the detection of the $\cos(2\phi)$ modulation of the transverse asymmetry, covering the region around $2\phi = n\pi$, where the sensitivity is largest (see Fig. 3.1). The azimuthal acceptance is optimized by placing service and support structures of the various detectors in the shadow of the toroid coils.

3.1.1 Mass resolution

A lepton pair invariant mass resolution close to 1 % is required to isolate the resonance signals from the continuum. This value necessitates a momentum resolution of the same order of magnitude for lepton tracks with a momentum range between 0.5 and 10 GeV/c. As a consequence, the maximum value of Δp around $\sim$ 0.3 GeV/c is required in the

[1] Proton Antiproton eXperiments, details in Appendix A

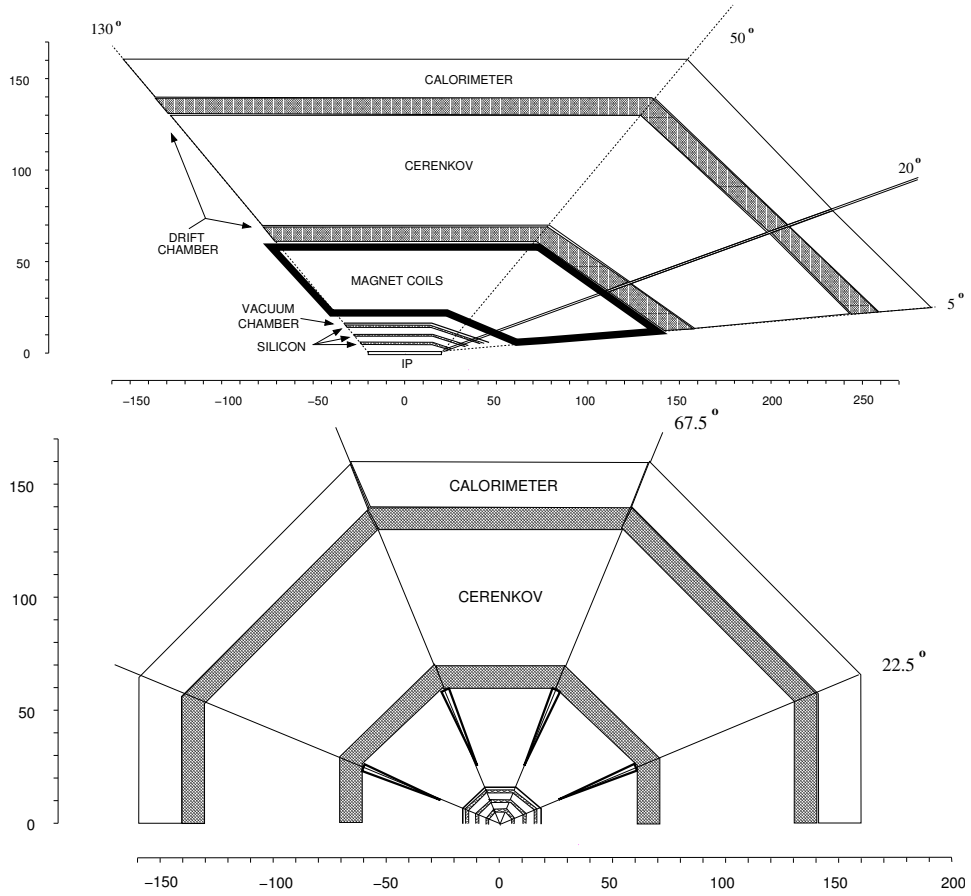

Figure 3.1: Sketch of the PAX detector, showing a side view ([z, y], top) and a view in beam direction ([x, y], bottom). The optional forward detector, sensitive at laboratory polar angles between 5° *and* 20°*, is also indicated.*

forward region where the particle momenta are larger. Such a momentum kick is provided by an integrated field along the particle trajectory of $Bl \sim 1$ Tm. In order to limit the cost of the external electromagnetic calorimeter, the detector should be compact: by assuming a magnet length of 70 cm in the forward direction, the required magnetic field is of the order of 1.5 T. A transverse momentum kick of $\Delta p \sim 0.3$ GeV/c puts constraints on the position resolution of the tracking detectors to achieve the required momentum resolution. At a momentum of 10 GeV/c, the deflection angle equals about 2°. A model calculation shows that an uncertainty in the position lower than 30 μm (200 μm) in the inner (outer) tracking region is needed to obtain a relative momentum resolution of about 1 %. This resolution can be provided by conventional silicon strip detectors (SiD) close to the target and drift–chamber modules (DCH) outside the magnet. The high spatial resolution provided by the silicon detector will help to identify the background leptons from secondary vertex (like $D^{\pm}$ decays). The required momentum resolution can

only be achieved by keeping multiple scattering in the magnetic field region small. If only multiple scattering is taken into account, the momentum resolution of ~ 1 % at the smallest accepted momenta of 0.5 GeV/c requires an effective thickness less than 0.05 radiation lenghts X_0 [25]. The amount of material in the tracking region should be minimized also to reduce the gamma conversion probability and energy loss by radiation. The first active tracking layers placed inside the target vacuum chamber can be used to veto gamma conversions as close as possible to the interaction point.

3.1.2 The gaseous Fixed-Target

Hydrogen pure nuclear polarization needs an holding magnetic field of the order of 300 mT [16]. A normal conductive iron cored dipole is not compatible with a central detector. A possible solution in order to build central detector in experiments using transverse gaseous polarized targets is the use of light superconducting coils magnets [26]. The combination of light superconducting coils and a toroidal magnet for tracking is compatible with both longitudinal and transverse polarized target since the target holding field is decoupled from the tracking one. The storage cell of the gaseous target is inserted upstream of the detector (IP in figure 3.1). The atomic beam source (ABS) and the injection tube of the cell are placed in the empty solid angle in front of the detector. The polarized gas atoms leave the target cell through the open ends and are differentially pumped by two stages along the beam pipe. This minimizes the degradation of the vacuum and thus its effect on the stored beam. The transition from the cell to the beam pipe could be made smooth using perforated tubes, to avoid the possible generation of wake fields that could cause heating and increase the emittance of the beam. Given the importance of the acceptance in the forward direction, the first pumping system at the cell position is located upstream, like the ABS. The vacuum region extends inside the conic–shaped internal space of the detector and reaches the second pumping system located just behind the CAL. Particles scattered into the detector exit the vacuum region through a 0.3 mm stainless–steel foil (corresponding to 0.5 % of radiation length) stretched by the toroid coil supports.

In order to minimize the material inside the detector acceptance, the magnet is composed of a couple of superconducting coil surrounding the target, parallel to the horizontal plane and providing a vertical field of about 0.3 T in the cell volume. The higher current density of the superconducting coils with respect to copper coils allows a lighter design. The use of superconducting materials such as MgB_2 can be cooled down by cryoheads instead of liquid bath guarantees a very light design. An example of a possible design is reported in figure 3.2, where a 700 mm long pair of symmetric superconducting coils is placed inside the shadow of the toroid coils at 14 mm and 34 mm from the x and y axis respectively and thus the system acceptance is not affected by the target magnet. The coils have a 2×10 mm^2 cross section and a current density of $J_e = 800\, A/mm^2$. The field of around 300 mT in the target region (z=$\pm$200 mm, x=$\pm$10 mm and y=$\pm$5) is shown

in Figures 3.3, 3.4 and 3.5. The field along the z (beam) direction plotted in Figure 3.6 shows the values of the integrated field affecting the accelerated beam, the zone affected by the beam is relatively short. The integrated field along beam direction is 0.2 Tm, and the z and x integrated field are negligible.

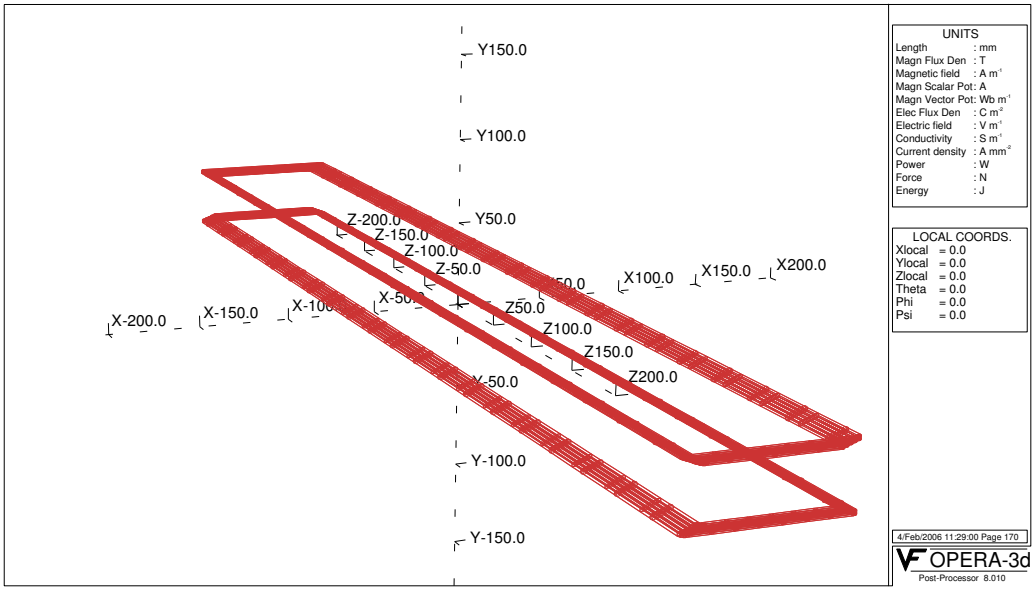

Figure 3.2: Target magnet coils.

The magnet is inside the vacuum region to provide thermal insulation. Four correcting dipoles are added to the beam line to compensate the effect of the PAX magnets on the orbits of the protons and/or antiprotons. For the case where longitudinal target polarization is required, the transverse field will be ramped down. If only one hyperfine state is injected, a longitudinal holding field of some mT is sufficient and can be provided by conventional Helmholtz coils. (When only one hyperfine state is injected in the target, spin–relaxation processes like spin–exchange collisions are practically absent and the condition for a strong holding field is consequently relaxed.)

3.1.3 Particle deflection

In most particle physics experiments a magnet is used to identify the particles emanating from the interaction. Uncharged particles traverse the field without being affected while particles having positive charge will be deflected to one side and the ones having negative charge to the other. This provides a first information about the particle charge. The deflection of the charged particle depends on strength of the field, the length of the

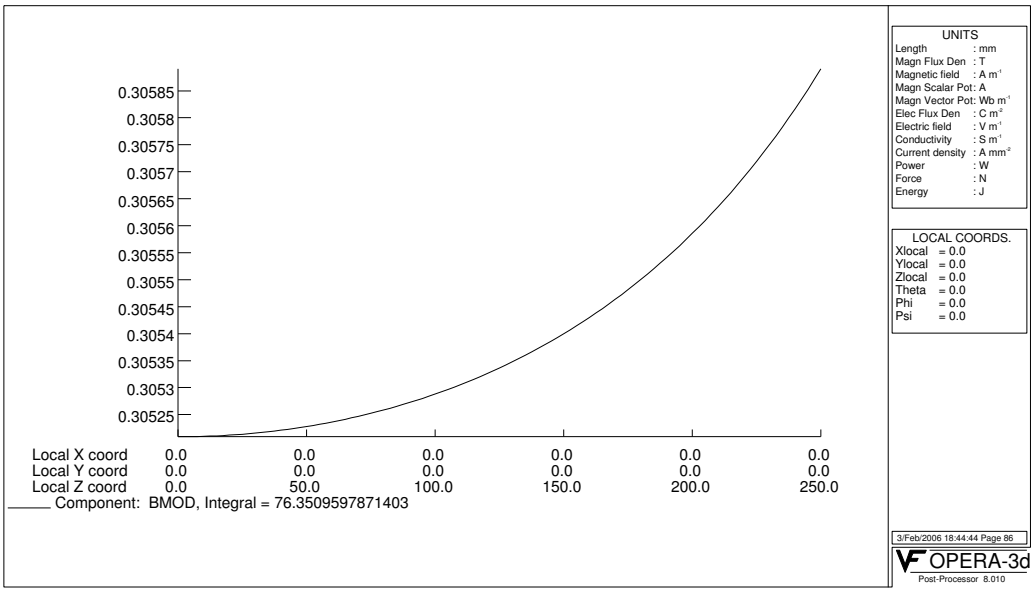

Figure 3.3: Component in y direction of the magnetic field on the target region (z=±200mm). The field is symmetric.

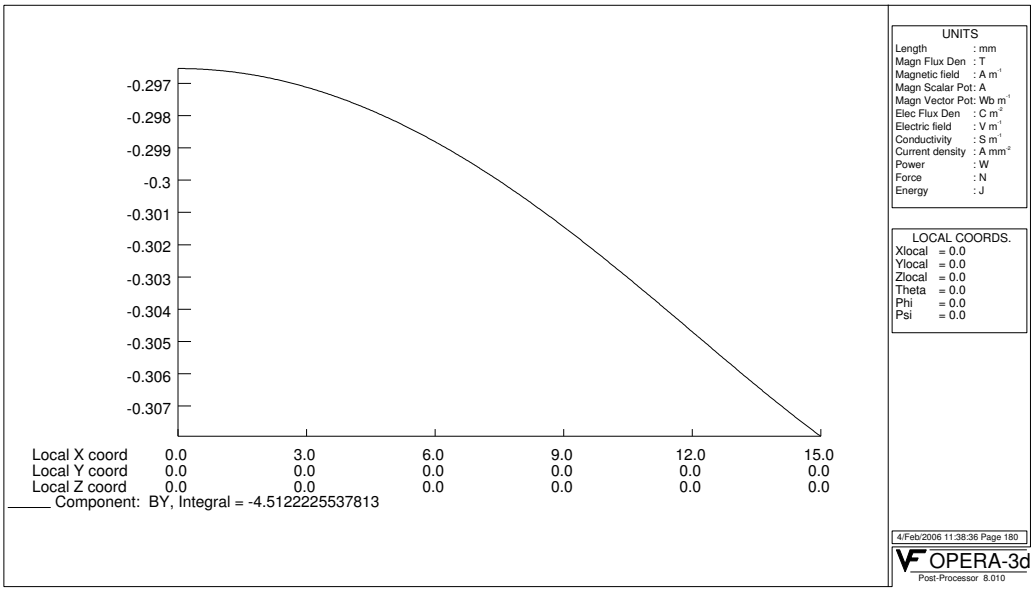

Figure 3.4: Component in y direction of the magnetic field on the target region (x=±15mm). The field is symmetric.

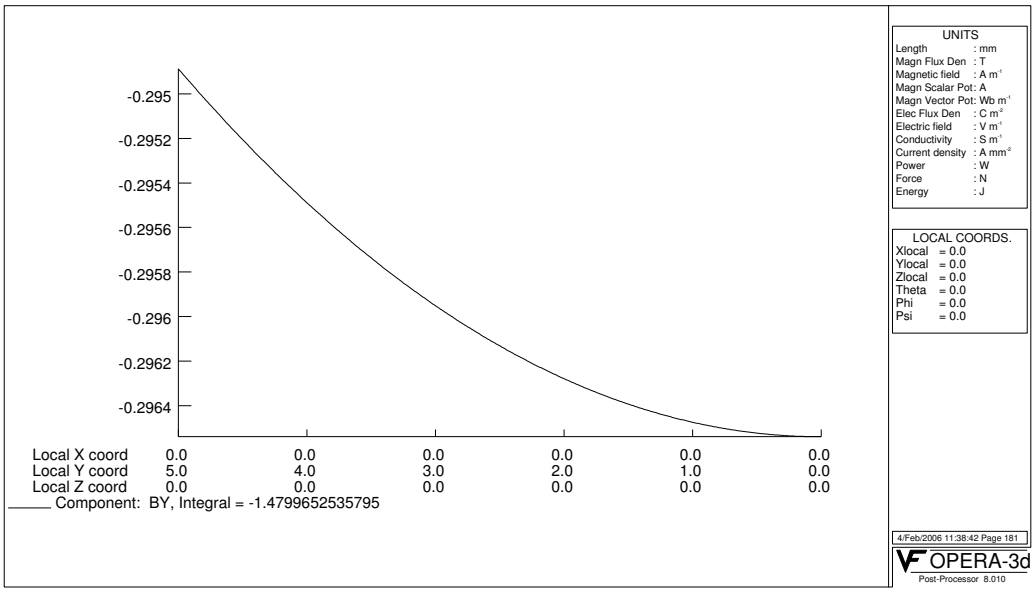

Figure 3.5: Component in y direction of the magnetic field on the target region (z=$\pm$5mm). The field is symmetric.

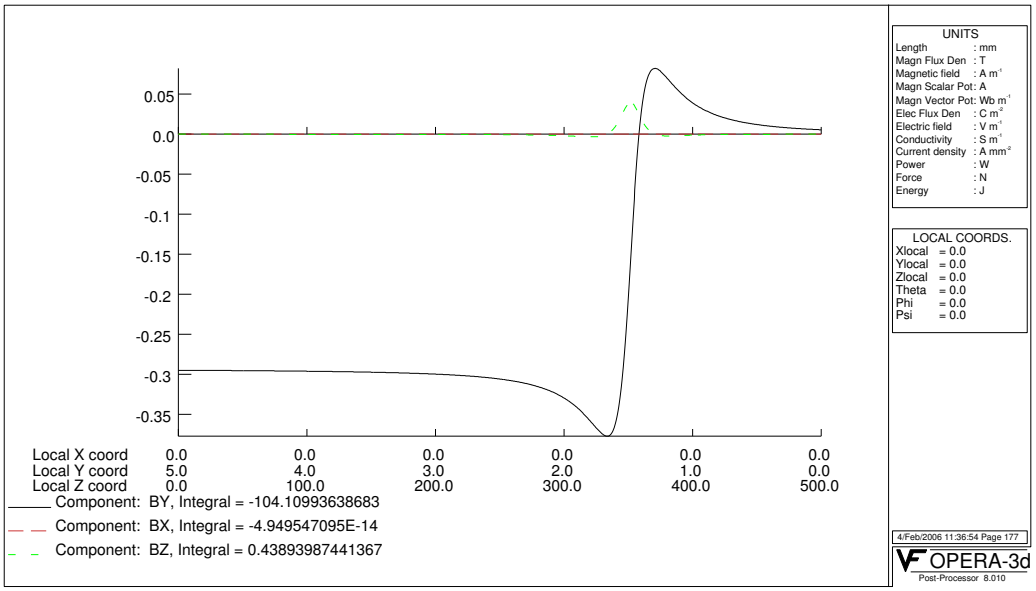

Figure 3.6: Field components along the accelerated beam axis (z) and integrated field. The field is symmetric. The total integrated field in y direction is $0.2Tm$*, while x and z field are negligible.*

trajectory in the field and the momentum of the particle. The size and strength of the magnetic field can be measured, so by measuring the deflection the momentum can be found.

The force exerted on a particle of mass m carrying charge q and traveling at velocity v in a magnetic field B is given by

$$\bar{F} = q\,\bar{v} \times \bar{B} \tag{3.1}$$

In case of uniform and perpendicular field respect to the motion, the particle will follow a trajectory which is a circle of radius r where

$$r = mv^2/|\bar{F}| \tag{3.2}$$

The momentum p of the particle is equal to mv, so after some simple algebra we can write equation 3.3, representing the angle Ψ through which the trajectory is deflected.

$$\Psi \simeq L/r = q\,B_\perp\,L/p \tag{3.3}$$

where L is the path length in the magnetic field having component $B_\perp$ perpendicular to the path. The sagitta s of the trajectory is then

$$s \simeq \frac{qB_\perp L^2}{8p} \tag{3.4}$$

In practice the track detectors record the trajectories in the field and the measurements are made of s or Ψ. In case of non point like targets, the trajectory have to be measured before and after the particle crosses the tracking field. The precision with which the momentum can be measured depends on the precision of these measurements and the magnitude of L and $\bar{B}$. Note that the momentum measurement largely benefits from a direction of the field as much as possible perpendicular to the particle trajectory.

3.2 Large angle detector magnets: solenoids and toroids

The detectors magnets basically have three configurations: solenoid, toroid and dipole. The dipole magnets are not very suitable for large angle detection because the field is transversal with respect to the beam axis and at large scattering angles the bending force vanishes along the field direction. These magnets are optimal for low angle particles, typical for forward spectrometers and will not be discussed furthermore.

3.2.1 Solenoids

Solenoids are conceptually simple, elegant and very effective. The vast majority of recent 4π detectors at colliders have relied on solenoidal type magnets, producing a cylindrically

symmetric field having the same axis of the colliding beams. They are also used for fixed targets and cosmic rays experiments. The reason for this is that the symmetric 2-D field is fairly uniform and this facilitates tracks reconstruction of the events; there is no material within the field volume to give rise to spurious secondary interaction, and the magnetic forces are relatively easy to contain. In case of a continuous solenoid, not split in coils, all particles inside the acceptance have to cross the conductor before exiting the magnet.

When solenoidal magnets are used, the interaction point or region is in the center of the magnet, where the field is maximum, this is of course not compatible with a transverse magnetic field, like the one required for a transverse polarized target. The bending force of the solenoidal field is null on the longitudinal axis, so that the solenoid is typical for high angle spectrometers. The effect of the solenoidal field on a particle accelerator is not negligible and require skew quadrupoles to correct for the coupling of vertical and horizontal betatron oscillations.

The length of trajectory of a charged particle emanating at zenithal angle Θ from an interaction on the axis of a long solenoid of radius R producing a static magnetic field B, is $R/sin\Theta$ considering zenithal angles approx 90° since solenoid are generally used for high angle particles. The component of field perpendicular to the trajectory is $Bsin\Theta$. Using equations 3.3 and 3.4 the change of angle, $\delta\Theta_{solenoid}$, and the sagitta $s_{solenoid}$ of the trajectory are therefore

$$\delta\Theta_{solenoid} \approx q\,B\,R/p \tag{3.5}$$

and

$$s_{solenoid} \approx \frac{B\,R^2}{8p\,sin\Theta} \tag{3.6}$$

The 'analyzing power' depends on the layout of the detector and is obtained by some combination of measurements of sagitta and changes in angle; this is reduced at small angles because of the finite length L of the solenoid. In fact in a solenoid the momentum is usually analyzed by measuring tracks inside the magnet, and the momentum resolution $(\delta p/p)$ solenoid scales as follows:

$$(\delta p/p)_{solenoid} \approx \frac{p\,sin\Theta}{BR^2} \tag{3.7}$$

Within the limits of known technology and transportable size, the cost of the solenoid of length L_s is roughly proportional to $L_s R^2 B^2$. It is therefore clear that, as concerns resolution, it can be preferable to invest in size than in central field.

3.2.2 Toroids

In theory a toroidal magnetic field is ideal, both for a 4π detector at a colliding beam facility and for forward and fixed target detectors. The field is symmetric and perpendicular to the particle motion. The integrated field along the trajectory of a particle increases as

Θ decreases, which is favorable because the likelihood of having high energy particles to analyze increases as Θ decreases. Charged particles produced on the axis are deflected in a plane simplifying the pattern recognition. There is no iron yoke. And there is no field along the axis of the beams. For an ideal toroid contained between current sheets at radii R_i (inner) and R_o (outer) and with field B_i at the inside radius, the deflection $\delta\Theta_{toroid}$ and the sagitta, s_{toroid} of the trajectory within the field, are given by

$$\delta\Theta_{toroid} \approx \frac{q\,B_i\,R_i}{psin\Theta} ln(R_o/R_i) \tag{3.8}$$

and

$$s_{toroid} \approx \frac{q\,B_i\,R_i^2}{10psin\Theta} \tag{3.9}$$

the latter assuming a typical ratio of 3 for Ro/Ri. For toroids the change in angle is usually used for the momentum measurement, and the resolution can be expressed as

$$(\delta p/p)_{toroid} \approx \frac{p}{B\,L} \approx \frac{p\,sin\Theta}{B_i\,R_i} ln(Ro/Ri) \tag{3.10}$$

In this idealized case the optimum resolution is obtained with $R_o/R_i \approx 3$, but this optimum is quite flat and is only reduced by 5% for a ratio of 2 and a ratio of 1.5 leads to a reduction of 25%. The reason why so few toroids have been built till now respect to solenoids is mainly because of the difficulty of making in practice anything resembling an ideal toroid, i.e. to make the inner conductor sheet and its supporting structure sufficiently transparent, or to divide it up so as to cover a sufficiently small proportion of the azimuth, and to make it sufficiently long. This material creates confusion in that some particles are absorbed or interact with the structure, an effect that can easily outweigh the benefits of conceptual elegance. Various studies made over the last 25 years have concluded that the best practical approximation for a high field (and therefore superconducting) toroid, covering the central region of the detector of a collider experiment, consists of a small number of flat pancake coils (typically eight). With care these can be made to cast shadows over as little as 30% of the azimuth, which can be considered acceptable.

In comparing solenoids with toroid advantages, one should consider that iron yokes double as calorimeters; the compensation of the effects of solenoids on the circulating beams is fully understood and is not onerous; For a racetrack toroidal coil geometry the field is far from being uniform and requires a detailed field map for tracking. The field on the inside conductor of a typical toroid is about four times the maximum field in the useful part of the magnet (compared with about 1.3 times for a typical solenoid). This is unfavorable in the case of a superconducting coil working at very high fields but a polarized gaseous target require a holding field which can have longitudinal or transverse orientation. An important advantage is then to have the target holding field and the tracking one completely independent. As an example, the HERMES experiment is able to run both polarized and transverse polarized targets since the tracking dipole of the

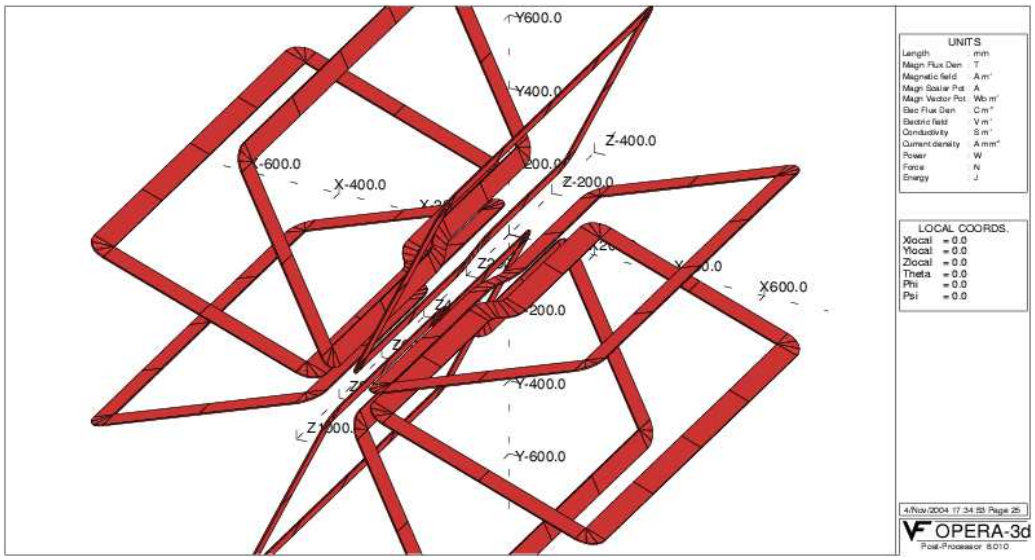

Figure 3.7: Artistic view of the 8 coils toroidal magnet for the PAX spectrometer.

forward spectrometer is independent from the polarized target holding field [27]. The momentum resolution of a solenoid decreases with the zenithal angle and Equation 3.7 is valid for angles near 90° and the particle is not deflected when its trajectory is parallel to the solenoid longitudinal axis. For toroids the particle deflection increases at lower zenithal angles (see Eq. 3.8); this feature is suitable with energy spectrum of the detected particles.

3.3 The PAX superconducting toroid conceptual design

The request of both a zero field in target region and high compactness of the PAX experiment detector are fulfilled by a toroidal magnet. The charged particles coming from the target region entering the magnet are bent by a magnetic field that is orthogonal respect to the particle's path at any angle. The bending force increases inversely proportional to the radial distance and zenithal angle, greater bending power is available for particles scattered at smaller angles, which have higher momenta.

The toroid superconducting coils are actually in use in particle detectors (HADES [28], CLAS [29], BLAST [30], ATLAS [31] [32] and at KEK-PS [33]), fusion projects (ITER [34] and KSTAR [35]) and Superconducting Magnetic Energy Storage projects [36][37]. The acceptance of the detector, i.e. the fraction of space through which a particle exiting from the interaction region is detected by the active part of the detector, is one of the most important parameters in the design of an experiment. A complete toroid is not feasible

because of the amount of the material put along the particles path, which hugely reduces the resolution of any detector behind the magnet or makes it blind. In order to reduce the overall dimensions of such a magnetic field generator, a series of superconducting coils can be used [33]. The superconducting and cryogenic technologies allow to reduce the width of each toroid coil respect to copper coils because the higher current density in superconductors. The toroid coils reduce the azimuthal acceptance because they are made up of bulk Aluminum, Copper and superconductor material (high atomic mass alloy) and if a particle hits them a shower is generated. An high azimuthal acceptance is attained using a reduced number of superconducting coils, typically six or eight. In order to increase as much as possible the acceptance, two support rings are placed upstream and downstream the target-spectrometer system. The upstream one hosts the supply lines for electric power and for liquid helium. At the downstream toroid end, an hexagonal plate compensates the magnetic forces to hold the coils in place. Additional mechanical reinforcements are placed on the inside of each coil preventing planar deformation. These reinforcements, placed in the coils's shadow, do not affect the detector acceptance.

The cost of the overall PAX detector is influenced by the length and diameter of the tracking magnet. The detector's cost are in first approximation proportional to the surface to be covered. The choice of a eight coils superconducting toroidal magnet is a trade off between high acceptance request and small overall dimensions. The inner and outer dimensions are influenced by several parameters: the space for the target (and target magnet), the need of high integrated field Bl for low angle particles. The request to the outer diameter of the magnet is to be less than 70 cm to contain the total detector cost.

The target, its magnet and the vertex detector need a 300 mm diameter and $\pm$400 mm long cylinder of free space. To achieve a $\sim$ 1 % momentum resolution in the PAX spectrometer, an integrated field above 1 Tm is required in the forward region where low angle (20°) particles have few GeV momenta. An integrated field of 0.35 Tm is sufficient in the central region since the particles scattered at large angles have a momentum peaking at 1 GeV. The coils are shaped in order that in the region downstream the target the minimum distance from the accelerated beam axis is 150 mm. The total length of the magnet is then 1800 mm. The center of the target region is placed inside the magnet 400 mm from the upstream magnet limit (fig. 3.1).

TOSCA simulations have been used to design the coils. The calculated field in the transverse xy plane is plot in figure 3.11, where z is the accelerated beam axis, x and y are the transverse horizontal and vertical axis, respectively. The field inside and outside the toroid are negligible as requested by design parameters. It has to be notice how the negligible field zones for the target and the Čerenkov detector does not require any magnetic shielding. The eight coils superconducting toroidal magnet (see Fig. 3.7) is characterized by a maximum tracking field of 2.0 T and maximum field on the coils of 3.2 T as shown by the calculated field on the zy plane in Figure 3.10. Such fields are not large enough to put severe limitations to the critical current of the superconductor. The

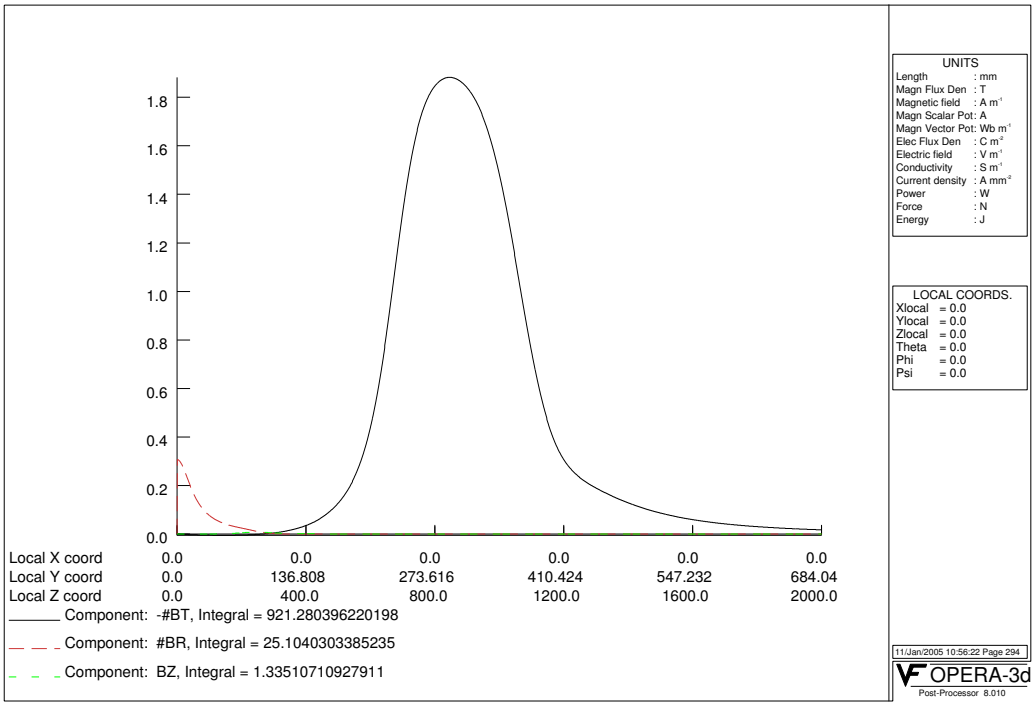

Figure 3.8: TOSCA calculation of the integrated field at a zenithal angle of 20°.

calculated field profile along a sample of particle trajectories (approximated by straight tracks at 20°, 45° and 135°), together with the field integral, are plotted in Figures 3.8 and 3.9.

The main coil's parameters are listed in Figure 3.3.

3.3.1 Cross section

The superconducting coils width directly influences the detector's acceptance. In the conceptual design a great effort was made in order to decrease the coils width down to 3 mm, corresponding to about 3 layers of superconducting $\Phi_{bare} = 0.75 - 0.85\ mm$ strands coiled, where Φ_{bare} is the strand diameter without electrical insulation ($0.100 - 0.150$ mm thick). TOSCA simulations show that, with an engineering current density $J_e = 1450\ \frac{A}{mm^2}$ at 5 K and at 4 T maximum field, a 3×100 mm^2 cross section is sufficient to obtain the 2.0 T maximum field in the tracking volume and the required ~ 1 Tm maximum bending integrated field.

The used engineering current density of $J_e = 1450\ \frac{\mathrm{A}}{\mathrm{mm}^2}$ at 5 K and 4 T is a reasonable performance for a future superconducting Nb_3Sn cable. Considering a mass ratio Copper over superconductor around 1, the required specific current density for the superconductor is $J_c = 3000\ \frac{A}{mm^2}$. This value is reasonable for a commercial wire in the future since it has already been reached for test strands [38, 39]. The coils are supposed to be cooled by

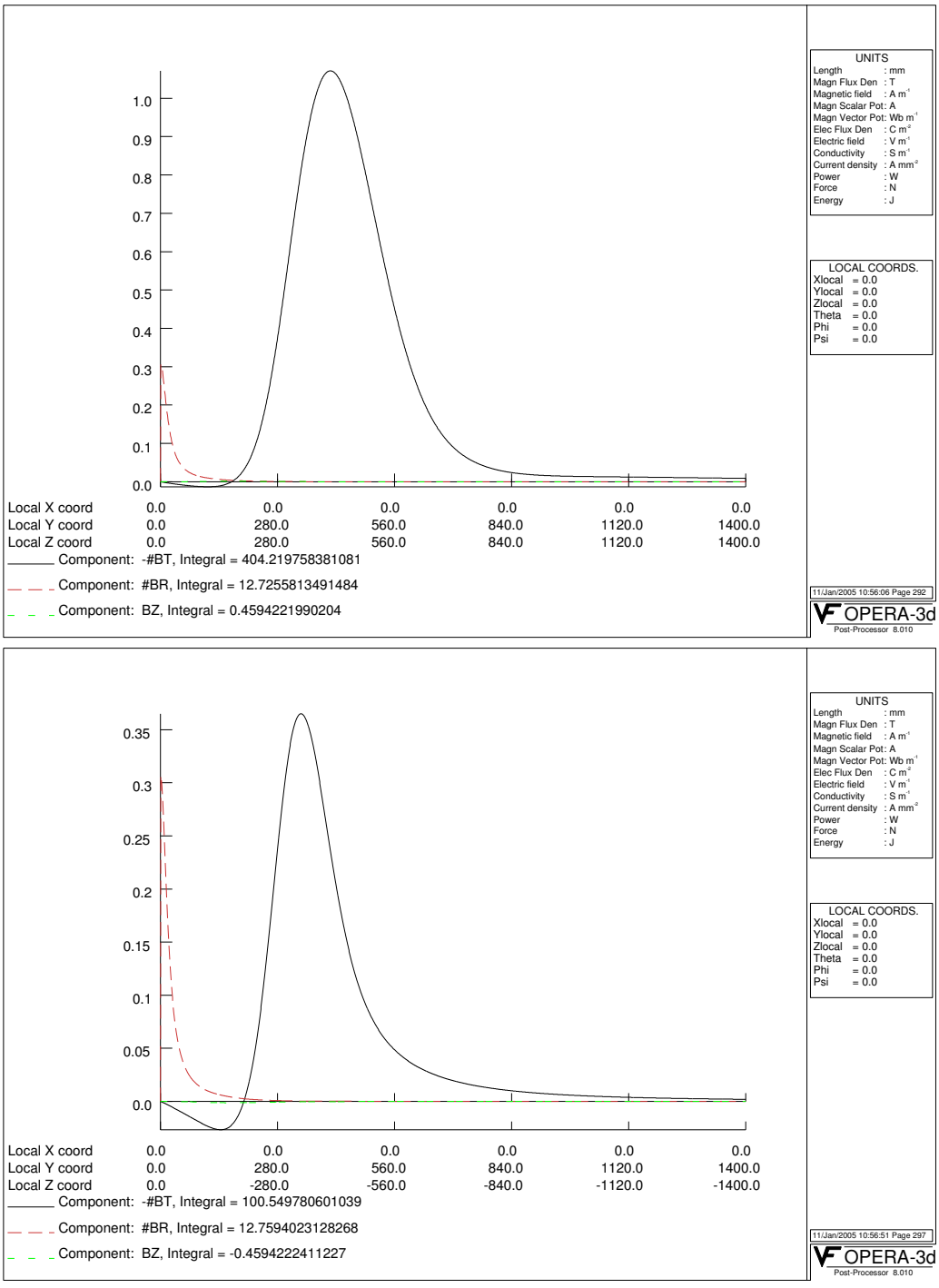

Figure 3.9: TOSCA calculation of the integrated field at a zenithal angle of $45°$ *(upper) and* $135°$ *(lower).*

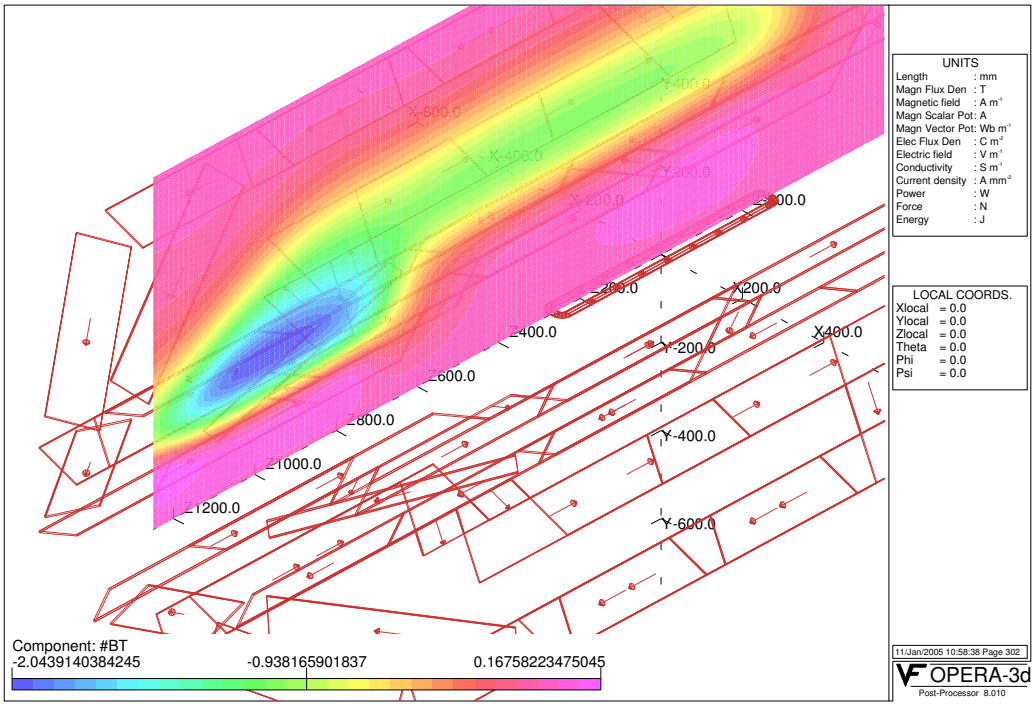

Figure 3.10: The magnetic field in the yz plane, the plane is azimuthally equidistant from 2 coils

liquid helium, by flowing inside pipes in thermal contact with (or internal to) a layer of aluminum that covers the superconducting coil to cool and support it. The temperature of the coils is then around $4.5 - 5.5\ K$.

Considering latest successfully tested SC toroidal coils [40] the superconductor Aluminum case cross section can be $12 \times 300\ mm^2$. Possible coil planar supports can be added inside the coil to increase the stiffness. A mechanical stress analysis and support design has not yet been performed at this stage of the project.

The coils require a thermal insulation. There are two main ways to thermally insulate the SC coils: a standard cryostat for each coil or only one vacuum chamber containing the 8 coils. First solution requires a warm wall surrounding each coil and vacuum between the coil's Aluminum and the warm wall itself, in that case the thermal insulation, that is composed by a vacuum vessel, multilayer insulation and eventually an intermediate temperature surface have to be at least 5 mm. The tracking planes inside the magnetic field are in this case at atmospheric pressure and the insulating vacuum of each coil is independent from each other's. Second solution consist in a bigger vacuum chamber that includes all 8 coils using a thermal insulation composed by a thermal screen (a cold envelope) and multilayer insulation not thicker than 1.5 mm, with overall $15 \times 303\ \mathrm{mm}^2$ coils' dimension. In that case the tracking planes inside the magnetic field must be suitable with high vacuum ($p < 10^{-5}$ mbar), moreover all detected particles have to cross

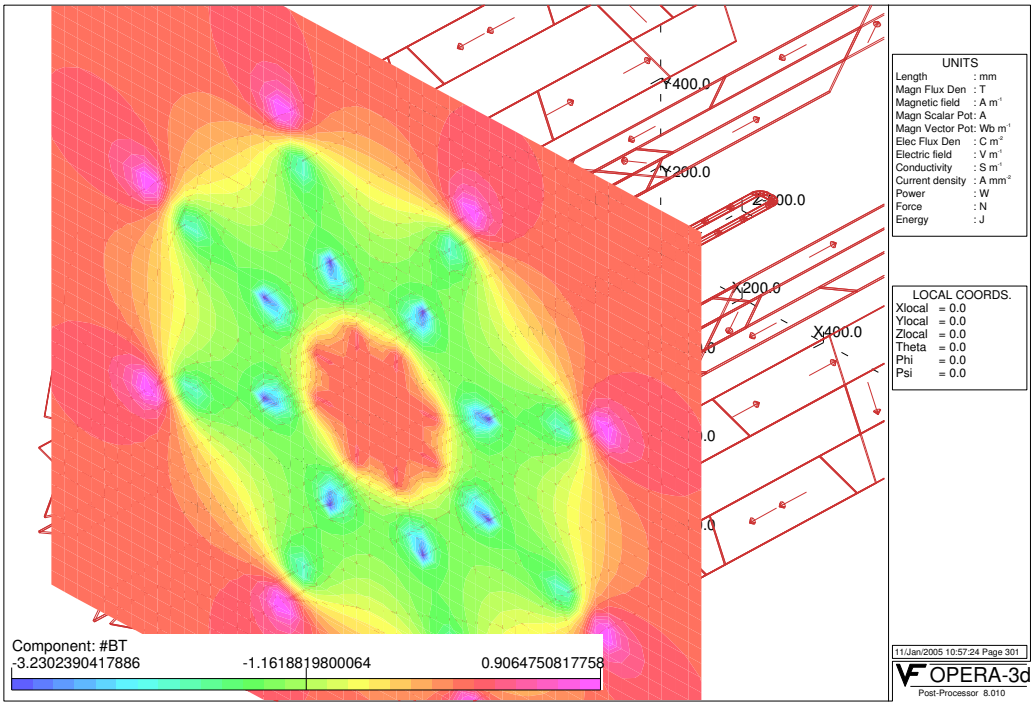

Figure 3.11: The magnetic field in the xy plane at the center of the accumulation cell (z=0).

parameter	value
R0	150 mm
RR1	150 mm
R	450 mm
Z0	-400 mm
ZZ1	1000 mm
Z	1800 mm
Cross Sec SC	100x3 mm^2
J_e SC	1450 $\frac{A}{mm^2}$
overall Cross Sec	300x15 mm^2

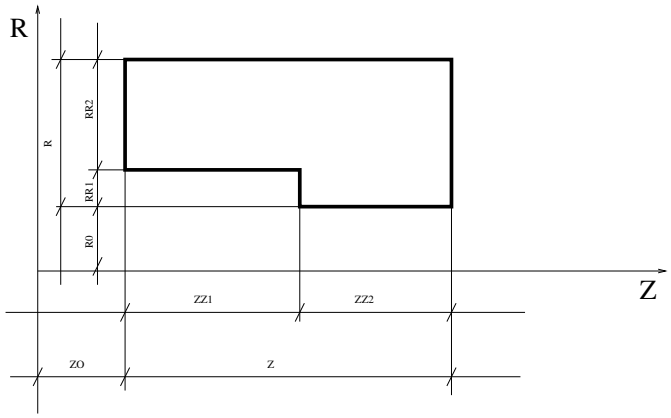

Figure 3.12: Coil parameters.

one more chamber (vacuum) wall if the magnet vacuum is independent from the beam one. Aluminum thin walls can be used to reduce particles multiple scattering. The second solution allow higher acceptance and increase flexibility in thermal insulation with respect to the first solution.

3.3.2 Acceptance

The minimum coils' distance from the beam axis (z) or, in general, the distance from the cell determines the acceptance. The accumulation cell center is at x=y=z=0 and 400 mm far from the upstream limit of the spectrometer magnet with respect to the incoming beam (Fig. 3.1). The acceptance for the toroid magnet for high zenithal angles ($\Theta \sim 90°$), as a function of the radial distance of the coils from the beam axis, is plotted in Fig. 3.13. The minimum distance from the z axis is $R0 + RR1 - 100 = 200$ mm (all radial dimensions), so that acceptance is about 80%. For different zenithal angles, the distance between the generation point and the coils increases thus increasing acceptance. The low zenithal angle track acceptance is influenced by the downstream part of the coils that in forward region are placed nearer to the beam axis. In this case the acceptance is limited by the distance between the target volume points and the upstream coils structure. The minimum distance along z axis between the end of the cell and the vertical part (RR1 long in Fig. 3.3) of the coil is $ZZ1 + Z0 - 100 - \frac{L_{cell}}{2} = 300$. In figure 3.14 is plotted the effective acceptance in forward direction. Considering for a safe calculation a point in the downstream end of a $L_{cell} = 400\ mm$ accumulation cell, the minimal acceptance is $\sim 70\%$ for a track at 20 ° respect to z axis. At larger angles the acceptance increases.

3.3.3 Quench protection

When a portion of the superconducting wire becomes normal conducting, normal conducting state propagates along all the magnet. This is called magnet's quenching. The superconducting material, when in normal conducting state, is more resistive than the wire's copper matrix, so the current during a quench flows in the matrix. The flowing of high currents in copper rises the coil temperature through Joule effect. The energy release can be destructive for the magnet. In particular, magnets can store sizable and dangerous amounts of energy that can easily destroy the coils. This is possible because the current densities in superconductors are usually much higher than in normal conductors. Hence the heat production is high in case of a quench and therefore the upper equilibrium temperature may mean that the cable insulation, solder joints or even the alloy melt.

The highest temperature, and hence the possible damage, depends on the deposited Joule heating (that is the Joule heating integrated in time $\int \rho J^2 dt$) and on the affected volume. The first transition point is the most dangerous point because it undergoes the current in a resistive state for a longer time, until the current is shut off and goes to zero, so that in that point is located the maximum temperature peak and the risk of permanent

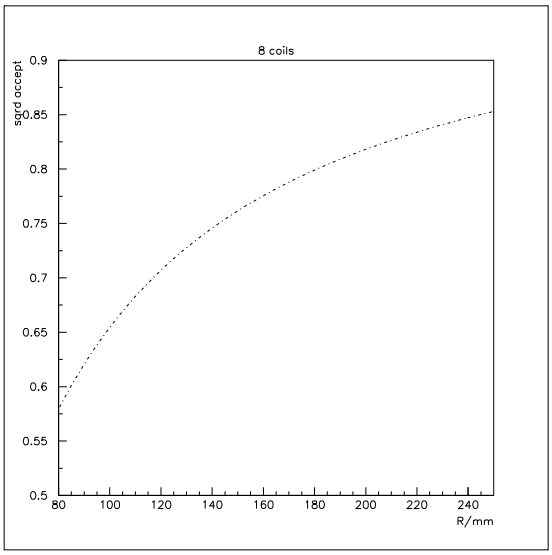

Figure 3.13: Squared geometrical acceptance in radial direction as a function of the distance from beam axis (R). The plot refers to particles' straight trajectories starting from the accumulation cell center.

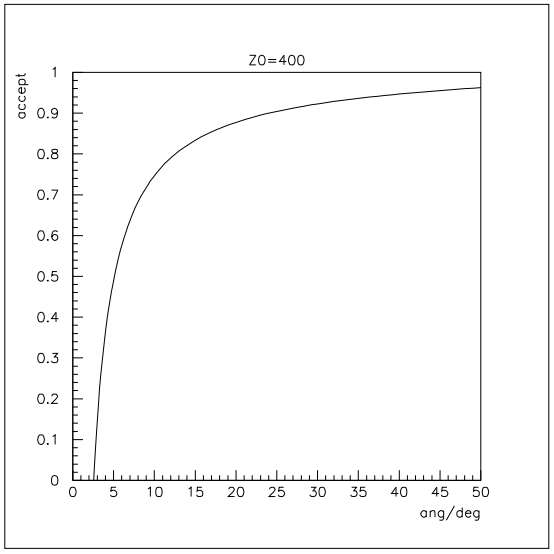

Figure 3.14: Squared geometrical acceptance for a straight track starting from the downstream accumulation cell end, as a function of the angle from the beam axis.

damage due to burning is higher.

Since the problem of quench propagation becomes very important for big high current density magnets, some heat charges (resistances) can be used to spread almost instantaneously the quench along the coils. If the energy is dissipated in a small region the risk is that region reaches too high temperatures and is permanently damaged. On the contrary heating the coil in several points by heating charges lets the energy to be dissipated in a larger volume reducing burning risks. Therefore it is necessary to detect quenches as early as possible to influence the energy deposition by some active means and to spread the deposited energy over a large volume.

3.3.4 Quench calculation

The quench propagation phenomena is rather complicated, but for magnet protection aims some simplifications can be useful: we can neglect the way in which the quench propagates and assume the system adiabaticity, i.e. without heat exchange with any other system. The adibaticity hypothesis is safe since neglects any cooling power, and is a fair approximation when a quench intrinsic time is less than a second, a common feature. When the wire begin to dissipate by Joule effect, the heat generated make the helium in contact with the coil's surface to boil off and to create a layer of gaseous helium

that has thermal transport properties much lower than the liquid. In this case an easy to apply and very safe assumption is the adiabaticy of the system, i. e. that there is non thermal exchange between the helium and the wire. With the adiabatic assumption the heat generated by Joule effect is not transferred to the helium and can only warm up the wire. The heat balance per unit of volume [41] can be expressed by:

$$J^2(t)\rho(T)dt = \gamma C(T)dT \tag{3.11}$$

where $J\left[\frac{A}{m^2}\right]$ is the current density, $T[K]$ the temperature, $\rho\left[\frac{\Omega}{m}\right]$ the resistivity, t the time, $\gamma\left[\frac{kg}{m^3}\right]$ the density and $C\left[\frac{J}{kg\ K}\right]$ the heat capacity. All the quantities are averaged over the winding cross section. Rearranging and integrating we have

$$\int_0^{\infty} J^2(t)\ dt = \int_{t_0}^{T_m} \frac{\gamma C(T)}{\rho(T)} dT = U(T_m) \tag{3.12}$$

The function $U(T_m)$ contains only the properties of materials used in the winding, so that the maximum temperature T_m can be evaluated numerically once the current density $J(t)$ is estimated.

$U(T_m)$ evaluation

In order to evaluate the function $U(T_m)$, we have to approximate the complicated behavior of the $\frac{C}{\rho}$ ratio as a function of the temperature and then average. Specific heat is a property that can be predicted fairly accurately by mathematical models through statistical mechanics and quantum theory for solids at ordinary pressures. For solids, such as Copper and Aluminum, the Debye model can be used. The expression for specific heat, neglecting the small difference between specific heat at constant volume (c_v) and pressure (c_p), can then be written as:

$$C = \frac{9RT^3}{\theta_D^3} \int_0^{\frac{\theta_D}{T}} \frac{x^4 e^x dx}{(e^x - 1)^2} \tag{3.13}$$

where R is the specific gas constant, T the temperature in Kelvin, θ_D the Debye temperature. The Debye temperature for Copper and Aluminum are [42] 310 K and 390 K respectively. The Copper and Aluminum specific heat is plotted in figure 3.15.

The average coil's $\gamma\ C$ function plotted in Figure 3.16 is a volume average (i.e. attained averaging the Copper and Aluminum function along the coil cross section weighting by the cross section area). It is now possible to numerically calculate the function $U(T_m)$ by using Equation 3.12. The result is plotted in Figure 3.17.

$J(t)$ estimation

The magnet current behavior in time depends on the discharge circuit features. A typical power supply and fast discharge circuit for a single magnet comprises the power supply, the

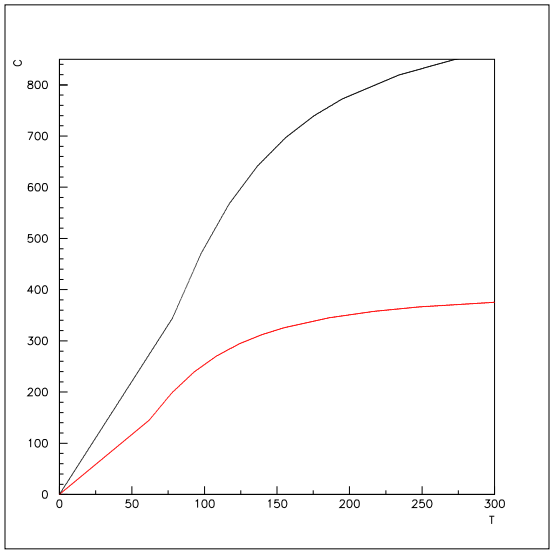

Figure 3.15: Calculated specific heat for Aluminum (lower red curve) and Copper (upper black curve) by Debye model.

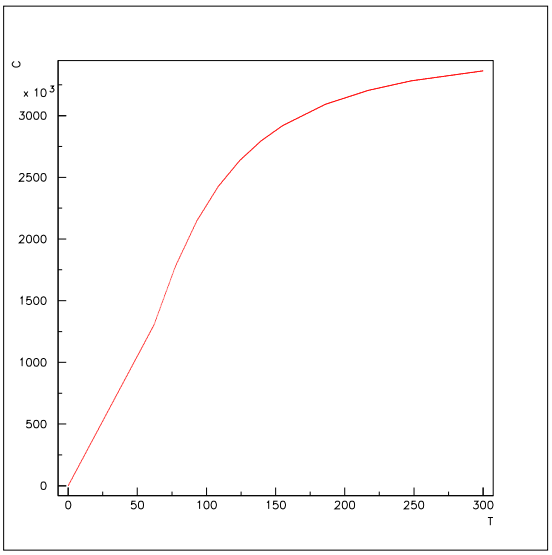

Figure 3.16: Coil's γ C function average by aluminum and copper volume.

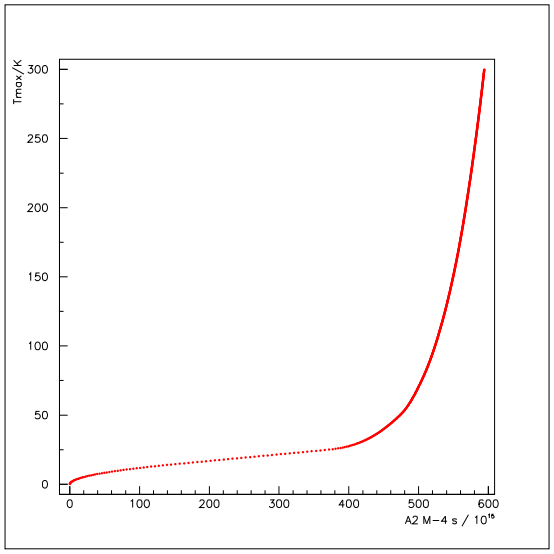

Figure 3.17: $U(Tm)$ function

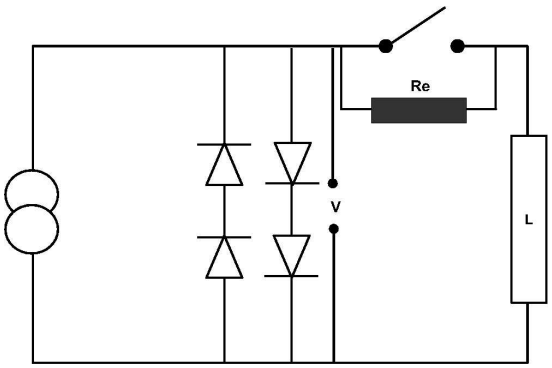

Figure 3.18: Power supply and protection circuit scheme.

magnet, protection diodes, a relay and a fast discharge resistance R_e. These components are sketched in Figure 3.18.

For the estimation of $J^2(t)$, the magnet is considered a perfect inductance since in case of quench all the resistances involved are small respect to the fast discharge resistance R_e (i.e. the cable, and the current lead resistances can be neglected) In normal magnet operation (ramping and full current) the relay S is in closed condition (short circuit) and the diodes are an open circuit since the voltage drop across them is not above their threshold (i.e. 0.6 V each diode). In case of quench the relay opens the circuit so that the magnet fast discharges its energy on the resistance and simultaneously the power supply is switched off and short circuited over protection diodes so that it doesn't supply any more the magnet.

The voltage the relay must undergo is $\Delta V_{ext} = R_e \cdot I_0$, where I_0 is the magnet nominal current value. Considering a round $\Phi = 0.85$ mm cable with a superconductor over Copper ratio equal to one and a current density into the superconductor of $J_c = 2900$ A/mm^2, the magnet nominal current is $I_0 \simeq 800$ A. A commercial 800 A relay can undergo at least $\Delta V_{ext} = 1$ kV and react in less 100 ms, so that the magnet can be short circuited on a $R_e = 1.25\ \Omega$ dump resistor. When the magnet quenches, its resistance increase immediately. The quench detection system, monitoring the voltage across each coil, can detect the quench in a negligible time and force the relay to open the protection circuit. The relay needs less than 100 ms, so the discharge begins after that time. After the relay opening, the current behavior is then exponential with a time constant $\tau_e = \frac{L}{R_e} = 0.06\ s$. The magnet inductance L plays and important role in the discharge, either in fast or slow one. It depends on the cross section of the superconducting cable used and it has been evaluated considering the toroid as a series of the eight coils.

To evaluate the maximum temperature reached inside the magnet we have now to estimate the total heat dissipated (see eq. 3.12) in the discharge. It has two contributions, the first one is due to the time required to the relay (S) to open: $U_1(T_m) = 0.1[\mathrm{s}] \cdot J_c^2 = 2.25\ 10^{17} \frac{\mathrm{A}^2}{\mathrm{m}^4}\mathrm{s}$. The second component is due to the discharge and is attained integrating the $J^2(t) = J_c^2\, e^{-2\,t/\tau_e}$ from zero to infinite. The contribution of the discharge is then $U_2(T_m) = \frac{1}{2} J_c^2 \tau_e = 0.61\ 10^{17}\ \frac{\mathrm{A}^2}{\mathrm{m}^4}\mathrm{s}$.

The maximum allowable temperature for the coils is 100 K. During a quench, a temperature peak below 100 K is considered a safe behavior for a magnet. The coils' maximum temperature corresponding to the $2.86\ 10^{17}\ \frac{\mathrm{A}^2}{\mathrm{m}^4}\mathrm{s}$ value of the $U(t_m)$ function is below 50 K. This calculation shows how the protection for such coils is feasible.

3.4 Conclusion

The PAX experiment was briefly presented. The choice of a toroidal magnet for PAX spectrometer was motivated. The use of superconducting coils, surrounded by a winding of Aluminum for support and cooling, allows to reach an azimuthal detector acceptance in excess of 80%, while the radius of the inner tracking volume can be kept below 75 cm.

These characteristics meet the requirements of the PAX detector project. The conceptual design completed with magnetic design, materials and quench protection discussion were reported in this section.

Chapter 4

HERMES Recoil Detector superconducting magnet

The HERMES Recoil Detector (HRD) superconducting solenoid and its cryogenic system commissioning is presented. Detail on cryostat modifications and interlock design are explained in this section. I have been co-responsible of the HERMES Recoil Detector commissioning during 2005 and since January 2006 I am responsible for the running of the magnet.

4.1 General detector design

The HERMES Recoil Detector consist of three active detector parts: a silicon detector around the target cell inside the beam vacuum, a scintillating fiber (SciFi) tracker in a longitudinal magnetic field and a photon detector consisting of several layer of scintillator strips inside and outside the solenoidal magnet. The thickness of the target cell wall (50 μm) and of the beam pipe (1.2 mm) is kept to a minimum to achieve the lowest possible momentum thresholds for the silicon and the SciFi detector. The cross section of the Recoil detector is shown in Figure 4.1. The silicon detector consist of four modules organized in a 'diamond shape' around the target cell, each module consist of two layers of double-sided silicon. The silicon detector uses the energy deposition of the recoil protons to determine their momentum. The silicon detector can detect recoil protons down to very low momentum (130-135 MeV/c) corresponding to kinetic energies of 9.7 and 5.5 MeV respectively because it is located inside the ultra high vacuum of the HERA accelerator.

The scintillating fiber detector consist of two barrels with 8 layers consisting of 0.5 mm thick fibers, the first four parallel to the z axis (the beam) and the second four under a small stereo angle (about 10°). The SciFi detector uses the deflection of charged particles in the longitudinal magnetic field of the Recoil Detector for the measurement of their momentum. The energy deposition in the fibers provides a means of particles identification to separate protons and pions at momenta between 250 and 450 MeV/c.

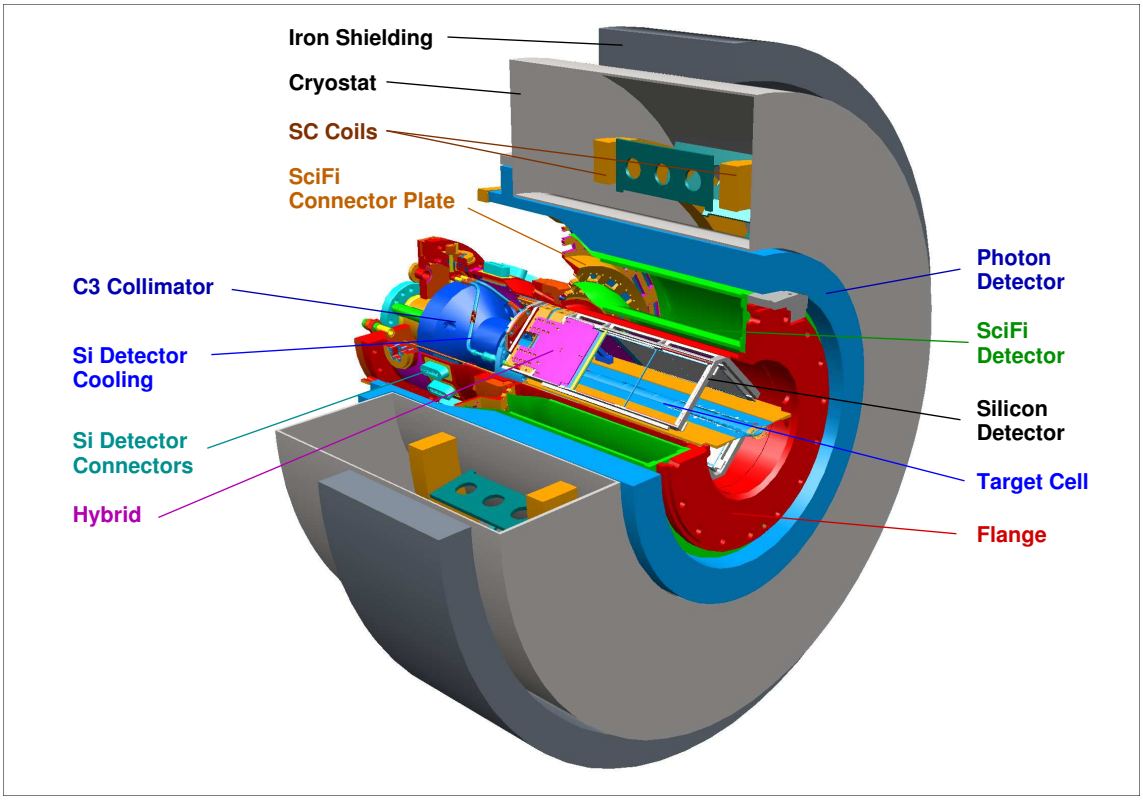

Figure 4.1: Three dimensional cut through of the Recoil detector CAD model.

The photon detector consist of four layers of scintillator strips that are organized in barrels of 72 strips each on the inside and outside of the solenoid. The innermost layer uses a thin layer (1 radiation length) of lead as shower material. The other three layers use the cryostat/coil material and the iron return yoke of the magnet for the same purpose. The photon detector has a multiple role: photons from π^0-decays can be detected, because they produce clusters in the detector which have no corresponding tracks pointing at them. In addition it improves the pion/proton separation for momenta between 400 and 800 MeV/c.

The magnet fulfills a double function for the Recoil Detector: it removes the *Møller* electrons by letting them spiral forward and in this way protects the silicon detector from background, and it provides the magnetic field for the SciFi tracking detector. The natural configuration for such purposes is a solenoid since the field parallel to the accelerated beam is optimal for both the purposes. The boundary conditions for the magnet design are given by the requirements of SciFi and silicon detector, the spacial constrictions imposed by the experimental surroundings and the other HERMES detectors. The magnetic field having a strength of about 1 Tesla allows the momentum resolution of the SciFi detector

to connect smoothly to the silicon detector one. For the same reason the homogeneity of the field should also be better than 20% in either direction. The reduction of *Møller* electrons is adequate for fields above 0.7 Tesla. Spacial constrains due to others detectors led to the decision to use a superconducting solenoid since this is the less bulky solution. It also allows the installation of the outer layers of the photon detector, which for a normal conducting magnet would have been questionable. A further condition is imposed by the wire chambers i the front region of the experiment and by the photomultiplier that is needed for the photon and the SciFi detectors. They requires the magnetic field to drop to less than 5.0 mT at 1 m distance from the magnet, this can be accomplished thank to the ferromagnetic shield of about 5 cm thickness around the magnet.

4.2 The HRD magnet

The HRD longitudinal magnet is a superconducting solenoid made up of two coils whose inner radius is 600 mm, the magnet and its cryostat have been commissioned by HERMES collaboration to Efremov Institute, Saint-Petersburg and have been built in S. Petersburg. The two identical coils have a 25×60 mm^2 cross section and are placed at a 198 mm distance each other (see Fig. 4.2). Each coil has 26.5×68 NbTi wires having a diameter equal to 0.85 mm provided by Efremov institute; the cross section encased in a 2 mm copper case (see Fig. 4.2. The coils are designed to work partially inside the liquid helium bath and partially by conduction thanks to the copper case. At the rated current of 166 A the solenoid provides a 1 T field with a 20% field homogenity inside the operating region: a 250 mm radius cylinder 300 mm long centered in the accumulation cell center; the measured field is plotted in Figure 4.3. The inductance of the coils is $\sim$ 10 H and the stored energy is 144.5 kJ.

4.2.1 The cryostat

The cryostat is a cylindrical helium cryostat with a 500 mm warm inner bore. The inner helium chamber in which are placed the two superconducting solenoidal coils contains around 27 l of liquid helium. The inner vessel is insulated by a vacuum vessel and gaseous helium cooled thermal shields.
The vacuum is permanently pumped from an external pumping system. A part of the gaseous helium evaporating from the liquid bath flow into a piping system connected to the two thermal shields keeping them cold. The flowing sequence is from the colder part to the warmer part of the shields as shown in Fig. 4.4.

The cryostat has four total gas outputs: the thermal shields output, two lines cooling the current leads and a bypass (a direct output).
The current leads are two 6 mm diameter 1 mm wall thickness copper pipes. The bypass

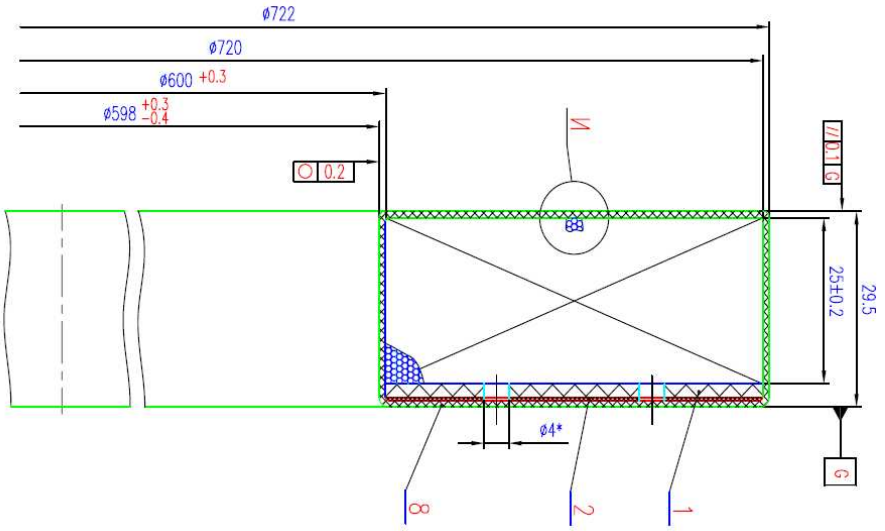

Figure 4.2: Detailed dimensions of the superconducting coils of the HRD magnet.

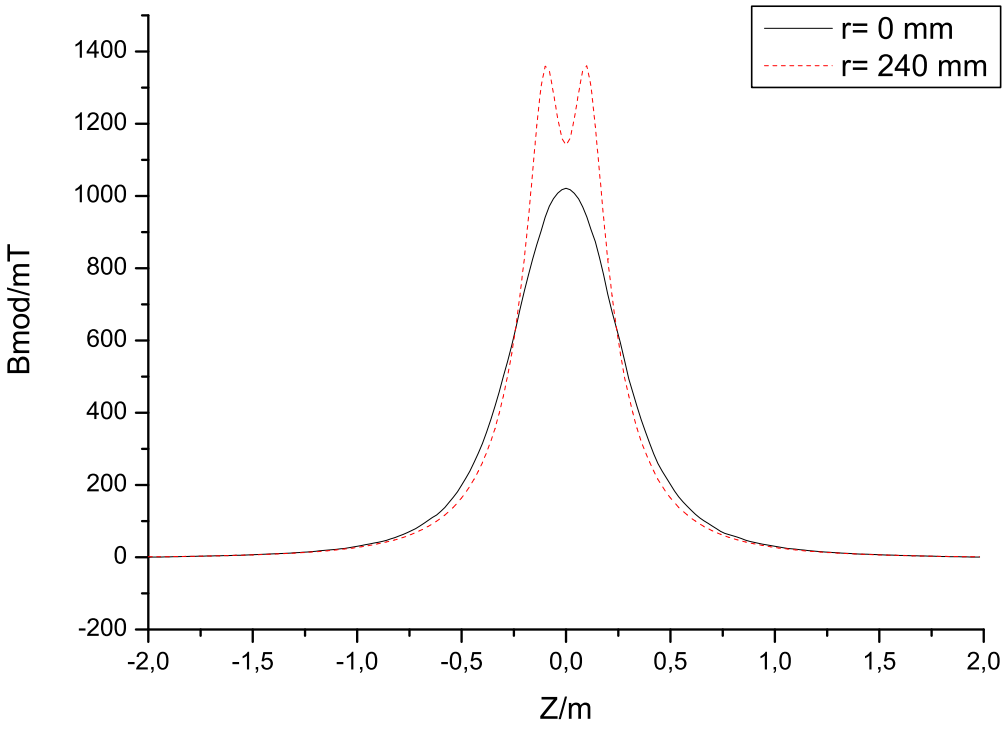

Figure 4.3: Measured magnetic field at maximum current along z direction. The field is plotted in the center of the magnet (r=0 mm) and at a 240 mm radius

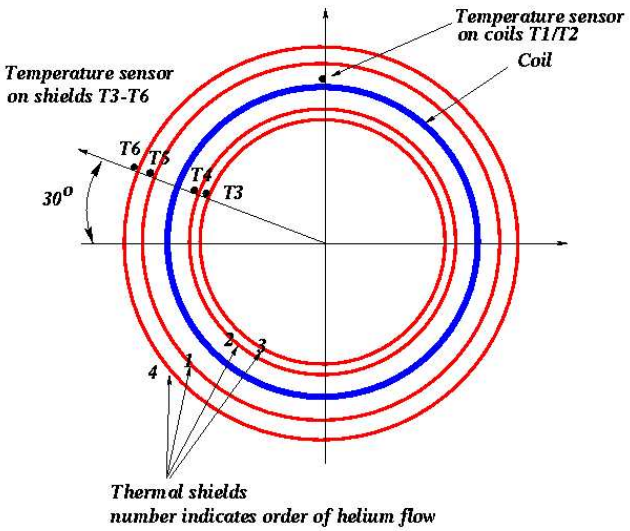

Figure 4.4: The picture shows the location of the temperature sensors placed inside the cryostat: T1 and T2 measures the temperature of the magnet coils , T3 to T6 the thermal shields temperatures. The gaseous helium evaporating from the inner vessel flows first into the inner shields and then in the outers as shown.

is a 14 mm diameter pipe connected to the inner vessel by a relief valve.

The helium inlet pipe splits into five arms with holes to let helium enter the vessel. Four of them are around the coils to reduce temperature gradient during cool down. The helium level is measured by a superconducting liquid helium level probe inside the vessel, the probe is placed on one half of a circumference. Figure 4.5 shows the relation between the probe output (dm) and the effective helium inside the vessel.

4.3 Cryostat tests and modifications

Several tests in the test area have been performed to test the cryostat and find operating parameters. The magnet installed in the test area is shown in pictures 4.6 and 4.7.

The cool down procedure has been set using the thermal shield flux to cool down the system. A typical coil temperatures during the cool down is shown in Figure 4.8, where also the cooling speed (rate) is plotted. In Figure 4.9 the thermal shield temperatures and cool down rates are plotted, the step is due to the exchange between measured probes. The maximum allowed cooling speed for the magnet and the thermal shield is -40 K/h in

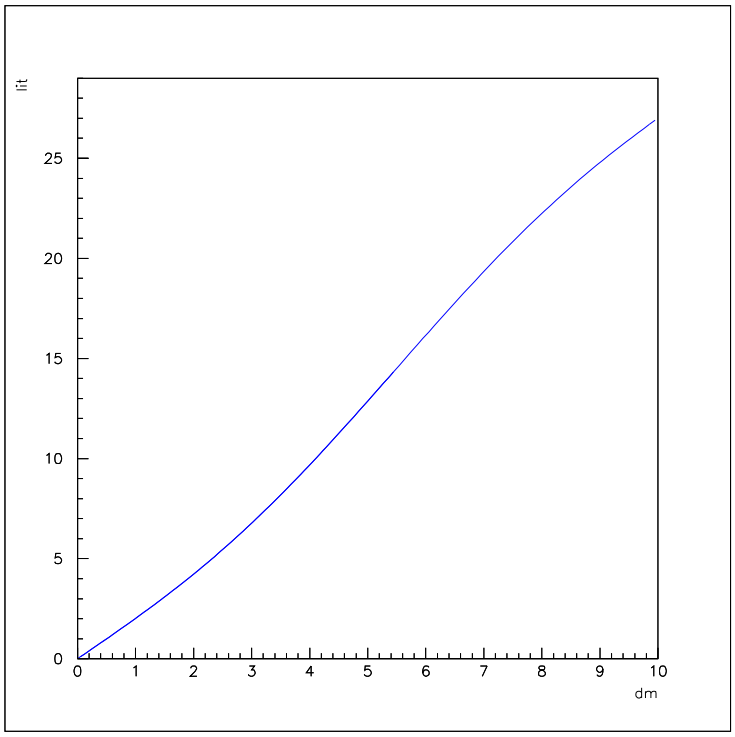

Figure 4.5: The liters of liquid helium inside the cryostat are plotted with respect to the length measured by the liquid helium level probe.

the range 300 K-100 K; the cooling rate is limited by the difference in thermal expansion coefficients of the material by which is built the magnet.

4.3.1 Static helium consumption and modification of the cryostat

The magnet had thermal instabilities due to transfer line insulating vacuum problems (that were solved by continuous pumping) and limited bypass flux. During the test the bypass line has been opened in air with a complete helium loss because the pumping speed of the available pumps was too low and a high flux flow meter has been used to read the helium flux. The maximum flux is roughly 1.2 g/s because the transfer line have to be kept cold to allow a continuous cryostat filling to grant duty time above 4 hours. In these conditions an optimization of the flux has been performed and the average helium consumption of the system is 22 l/h of liquid helium. These high helium consumption have been accepted since the detector run is limited to 1,5 years.

The total thermal load in static condition and full current is below 3 W. The steady state helium consumption at zero current measured before the delivery is less than 4 W.

Figure 4.6: Cryostat in the test area, from left to right are visible the transfer line column, the bypass one and the thermal shield-current leads one. The service flanges are also visible with the connections for the temperature probes and the helium level probe. In the bottom left part of the cryostat the vacuum connection is placed.

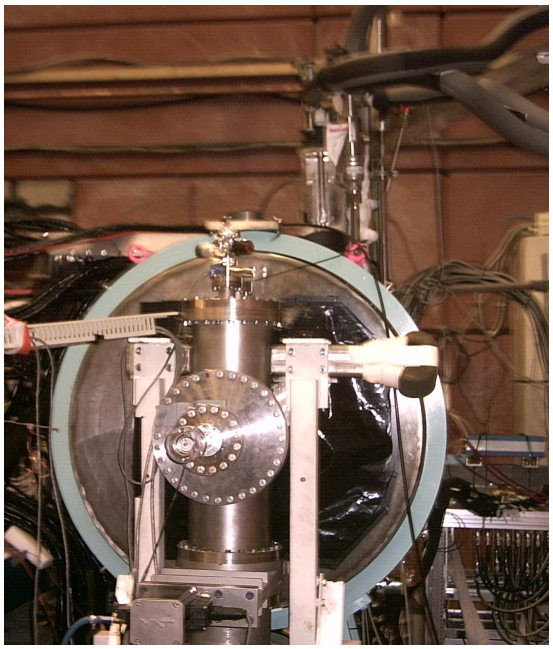

Figure 4.7: Cryostat in the test area with the scattering chamber and all the recoil detectors installed

The steady state helium consumption at 166 A, measured at DESY, has been 3.7 W. In this case the transfer line and the bypass were closed, while the thermal shield and current leads average flows were 16.7 l/min and 25.7 l/min respectively.

Several mechanical problems were found during last year of commissioning:

- high helium consumption due to continuous refilling mode,
- The bypass line icing and cryogenic fluid liquefaction on surface,
- the current leads icing and cryogenic fluid liquefaction on surface.

The magnet has to operate for the whole length of a HERA beam lifetime i.e. more than 10 hours. It has to be operated always partially inside the helium bath thanks to

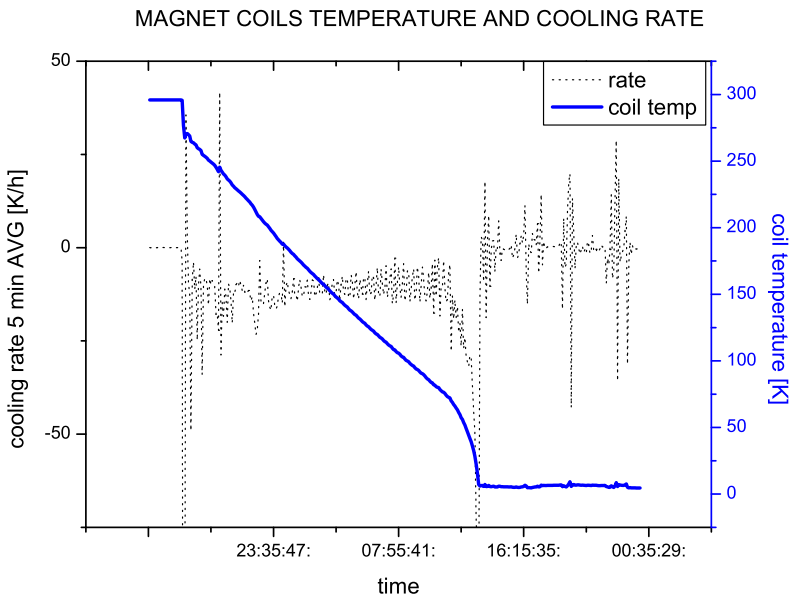

Figure 4.8: Magnet temperature and cooling rate during cool down.

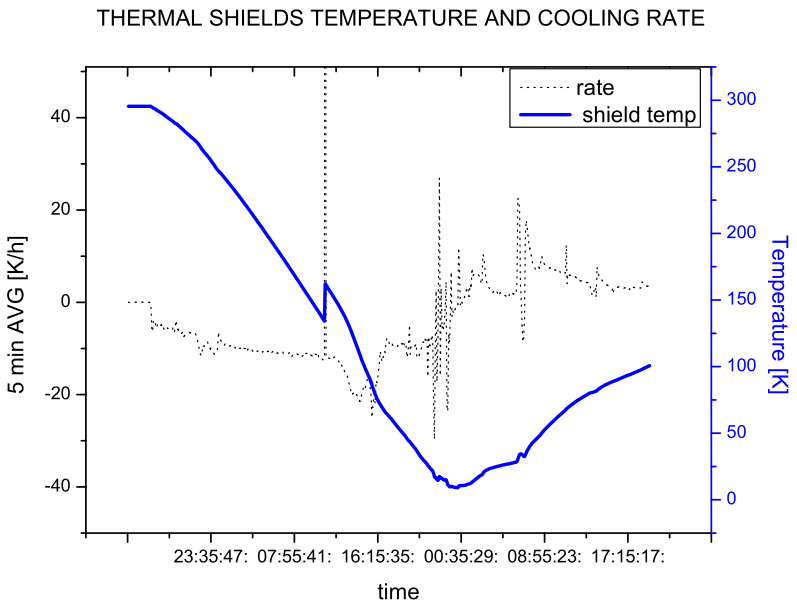

Figure 4.9: Thermal shields temperature and cooling rate during cool down.

a Copper cover cylinder that cools down by conduction the superconducting wire outside the bath. When the helium bath is in the range 35-85 dm the magnet can be safely supplied by maximum current, so that the maximum duty time is $\approx$ 4 hours neglecting the time required to ramp up and down the magnet. A standard helium refill is not possible because the transfer line warmed up inject (relatively) warm helium gas at the beginning of the refill. That helium warms up the part of the magnet outside the helium bath, warming it above 10 k causing a quench. The use of a phase separator has been rejected because the operation required a major modification of the cryostat and the time to modify and safely test the apparatus has always been too long with respect to the time remaining for the test and installation. A transfer line with a needle valve has been acquired. The transfer line will be used for test in order to try to batch fill the cryostat, in the meanwhile the transfer line is kept always open, increasing the helium consumption. The candidate optimized by several test the helium flows reducing the helium consumption with the transfer line opened by a factor 3.

The bypass line exiting the cryostat had problems due to ice formation as can be seen in Figure 4.10, the upper part of the bypass column was not vacuum insulated because of problems during the welding of the insulation itself, in fact it was different with respect to the design. The ice formation was near the HRD detector, so that the water could damage the detectors when defrosting. Moreover the very low temperature could liquefy nitrogen or even oxygen, so the modification has also been a safety issue. The candidate commissioned and designed the modification of the vacuum insulation of the bypass line; a cryogenic connection has been included, so that a 1 m long transfer line is inserted in order to keep far from the cryostat the ice formation. The modified line can be seen in Figure 4.11.

A Plexiglas cylinder (Fig. 4.12) has been used to avoid ice formation and cryogenic liquid formation on the current leads and the thermal shield lines. Main issue for this modification is the safety, because by the current leads the current is supplied to the magnet, but also water damaging detectors when the ice layer defrosts has been an issue. In fact the nitrogen flux has been calibrated to avoid ice formation outside the Plexiglas cylinder. Inside the Plexiglas cylinder $\approx$50 l/min of room temperature nitrogen flows keeping dry the current leads and also the outer Plexiglas surface. Avoiding any possible source of water on the detector inside the cryostat warm hole has been a design request. As can be seen in Figure 4.12 the lines exiting the Plexiglas are connected to vacuum insulated pipes. Part of the work of the candidate has been the commissioning of the Plexiglas cylinder and the optimization of the working parameters such as dimensions, choice of the gas, temperature and flux.

4.4 The cryogenic system

The cryogenics systems that will be used to run the HERMES Recoil Detector magnet are sketched in fig 4.13.

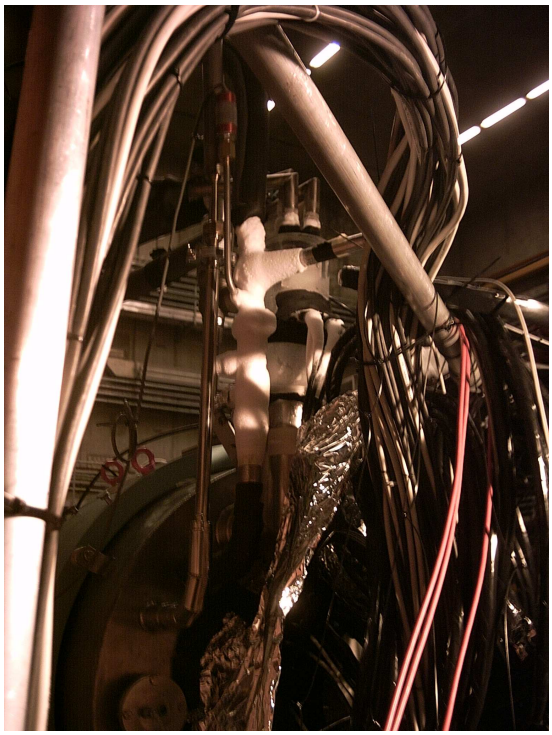

Figure 4.10: Cryostat during a cool down before the bypass line modification. The line is completely covered by ice. The Plexiglas cylinder is also covered by ice in this picture.

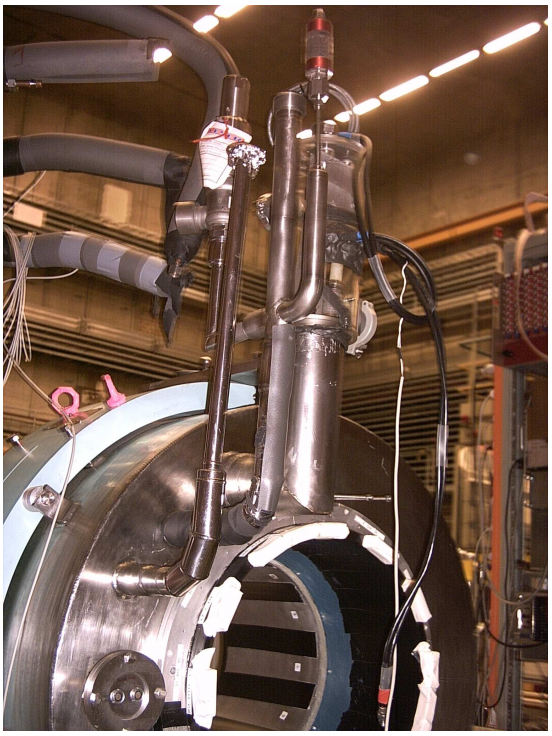

Figure 4.11: Cryostat after the bypass modification. The insulation vacuum has been extended to that line.

The cryostat has 6 temperature sensors (RhFe), 1 on each SC coil and 4 on the thermal shields, 1 L-He level probes (plus 1 spare) and a pressure gage for the insulating vacuum and the He boil. The transfer line from the HERMES Dewar has a a pressurized air controlled solenoidal valve. From the cryostat there are 4 G-He output: the thermal shields cooling, 2 current lead coolings and the bypass.
The thermal insulating vacuum is continuously pumped down by a simple rotary-turbo pumps system. The system has its own interlock providing a pumping system hardware (HW) OK.
The magnet protection system is an independent hardware circuit that reads the voltage between the two current leads and when detects a quench, turns off the magnet current supply. This system provides an OK (ready) HW signal and is triggered by an outer HW signal to fast ramp down the magnet current.
The power supply system is controlled by a software program (ramping up and down) and it is shut off by the quench detection system.
The magnet is protected also by an emergency button (NOT AUS), that shuts off the

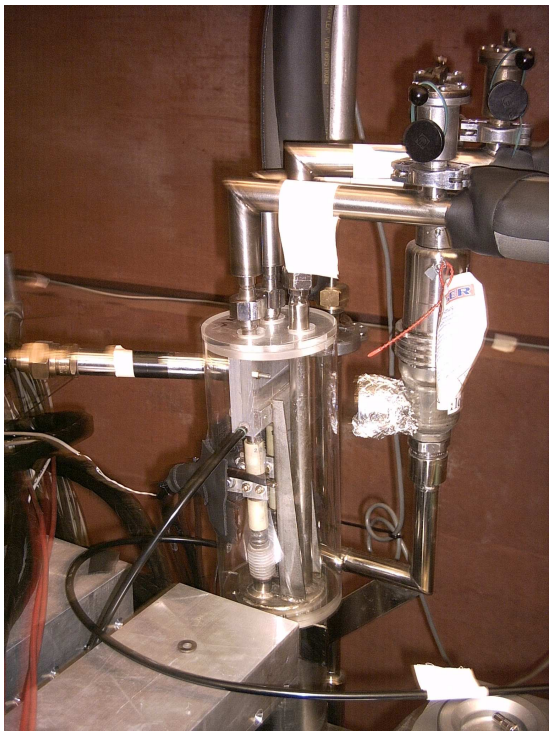

Figure 4.12: Detail of the column with the current leads and the thermal shield cooling. When the magnet inside the cryostat is cold warm nitrogen flows inside the Plexiglas to avoid ice formation.

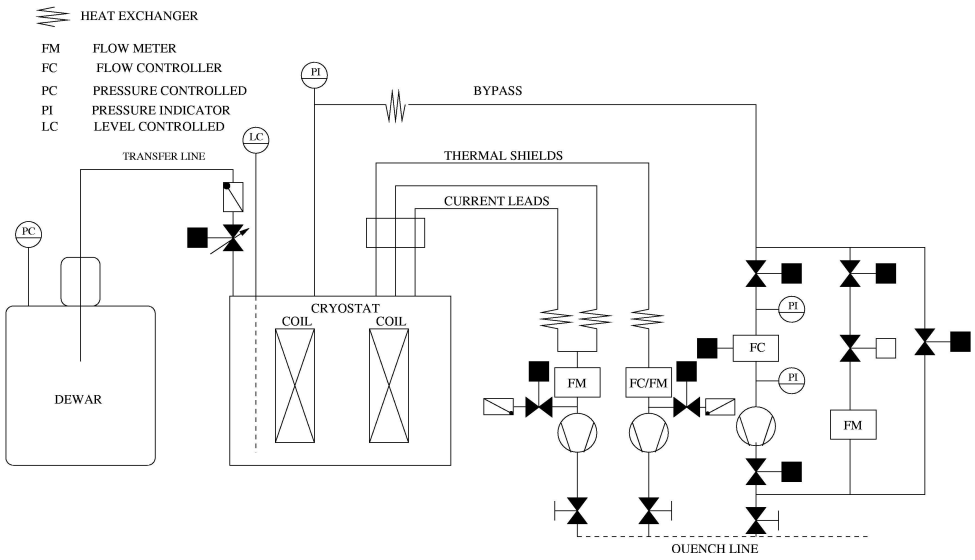

Figure 4.13: A simplified scheme of the helium input and outputs.

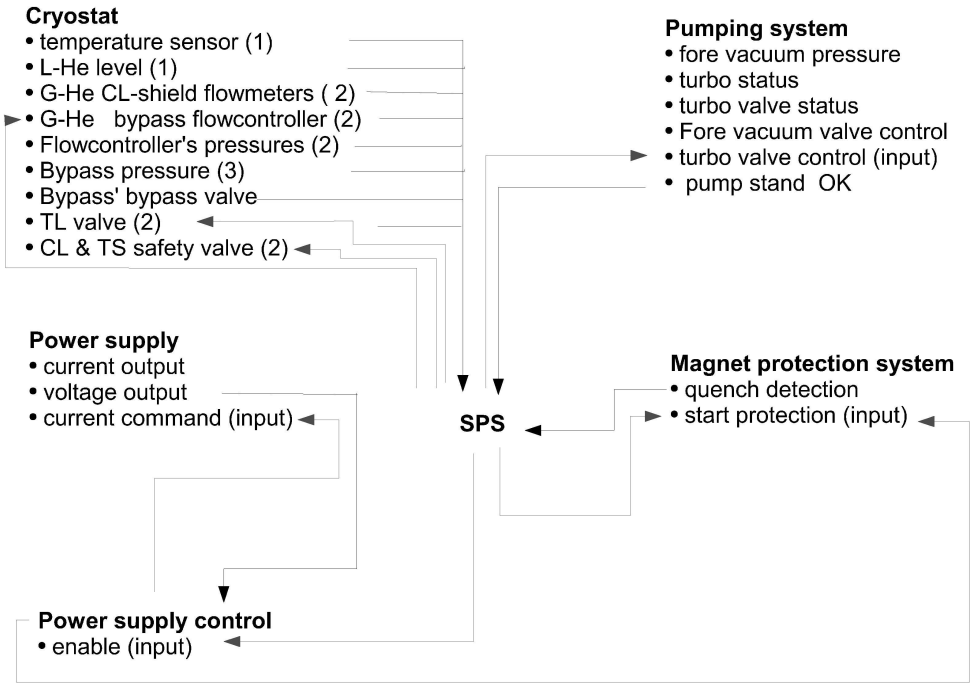

Figure 4.14: Simple interlock scheme

system and starts a fast magnet ramp down.
All the systems involved in the Siemens PLC controller (SPS) measuring and controlling are resumed in Figure 4.14 and Table 4.1.

4.4.1 Logic

Main purpose of the interlock is to enable the current supply to the magnet and to properly react in emergency cases.
The SPS produces a series of hardware enable signals, a normally open relay contact. If the pumping system is working, the insulation vacuum is good, the cryostat status is good and the magnet protection system is enabled, then the magnet current supply is enabled.

Enable HardWare signals

The Pumping system HW OK signal is given if:

- fore vacuum pressure below **threshold**

- turbo at regime **relay**
- high vacuum valve operating **relay**
- high vacuum below **threshold**=5 $10^{-5} mbar$

The Cryostat HW OK signal is given if all the following conditions are fulfilled:

- the coils temperature is below a **threshold** $\simeq$ **8 K**
- the insulation HW OK signal **relay**
- the L-He level is above a **threshold=25-30%**
- the current leads (CL) flux is good $\phi_{TL} = 15\ l/min$
- the thermal shields (TS) flux is good $\phi_{TS} = 40\ l/min$
- the bypass flux is good i.e. input is compatible with output

The pumping system HardWare OK is given if all the conditions are fulfilled allows the system itself to open (and keep open) the high vacuum valve.

4.4.2 operation

The system can operate in different working conditions. In standard operation must be guaranteed safe cool down, normal operation (magnet on/off and helium refilling) and warm up. The interlock system must also react in case of emergencies, such as a quench, NOT AUS button pressed or power failure.

cool down

The cool down process requires roughly one day (24 h). Both the magnet and the thermal shields must be cooled down at rates below 40 K/h in order to prevent any damage due to different thermal expansion coefficient in material used for the construction. The slow cool down is performed partially opening the thermal shield and current leads outputs (see Fig. 4.13)
The parameters to control are the cryostat pressure, one coil temperature, two thermal shields temperatures, thermal shield flow and current leads flow.
The dewar pressure is monitored and if out of range, an error signal is sent. The dewar pressure is automatically controlled and the set point is set by the DESY cryogenic group.

signal to/from SPS	in	out	name
cryostat			
magnet temperature	0-10 V		mt1
thermal shield temperature	0-10 V		ts1
liquid helium level	0-10 V		hl
CL flow meter(flow meter)	4-20 mA	4-20 mA	clfm
TS flow meter	4-20 mA		tsfm
BP cryostat pressure	4-20 mA		bpcp
BP flow controller (2x)	2x 4-20 mA	2x 4-20 mA	bpfc
BP flow controller pressures (2)	2x 4-20 mA		bpfcp1 bpfcp2
BP flow meter			bpfm
BP flow meter valve			bpfmv
BP full open valve			bpfov
Transfer Line valve	0-10 V	0-10 V	tlv
TL solenoidal valve	0-10 V	0-10 V	tlsv
TL regulating valve	0-10 V	0-10 V	tlv
CL safety valve	0-10 V	0-10 V	clsv
TS safety valve	0-10 V	0-10 V	tssv
hardware OK		relay	hwok
Power Supply control			
PS enable		relay	pse
PS hardware OK	relay		pshw
magnet protection			
MP quench detection		relay	mpqd
MP start protection		relay	mpsp
pumping system			
enable pump system		relay	pse
pump stand hardware OK	relay		pshw

Table 4.1: SPS inputs and outputs.

The 3 temperatures monitored are needed to check the cooling speeds, they can be calculate averaging over 3-5 minutes.
The cryostat pressure can be kept inside the 19.5 - 25 % range. 1 bar correspond to 18.7-18.8 %.

If the vacuum HW is OK, the magnet pressure is 1-1.3 bar and the cooling rate is above -40 K/h, the cool down continues and the TL valve is opened and kept open. The magnet pressure and the cooling rate are controlled by the He flow in the TS line.

running and helium refill

During the normal running mode the magnet can be off, ramping up or (slow) down or at full current (166 A). The difference of the three states is only in the current and voltage control on the magnet. The SPS must monitor the parameters listed in table 4.1, and if those values go over range, turn off the magnet, starting the fast ramp down. To start the fast ramp down of the magnet, the quench protection system must be triggered. For example a normally open relay controlled by the SPS can be installed in series with the NOT AUS button.
The magnet temperature is the most important parameter to be monitored. When any current if supplied to the magnet, a temperature increase can make the magnet to quench. The magnet can run at nominal current (166 A) at temperature below 6 K (experimentally tested).
The magnet temperature depends also on the cryostat pressure, that can be regulated by the gaseous helium outputs.
The current leads flux must not be below 20 l/min to avoid physical damages (internal burn). The current leads cooling must be guaranteed also in case of pump failure, opening the bypass valve (normally open) in air. Each current lead line has its own bypass valve (fig 4.13).
The thermal shields temperature can be between 20 and 100 K. Also the thermal shields have a bypass valve in air, opened in case of any failure.

If the vacuum HW is OK, the coil temperature is below 8 K, the TS flow is above 20 l/min, the CL flow is above 10 l/min, and the liquid helium level is above 30% then the maget power supply is enabled.

The interlock has been developed for the use of a needle valve in the TL, in case of the use solenoidal valve, the logic is more simple and require minor changes. In the normal running mode the magnet pressure is kept at 1.1 bar by a PID loop. The PID parameters can be modified by an expert. The magnet runs in normal mode until the liquid helium level is above 50%.

The refill mode is enabled when the liquid helium level in the cryostat is below 50%. The TL valve is opened by 5% (absolute), then the system wait 10 minutes before acting on the TL. This is needed not to quench the magnet during refill. When the liquid helium level is above 80%, the mode is again normal.

The bypass line

The bypass line (Fig. 4.13) has two different running modes to regulate the fluxes. The main mode uses the flow controller and the pump; in that condition the flux can be fully regulated by the flow controller. In case of any increase of pressure or temperature inside the cryostat, the third line (from left) is opened by a remote (SPS) controlled valve in order to force the pressure to reduce to ambient value.
The second line is composed by a manually regulated valve and a flow meter. They can be used in case of failure or maintenance stop of the main line. The third line is working also in this case as a fast way to reduce the cryostat pressure.
There are four manual closing valves: two to insulate the flow controller line and the others to close both flow meter and full open valve lines.

warm up

The warm up procedure requires several days.
The magnet is at zero current, the power supply is turned off, the transfer line is closed before the warm up.
During the warm up procedure the bypass is fully open, while the CL and TS are closed. Experimentally the magnet and the thermal shields warm up safely in these conditions. There are no pumps turned on so that the cryostat pressure cannot reach a pressure below one atmosphere.
During the warm up the SPS monitors the cryostat pressure and the warming speed and controls the bypass gaseous helium flux by the BP flow meter.

emergency

In case of an emergency (power off or NOT AUS button pressed), the system must react and take the magnet and the cryostat to a safe condition.
The actions that must be guaranteed also in case of partial or total power failure are: turning off the power supply (as if in case of quench), closing transfer line, opening the bypass line, opening the current leads and let the G-He flux to flow freely, closing the insulation vacuum valve.
These operation can be guaranteed simply using normally open relays or normally close/open

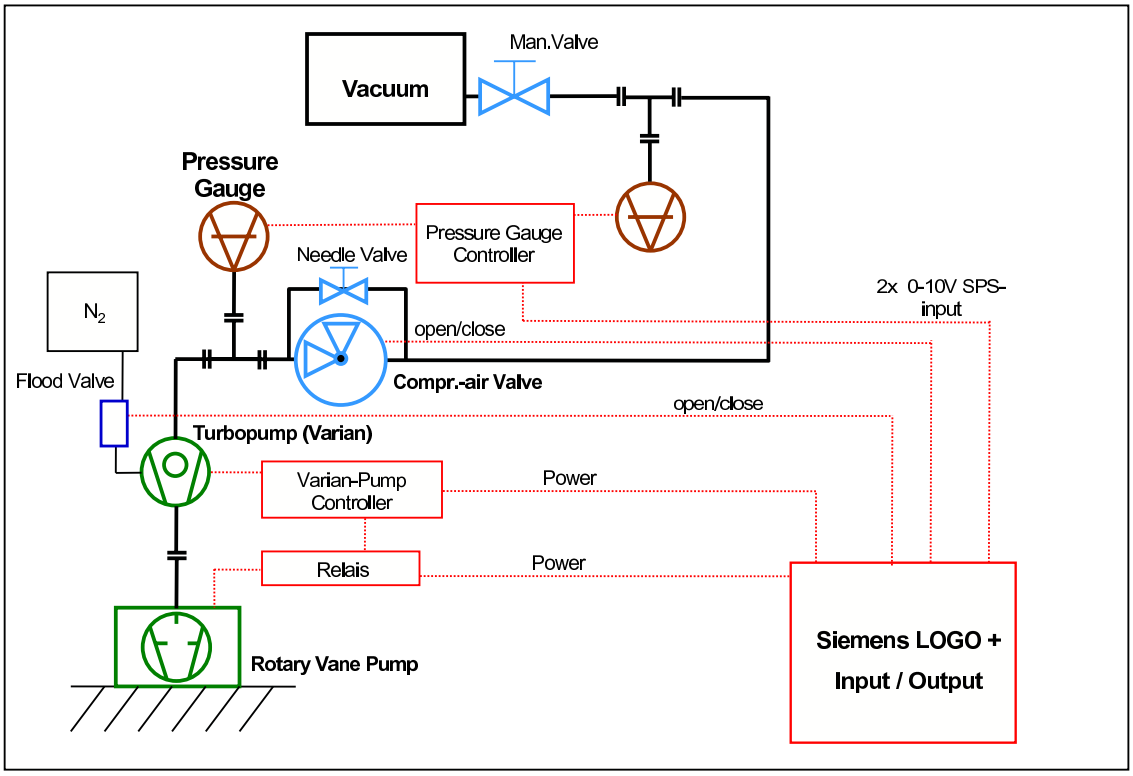

Figure 4.15: Cryostat vacuum insulation pumping system.

valves: the HardWare protection relays are normally open, while the transfer line valve relay are normally close.
The flow controller is normally normally closed, so that a normally open bypass valve is needed.
The flow into the thermal shields and both the power supply lines must be guaranteed also in case of pumps tripping, each line is provided with a normally open valve to air.

4.4.3 Insulation vacuum

The insulation vacuum has its own interlock (Siemens LOGO PLC) interacting with the main interlock (see Fig. 4.14).
The system is sketched in Fig. 4.4.3. The LOGO controls the open close valve, the pumps and the flood valve. The output from LOGO is one relay (hardware pump stand OK) and the cryostat vacuum (4-20 mA).

The cryostat vacuum must be kept below 1 10^{-5} mbar. If the vacuum is $\approx 10^{-4}$ mbar at room temperature, the pressure when the liquid helium is inside the cryostat is $\approx 10^{-6}$ mbar.

4.5 The quench protection circuit

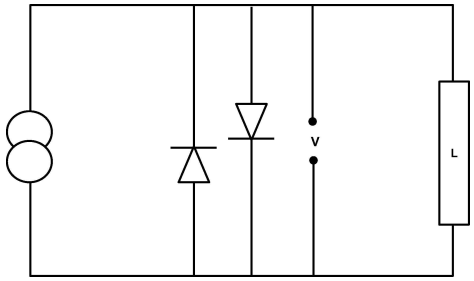

Figure 4.16: The quench protection and discharge circuit. Each diode plotted represent a series of 4 diodes. The maximum voltage before short circuit is now 2.4 V.

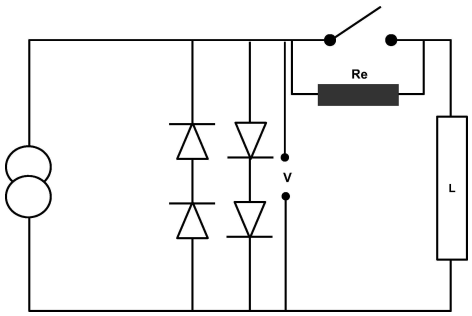

Figure 4.17: A possible modification of the quench circuit with an external resistance for faster discharge.

The electrical circuit power supplying and quench protecting the magnet as it was delivered is shown in Figure 4.16. The quench protection circuit is an hardware protection, when the voltage across the diode is above the 1.2 V threshold, the diodes behave like a short circuit making the magnet to discharge on the diodes and the power supply is shut off and it is short circuited on its protection diodes. This circuit provide a safe discharge (in case the magnet is not quench) in about 30 min.
The ramp up or down time with this circuit is 1 h, due to the maximum voltage diode can undergo before closing the circuit.
During the test made before delivery, the circuit used an external resistance. An external resistance allow a faster discharge and partial energy dissipation in air instead of inside the cryostat.
The circuit can be modified in order to reduce the ramping and fast discharge times.
To reduce ramping time, can be added two more diodes like in Figure 4.17, doubling the voltage (1.2 V) without a short circuit and halving the rumping time (1/2 h).

To reduce magnet's fast ramp down can be used an external resistor (R_e) and a relay (see Fig. 4.17). The fast ramp down speed with no external resistor is dominated by the magnet's inductance.

The latter solution allows faster magnet operations, but involves a more complicated hardware. Also the interlock becomes a little more complicated.
As an example, using a resistor $R_e = 1.5\ \Omega$ the fast ramping time is less than 30 sec. The candidate commissioned the final circuit that has 8 diodes (4 per each line), with a final maximum allowed voltage before short circuit of 2.4 V. The protection circuit trigger has been set to 3 V.

4.6 Conclusion

The commissioning of the HRD superconducting solenoid has been presented together with my contributions that are the revision of the magnet cryostat, the determination of the working parameters and the design of the final interlock system.

Appendix A

Polarized Antiproton eXperiments

The study of polarized reactions provides access to the elusive spin structure of the nucleon and to the investigation of the spin role in strong interactions. High precision experiments with polarized lepton beams scattering from polarized nucleon targets have provided valuable informations but not yet conclusive. New approaches are being proposed, where the use of polarized nucleon beams, and in particular antiproton beams, provide access to the missing pieces of the complete understanding. The technological challenges connected to these innovative approaches have in the past prevented the realization of dedicated experiments. The studies presented in this thesis have the goal to address some of these challenges.

A.1 The Spin physics today

In recent years, a detailed investigation of the spin structure of the nucleon and the determination of its partonic composition has been a major goal of the Quantum Chromo-Dynamics (QCD), the theory of strong interactions. The component of the nucleon spin along the direction of the nucleon momentum (helicity) can be decomposed into the contribution of nucleon constituents according to

$$S_z = \frac{1}{2} = \frac{1}{2}\Delta\Sigma + \Delta G + L_z^q + L_z^g, \tag{A.1}$$

where the three terms are the contributions from quark $\Delta\Sigma$ and gluon ΔG spins and the total angular momenta of the quarks L_z^q and gluons L_z^g, respectively.

For nearly four decades the Deep Inelastic Scattering (DIS) experiments, detecting the reaction $e^{\uparrow}p^{\uparrow} \rightarrow eX$ where polarized leptons scatter off polarized nucleon targets, has been extensively studied to unravel the helicity structure of the proton. An impressive progress in the subject was triggered by the so-called EMC spin crisis, when a much lower than expected contribution of the quarks to the nucleon spin was measured for the first time. High-precision DIS experiments at CERN (SMC) [43], SLAC (E142, E143, E155) [44, 45]

and HERA (HERMES) [46] laboratories have finally mapped the helicity distribution of charged partons in the nucleon, being able to decompose $\Delta\Sigma$ in the contributions Δq of each quark flavor q. The helicity distribution of gluons ΔG is being studied by a DIS experiment at CERN (COMPASS) and by polarized proton-proton collider experiments at BNL (STAR, PHENIX). Recently it was recognized that indirect access to the parton total angular momenta can be provided by the study of exclusive (un)polarized reactions, where all the final state products are detected. In the current experiments such a study is possible thanks to the excellent particle identification and momentum resolution in a wide kinematic range. For instance, the HERMES spectrometer is being upgraded by a recoil detector to measure the recoil proton and thus identify the complete final state of exclusive process.

In spite of the fast progresses achieved in this field, the spin tomography of the proton would be ever incomplete without the determination of the last leading–twist missing piece of the QCD description of the partonic structure of the nucleon: the transversity. The transversity distribution δq, the transverse polarization of a quark of flavor q inside a transversely polarized proton, can be regarded as the analogous of Δq but in the plane ortogonal to the momentum direction. It can not be reconstructed from the knowledge of the unpolarized distribution q and the helicity distribution Δq of the quarks. Unlike these quark distributions, the transversity δq can not be directly accessed in DIS reactions where appears always in combination with other unknown functions [47]. The history of the DIS spin physics experiments going from SLAC to CERN to HERA will end without having the possibility to map the transversity properties of the proton.

The transversity can be accessed directly only in experiments with hadron beams and detecting Drell-Yan reactions $N^{\uparrow}N^{\uparrow} \rightarrow l^{+}l^{-}X$, where a quark of one nucleon and an antiquark of the other nucleon annihilate into a lepton pair. The polarized proton-proton collider experiments at BNL has in principle the chance to measure Drell-Yan reactions, and thus transversity, but requires very high energy to struck antiquarks off a proton. At this energies the transversity effects are expected to be too small to be efficiently detected. An entirely new chapter in studies of the spin structure of the proton will unfold with the advent of the polarized antiproton capability at new hadron facilities, like the Facility for Antiproton and Ion Research (FAIR) of GSI Darmstadt. This will be outlined in the following.

A.2 The PAX project

Polarized antiprotons, produced by spin filtering with an internal polarized gas target, provide access to a wealth of single– and double–spin observables, thereby opening a new window to physics accessible at new hadron facilities. This includes a first measurement of the transversity distribution of the valence quarks in the proton, a test of the theoretical connections between observables related to the quark distribution inside a transversely polarized nucleon, in Drell–Yan as compared to DIS reactions, and a first measurement of

the moduli and the relative phase of the time–like electric and magnetic form factors $G_{E,M}$ of the proton. Still open questions in polarized and unpolarized $p\bar{p}$ elastic scattering can be addressed as well. A viable experimental set-up can be realized within the Facility for Antiproton and Ion Research (FAIR) project for a large European hadron facility, where a low-energy antiproton polarizer ring is used to yield an antiproton beam with sizable polarization. After acceleration, the polarized antiproton beam can be used to collide on a polarized internal hydrogen target (fixed target mode) or with a beam of polarized protons (collider mode). The design and performance of the new components, required for the polarized antiproton program, are outlined in the following.

A.2.1 Physical case

The polarized antiproton–proton interactions will allow a unique access to a number of new fundamental physics observables, which can not be studied without transverse polarization of protons and/or antiprotons:

- The transversity distribution is the last leading–twist missing piece of the QCD description of the partonic structure of the nucleon. It describes the quark transverse polarization inside a transversely polarized proton [47]. Unlike the more conventional unpolarized quark distribution q and the helicity distribution Δq, the transversity δq can neither be accessed in deep–inelastic scattering of leptons off nucleons nor can be reconstructed from the knowledge of q and Δq. It may contribute to some single–spin observables in DIS, but always coupled to other unknown functions. The transversity distribution is directly accessible uniquely via the double transverse spin asymmetry A_{TT} in the Drell–Yan production of lepton pairs $p^{\uparrow}\bar{p}^{\uparrow} \rightarrow l^{+}l^{-}X$, which can be interpreted as incoherent sum over the quark contributions:

$$A_{TT} \equiv \frac{d\sigma^{\uparrow\uparrow} - d\sigma^{\uparrow\downarrow}}{d\sigma^{\uparrow\uparrow} + d\sigma^{\uparrow\downarrow}} = \hat{a}_{TT} \frac{\sum_q e_q^2 \, \delta q \cdot \delta\overline{q}}{\sum_q e_q^2 \, q \cdot \overline{q}} \tag{A.2}$$

  where $d\sigma^{\uparrow\uparrow}$ ($d\sigma^{\uparrow\downarrow}$) is the measured yield for parallel (antiparallel) spin configuration and e_q is the charge of the quark flavor q. The $\hat{a}_{TT}$ factor is the calculable double-spin asymmetry of the QED elementary process $q\overline{q} \rightarrow e^{+}e^{-}$:

$$\hat{a}_{TT} = \frac{\sin^2\theta}{1+\cos^2\theta} \cos 2\phi \,, \tag{A.3}$$

  where θ and ϕ are the polar and azimuthal scattering angles, respectively.

  The theoretical expectations for A_{TT} in the Drell–Yan process with transversely polarized antiprotons interacting with a transversely polarized proton target or beam

at HESR are in the 30–40 per cent range [48, 49]; with the expected antiproton spin–filtering rate and luminosity of HESR the PAX experiment is uniquely suited for the definitive observation of δq of the proton for the valence quarks.

- The PAX measurements can also provide completely new insights into the understanding of (transverse) single–spin asymmetries (SSA) which have been observed in proton–proton and proton–antiproton collisions as well as in lepton–nucleon scattering. These asymmetries can be interpreted in term of novel mechanism involving the transverse intrinsic momentum of the partons like Sivers [50] or Collins [51]. For instance through charm production ($\bar{p}^{\uparrow}\, p \to D\, X$ or $\bar{p}\, p^{\uparrow} \to D\, X$) it will be possible to disentangle the Sivers and the Collins mechanisms. In general, both effects contribute to the measured SSA (mostly in $p^{\uparrow}\, p \to \pi\, X$ and $\bar{p}^{\uparrow}\, p \to \pi\, X$), but in the case of charm production the Collins mechanism drops out. Moreover, in conjunction with the data on SSA from the HERMES collaboration [52, 53, 54, 55], the PAX measurements of the SSA in Drell–Yan production on transversely polarized protons can for the first time provide a test of the theoretical prediction [56] of the sign–reversal of the Sivers function from semi–inclusive DIS to Drell–Yan processes. Both studies will crucially test and improve our present QCD–description of the intriguing phenomenon of SSA.

- The origin of the unexpected behavior of the ratio of the magnetic and electric form factors of the proton, as observed at the Jefferson laboratory [57] [58], can be clarified by a measurement of their relative phase, which discriminates strongly between the models for the form factor. This phase can be measured via SSA in the annihilation $\bar{p}p^{\uparrow} \to e^+e^-$ on a transversely polarized target [59, 60]. The double–spin asymmetry will fix the relative phase ambiguity and allow independently the $G_E - G_M$ separation, which will serve as a check of the traditional Rosenbluth separation in the time–like region.

- The double transverse asymmetry in $p\bar{p}$ scattering can be investigated and related with the large effects observed in the pp case [61]. Arguably, in the $p\bar{p}$ case the hard mechanisms [62, 63, 64] can be tested at momentum transfer almost twice as large as in pp scattering at the same center of mass energy, thanks to the distinguishably of the particles undergoing the reaction.

- The charge conjugation property allows direct monitoring of the polarization of antiprotons in HESR and the rate of polarization buildup constitutes a direct measurement of the transverse double spin asymmetry in the $p\bar{p}$ total cross section. This asymmetry has never been measured and its knowledge will help to clarify the origin of the discrepancy between the experimental extraction [65] and the theoretical calculations [66] usually made assuming the spin independence of forward scattering.

A.2.2 Polarized Antiprotons at FAIR

For more than two decades, physicists have tried to produce beams of polarized antiprotons [67], generally without success. Conventional methods like atomic beam sources (ABS), appropriate for the production of polarized protons and heavy ions cannot be applied, since antiprotons annihilate with matter. Polarized antiproton have been produced from the decay in flight of $\overline{\Lambda}$ hyperons at Fermilab, but the intensity of the extracted beam was far below the one reached with proton beams [68]. Scattering of antiprotons off a liquid hydrogen target could yield polarizations of $P \approx 0.2$, with even lower beam intensities [69]. Unfortunately, both approaches do not allow efficient accumulation in storage rings, which would greatly enhance the luminosity. Spin splitting using the Stern-Gerlach separation of the given magnetic substates in a stored antiproton beam was proposed in 1985 [70]. Although the theoretical understanding has much improved since then [71], spin splitting using a stored beam has yet to be observed experimentally. In contrast to that, a convincing proof of the spin-filtering principle has been produced by the FILTEX experiment at the TSR-ring in Heidelberg [72]. Based on this result, the PAX collaboration has elaborated a viable scheme which would allow to reach a polarization of the stored antiprotons at HESR of $\simeq 0.2 - 0.3$ [73, 74, 75].

The proposed approach is composed of two phases. During these the major milestones of the project can be tested and optimized before the final goal is approached: an asymmetric proton–antiproton collider, in which polarized protons with momenta of about 3.5 GeV/c collide with polarized antiprotons with momenta up to 15 GeV/c. These circulate in the HESR, which has already been approved and will serve the PANDA experiment. In the following, we will briefly describe the overall machine setup of the APR, CSR, and HESR complex, schematically depicted in Figure A.1

(i) The Antiproton Polarizer Ring (APR) has the crucial goal of polarizing antiproton to be accelerated and injected in the other rings. The polarization method is based on spin-filtering by a polarized gas target internal to the beam line. In 1992 an experiment at the Test Storage Ring (TSR) at MPI Heidelberg showed that an initially unpolarized stored 23 MeV proton beam can be polarized by spin-dependent interaction with a polarized hydrogen gas target [72]. The final polarization achieved, of only few %, was that time limited by the not optimized beam acceptance and momentum. Among the three different mechanisms were initially identified to add up to the measured result [76, 77], two are now under theoretical debate [78]. The PAX collaboration has planned a set of preparatory test-experiments to investigate these mechanisms and optimize the polarization build up in APR. Preliminary estimates indicate an achievable polarization in the range $\simeq$ 0.2–0.3.

(ii) In the Cooler Synchrotron Ring (CSR, COSY-like) protons or antiprotons can be stored with a momentum up to 3.5 GeV/c for fixed-target experiments or accelerated to be transferred to the HESR ring. This ring shall have a straight section, where

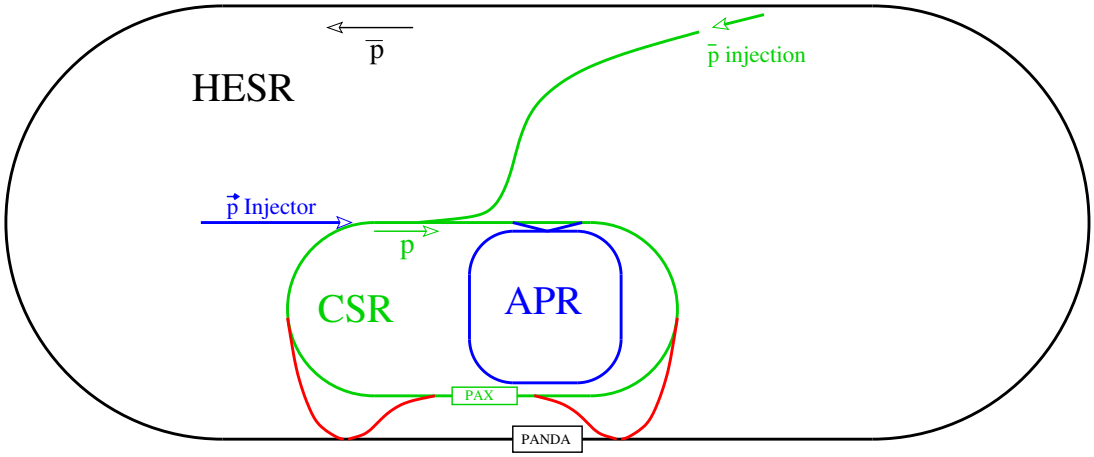

Figure A.1: The proposed accelerator set–up at the HESR (large ring), with the equipment used by the PAX collaboration in Phase–I: CSR (medium ring), APR (small polarizing ring), beam transfer lines and polarized proton injector. In Phase–II, by adding two transfer lines between CSR and HESR, both a fixed target experiment and an asymmetric collider can be set up at the PAX interaction point. (The figure is drawn to scale.)

a PAX detector could be installed, running parallel to the experimental straight section of HESR.

(iii) The HESR ring, already approved within the FAIR project to serve the PANDA experiment with antiproton up to 15 GeV/c momentum, is upgraded to become a synchrotron. By deflection of the HESR beam into the straight section of the CSR, both a fixed-target experiment with a moderate center of mass energy (s=45), or an asymmetric antiproton-proton collider with a high center of mass energy (s=200), become feasible at the PAX interaction point.

It is worthwhile to stress that, through the employment of the CSR, effectively a second interaction point is formed with minimal modifications of the HESR setup. The proposed solution opens the possibility to run two different experiments at the same time with minimal interference.

A.3 The PAX detector concept

In the following we focus on the most challenging task of the PAX physics program: the measurement of the Drell–Yan reaction to access the transversity distribution. A detector optimized for this task can be designed to be suitable to achieve also the other goals of the PAX experimental program.

In the detector concept, presented below, the following criteria have been pursued:

- be compatible with a polarized internal target in the fixed-target phase and with the asymmetric collider lattice in the high energy phase of the project. In particular any effect of the spectrometer magnet on the interaction point should be minimized (compensated) in order to not degrade the internal target (beam) polarization;

- optimize the acceptance at large angles. The double spin asymmetry of the $q\bar{q} \to \ell^+\ell^-$ QED elementary process maximizes the sensitivity of the measured asymmetry A_{TT} (and thus of the transversity distribution) for 90–degree scattering in the center-of-mass of the partonic system, where $\sin^2\theta \sim 1$, see Eq. A.3. The active area of the detector should match the azimuthal intervals where the $\cos 2\phi$ modulation of the asymmetry has the maximum. We note that also the $\overline{p}p$ elastic scattering at 90° c.m. and the form–factor measurements benefit from a large angle detector;

- trigger efficiently on the rare Drell–Yan events. At the PAX energy the few nb Drell–Yan cross section should be clearly identified from a total $\overline{p}p$ cross–section of about 50 mb;

- cope with the overwhelming background. The lepton identification should provide a rejection factor of the order of 10^4 to 10^5 against hadrons. Secondary leptons, produced in meson decays and in secondary interactions in the detector material, should be vetoed as well;

- provide of the order of 1 % resolution for the invariant mass of the lepton pairs, in order to efficiently distinguish the contribution of the resonances (J/Ψ and ψ) from the continuum;

- provide a unique facility as complete as possible and flexible to allow the study of auxiliary processes and additional physical channels which might become interesting during the next 10 years.

Physical channels

To reveal rare reactions like the Drell–Yan process and the $\overline{p}p \to l^+l^-$ annihilation, the PAX detector has to be conceived as a large acceptance apparatus capable of unambiguously identifying lepton pairs of large invariant mass and precisely measuring their momenta. The detector has to be able to measure lepton pairs with large opening angle, in a wide kinematic range with good angular and energy resolution. A clear particle identification is required to separate the leptons of the wanted processes from the large pion background.

Reactions characterized by two–body hadronic final states like elastic scattering, present a higher cross–section and put less stringent constraints on the detector design. They can be identified by measuring scattering angles and momenta of the hadronic particles by employing complanarity and total momentum conservation.

Particle Identification

The Drell–Yan production rate is of the order of 10^{-7} of the total $\overline{p}p$ reaction rate and results in a low yield of the e^+e^- signal per interaction. In order to maximize the dilepton detection efficiency, the PAX spectrometer must provide a large geometrical acceptance. At the same time, the high interaction rate (of the order of 1 MHz) together with the hadron multiplicity represents a serious challenge to the trigger system which has to select the events containing the lepton tracks. An accurate lepton identification can only be achieved by detectors which are highly insensitive to the large flux of hadrons. In order to minimize the background from lepton misidentification at a typical prevailing e/π ratio of 10^{-4}, redundant recognition of lepton tracks is essential. For the considered range of momenta (between 0.5 and 10 GeV/c) electrons offer the advantage with respect to muons of that they can be identified in a hadron blind gas threshold Čerenkov detector. This device can be operated on a fast time scale to meet the stringent trigger requirements in the high–rate high–multiplicity environment. Additional discrimination against pions can be provided both by the cluster lateral profile in the electromagnetic calorimeter (CAL) and by the E/p ratio between the energy E measured in the CAL and the momentum p measured in the spectrometer. With these constraints, the required rejection factor of the order of 10^{10} against hadronic events (corresponding to 10^5 for single track events) is achievable, as demonstrated in other experiments [79, 80].

In order to best match the above requirements, the PAX detector is designed to measured electron–positron pairs of large invariant mass.

A.3.1 Overview of the PAX spectrometer

The PAX large-acceptance spectrometer, sketched in Figure A.2, is optimized to detect electromagnetic final states with two charged tracks of high invariant mass. A clear identification of electrons is required to separate scattered electrons of the Drell–Yan mechanism from the large π background. The detector is designed to also detect two–body hadron reactions using kinematical constraints, i.e. complanarity and total momentum conservation. Moreover it can measure the energy of gammas from radiative processes and π^0 and η decays.

The tracking magnet of the detector is a eight coils superconducting toroid covering zenithal angles from 20° to 135° and with an azimuthal acceptance above 80%. The detectors are arranged in an azimuthally eight–fold segmented, frustum–like geometry.

The very inner part of the detector is devoted to triggering and tracking of charged particles. The scattering angles as well as the initial trajectory for the determination of the particle's momentum are measured by a compact vertex tracking system consisting of three layers of double–sided silicon strip detectors (SiD). The momentum measurement is completed by two sets of conventional drift chambers behind the magnet (DC). A possible additional set of drift chambers inside the magnet (MC) would improve the matching between the inner and outer tracks and help to resolve multiple tracks and to identify

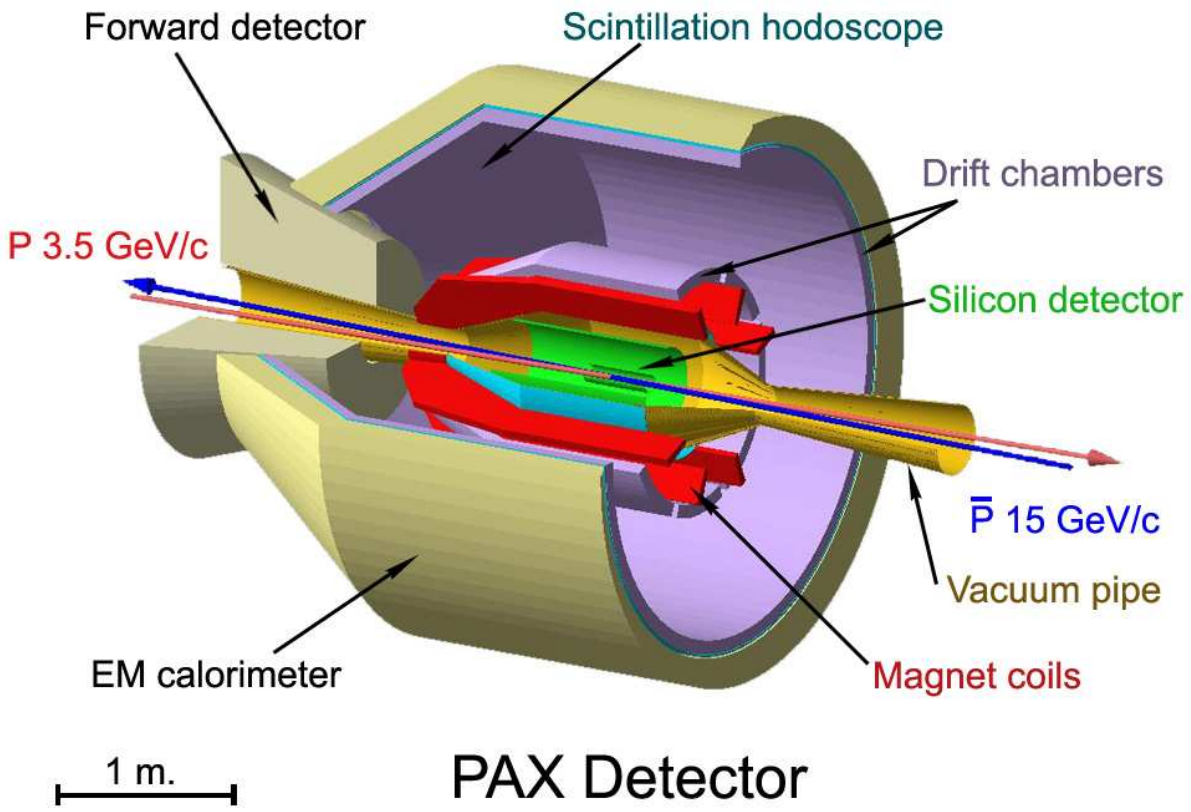

Figure A.2: Artists view of the PAX spectrometer.

gamma conversions. This will allow us to detect low–momentum tracks which do not reach the external section of the spectrometer.

A threshold Čerenkov counter (CER) provides trigger capability for electrons and positrons produced in Drell–Yan processes. The Čerenkov detector is placed outside the magnet, in between the two sets of drift–chamber, fitting the $0.6 - 0.8$ m tracking arm required to obtain the ~ 1 % momentum resolution with a typical spatial resolution of ~ 200 μm. Electron and photon energies and directions are measured by the CAL. Both the CER and the CAL provide fast response and can be employed in the selection of electromagnetic particles to obtain a π/e rejection factor $\lesssim 100$ at trigger level and larger than 10^4 in the off–line analysis for a single track. A pre–shower detector (PS) can possibly be added in front of the calorimeter to improve the pion rejection and the resolution on the impact point of photons.

The detector is designed to assure full acceptance between $\pm 20^0$ and $\pm 130^0$ for polar angles in the laboratory frame. In the present design, no real limit exists for the maximum acceptable polar angle: the above values can be taken as indicative and can be easily

adapted to match different beam configurations. The detectors point toward the central part of the interaction region in a projective geometry.

A.3.2 Detector Phase–I

The fixed–target program of Phase-I concentrates on reactions with 2-body final states, i.e. the time–like proton form factors and elastic scattering measurements. During Phase-II the physics program concentrates on the Drell-Yan measurement at medium center of mass energies (s=45) to access the transversity partonic distribution. The simple and over-constraint kinematics of 2-body events puts less stringent requirements on the detector performance. The momentum resolution, as an example, is not a crucial issue, as demonstrated by the E835 experiment [79]. Such measurements can start even before the detector is completed and can be used to test and optimize each of the sub–systems, i.e. tracking system and Čerenkov PID. In case of 2-body reactions the trigger is provided by two back–to–back tracks. The Čerenkov signals above threshold and the total energy deposited in the calorimeter equal to the center–of–mass energy, can be employed to trigger the rare electron events. At the CSR energies, the outgoing particles have an almost isotropic distribution and a momentum between 0.5 and 1.5 GeV/c. Hadron identification can be provided by time–of–flight measurement using the hodoscopes.

In fixed-target mode the typical luminosity is of the order of 10^{31} cm^{-2}s^{-1}. From the $p\overline{p} \to e^+e^-$ cross-section measured by PS170 [80], it is estimated that the proton time-like form factors can be measured in a relatively short time, from less than 1 day up to few weeks. Only the most challenging measurement of double polarized asymmetry at the highest energy requires few months of data-taking. From the cross-section measured by E838 [81], it is estimated that the most challenging double-polarized measurement in $\overline{p}p$ elastic scattering requires only few hours of data-taking to reach a precision of 0.05 at the maximum transverse momentum achievable in CSR (GeV^2/c^2).

A.3.3 Detector Phase–II

During Phase–II of the PAX physics program, the asymmetric–collider is used to achieve high energies and a complete mapping of the transversity in the quark valence region. The inclusive $\overline{p}p \to e^+e^-X$ Drell–Yan process has poor kinematic constraints. The intrinsic transverse momentum of the quarks, for instance, breaks the complanarity of the e^+e^- pair. A rejection factor of 10^3 against background events is required to reduce the rate from a few MHz to kHz levels. The trigger asks for two tracks in opposite hemispheres above the Čerenkov threshold. To reduce low–energetic combinatorial background, a cut on the dilepton invariant mass is applied using the deposited energy and the impact point at the calorimeter. The first layer of silicon is used to veto gamma conversions.

The major sources of background to the Drell–Yan process are the combinatorial background from meson Dalitz-decays and gamma conversions. Gamma conversions are vetoed

requiring a charged hit in the first silicon layer. The residual background can be studied and finally subtracted by investigating wrong-charge candidates (control sample). Charm background can be studied and eventually reduced by reconstructing the secondary vertex of the decay with the silicon detector [82]. The background by particle misidentification can be assumed to be negligible since the PAX detector is designed to provide redundant high-level information about the particle type. Preliminary results based on GEANT simulation show that the signal over background ratio is of the order of one *before* combinatorial background subtraction, and support the view that the background for the e^+e^- Drell-Yan measurement is well under control. Conventional tracking detectors can provide a resolution better than 2 % in dilepton invariant mass: this is sufficient to efficiently distinguish resonance from continuum contributions and to investigate the δq dependence on the relevant kinematic variables. During one year of data-taking, the most interesting valence region can be explored and the δq transverse distribution can be measured with a precision better than 10 % [75].

Appendix B

The HERMES gas target

This short overview deals primarily with the use of polarized hydrogen atoms as nuclear targets. A polarized gas target is an atomic gas which nuclei have the spin oriented with respect to a polarization axis defined by magnetic field. Nuclear polarization, the interaction between nuclear and electron spins and spin separation are relevant atomic physics principles involved in the realization of polarized gas targets. They are shortly introduced and an example of an existing gas target (the HERMES one) is then briefly illustrated.

Nuclear polarization

The polarization of an ensemble of spin $\frac{1}{2}$ particles, i.e. protons, is described by a polarization vector. The component of polarization along one axis (z) is definite as:

$$P_z = n_+ - n_- \qquad \text{where} \quad n_\pm = \frac{N_\pm}{N_+ + N_-} \tag{B.1}$$

where n_+ and n_- are the fraction of particles with spin I along zeta ($m_I = \frac{1}{2}$) and opposite to zeta ($m_I = \frac{1}{2}$) respectively. Usually the atoms of a polarized gas target are located in an external field, in that case the polarization vector is along the guide field, often called holding field.

Couping of nuclear and electron spins in hydrogen

The nuclear spin used for gas polarized targets is coupled with the spin of the electron in the neutral atoms. The external magnetic field **B** is defined 'weak' or 'strong' compared to the critical field $\mathbf{B_c}$ equal to 50.7 mT for hydrogen. In terms of the electron ($\Uparrow$) and nuclear ($\uparrow$) spin states the four hyperfine states of hydrogen are:

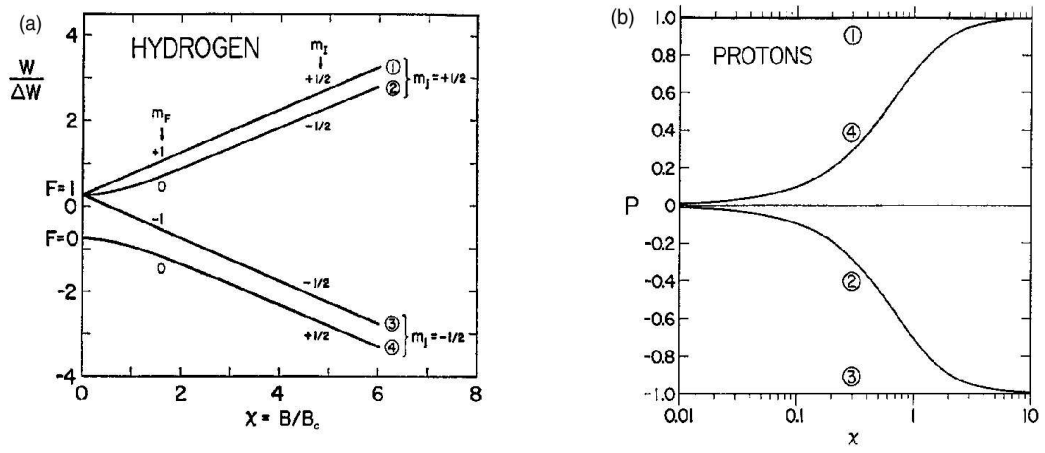

Figure B.1: Energy (a) and nuclear polarization (b) of the four hyperfine states for hydrogen as a function of the external magnetic (holding) field $\mathbf{B}$*, given in relative units* $\chi = \mathbf{B}/\mathbf{B_c}$ *with* $\mathrm{B_c} = 50.7$ mT. ΔW *is the hyperfine splitting*

$$
\begin{aligned}
|1\rangle &= |\Uparrow,\uparrow\rangle,\\
|2\rangle &= \cos\theta\ |\Uparrow,\downarrow\rangle + \sin\theta\ |\Downarrow,\uparrow\rangle,\\
|3\rangle &= |\Downarrow,\downarrow\rangle,\\
|4\rangle &= \cos\theta\ |\Downarrow,\uparrow\rangle + \sin\theta\ |\Uparrow,\downarrow\rangle
\end{aligned}
$$

where the mixing angle θ is defined in terms of the external field $\mathbf{B}$ and the critical field by the relation

$$\tan\theta = \frac{\mathbf{B_c}}{\mathbf{B}} \tag{B.2}$$

The states 1 and 3 are referred as pure spin states, while the states 2 and 4 as mixed states.

The energy of the four states of hydrogen as a function of $\chi = \mathbf{B}/\mathbf{B_c}$ is shown in Figure B.1. the energy difference between states 1 and 2 or states 3 and 4 is caused by the hyperfine interaction. In a weak magnetic field the electron spin J and the nuclear spin I couple to total angular momentum F. For the mixed states (that have $\mathbf{m_F} = \mathbf{0}$, i.e. states 2 and 4) in a weak field the electron and proton spins precess one about the other so that they have zero magnetic moment and zero nuclear polarization, as shown in Figure B.1(b).

In a strong external field i.e if $\chi \gg 1$, electron and proton spins are decoupled. the proton polarization reaches $\mathrm{P} = \pm 1$ asymptotically and the magnetic moment of the atom approaches μ_B the electron moment. For intermediate fields the polarization of the two 'pure' spin states is $|\mathrm{P}| = 1$ independently of the field strength, while the polarization of the mixed states is given by $|\mathrm{P}| = \pm\chi\sqrt{1+\chi^2}$ It is clear that injecting only one pure state requires a lower holding field.

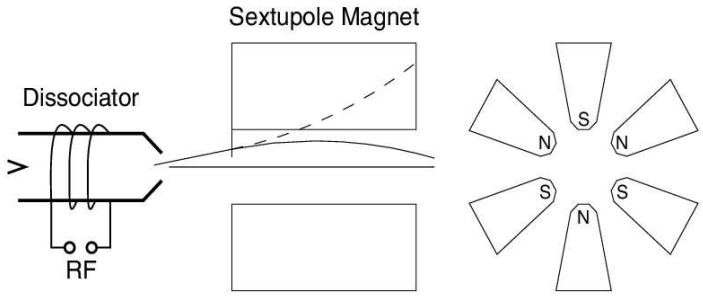

Figure B.2: Schematic of atomic beam spin separation. Atoms with $m_j = +\frac{1}{2}$ are deflected toward the axis (continuous line), while the ones with $m_j = -\frac{1}{2}$ are rejected (dashed line)

Spin separation

in an inhomogeneous magnetic field atoms are driven towards or away from the high field regions by Stern Gerlach separation, depending on whether their energy decreases or increases with increasing B. Thus, if a beam of hydrogen atoms is directed along the axis of a multipole magnet, i.e. a sextupole, atoms are with $m_j = +\frac{1}{2}$ (states 1 and 2) are deflected toward the axis of the magnet, while atoms with $m_j = -\frac{1}{2}$ (states 3 and 4) are rejected (see Figure B.2). The focalization of the polarized H gas targets are based primarily on this method. It has to be noticed how the spin rejection acts on the electron spin ion all these processes, not on the nuclear spin.

B.1 The HERMES target

The HERMES gaseous target setup which ran since 1995 to 2000 in the HERA lepton storage ring is an example of an internal target. This target setup has the advantages of being almost free of dilution (is close to 1), of providing a high degree of polarization (greater than 0.8), and of being able to invert the direction of the spin of the nucleons within milliseconds. The HERMES polarized gas target [83], schematically shown in Figure B.3, consists of an Atomic Beam Source (ABS) [84] which produces a polarized jet of atomic hydrogen or deuterium and focuses it into a thin-walled storage cell along the beam line [85].

The atomic gas is produced in a dissociator and is formed into a beam using a cooled nozzle, collimators and a series of differential pumping stations. A succession of magnetic sextupoles and radio-frequency fields are used to select (by Stern-Gerlach separation) and exchange (by radio-frequency transitions) the atomic hyperfine states that have a given nuclear polarization to be injected into the cell through a 1 *cm* diameter injection tube. The number of atoms per second that the atomic beam source focalize into the injection tube is called the atomic beam intensity I_{IBS}. The atomic flux is accumulated in an ac-

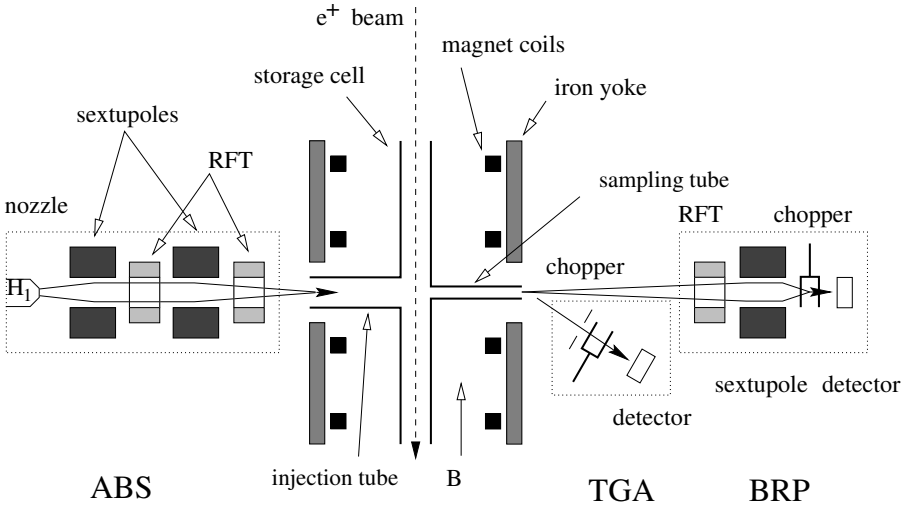

Figure B.3: Schematic view of the HERMES longitudinally polarized target. From left to right: Atomic Beam Source (ABS), the injection tube by which the focalized atoms enter the storage cell, the sampling tube that connects the diagnostic system composed by Target Gas Analyzer (TGA) and Breit Raibi Polarimeter (BRP). The accumulation cell and the target magnet are placed on the HERA beam pipe. The location of the radio frequency units (RFT) are indicated.

cumulation cell, a windowless 40 cm long elliptical tube coaxial to the beam, with 75 μm thick Al walls coated to inhibit the gas-surface interaction and then pumped out by the acceleration ring pumping system since the cell is part of the HERA beam pipe. The use of the storage cell technique results in a typical areal density increase of about two orders of magnitude compared to a free jet target. A sample of gas (ca. 5%) diffuses from the middle of the cell into a Breit-Rabi Polarimeter (BRP) [86] which measures the atomic polarization, or into a Target Gas Analyzer (TGA) [87] which measures the atomic and the molecular content of the sample. Both sample measurements are performed with a rate of the order of seconds. A magnet surrounding the storage cell provides a holding field defining the polarization axis and prevents spin relaxation via spin exchange or wall collisions by effectively decoupling the magnetic moments of electrons and nucleons. A gaseous helium cooling system allows to keep the cell temperature to the lowest value for which atomic recombination and spin relaxation during wall collisions are minimal. The target polarization is randomly chosen each 60 s for hydrogen and 90 s for deuterium, after having been measured by the diagnostic system. The rapid cycling of the target polarization allows almost simultaneous data taking of different spin configurations, reducing the systematic uncertainty in the measured spin asymmetries related to the stability of the experimental setup.

List of Figures

List of Tables

Bibliography

[1] For a list of publication please visit the HERMES web site http://www-hermes.desy.de.

[2] For a list of publication please visit the COMPASS web site http://wwwcompass.cern.ch/compass/.

[3] For a list of publication please visit the PHENIX web site http://www.phenix.bnl.gov/.

[4] For a list of publication please visit the STAR web site http://www.star.bnl.gov/.

[5] For a list of publication please visit the HALL-A JLAB web site http://hallaweb.jlab.org/.

[6] For a list of publication please visit the HALL-B JLAB web site http://www.jlab.org/Hall-B/.

[7] For a list of publication please visit the HALL-C JLAB web site http://www.jlab.org/Hall-C/.

[8] For a list of PAX collaboration meetings, conference presentations, QCD–PAC and STI reports, please visit the PAX web–site at http://www.fz-juelich.de/ikp/pax.

[9] "Smile loi," "http://www.fz-juelich.de/ikp/pax/public_files/LOItoCERN.pdf".

[10] M. Capiluppi *et al.*, "A high intensity superconducting atomic beam source," *IEEE Transactions on Applied Superconductivity*, vol. Vol 15, 2005. Poster presented by Marco Statera at ASC04.

[11] F. Gautheron *et al.*, "The compass polarized target," Prepared for 16th International Spin Physics Symposium (SPIN 2004), Trieste, Italy, 10-16 Oct 2004.

[12] E. Steffens and W. Haeberli, "Polarized gas targets," *Rep. Prog. Phys.*, vol. 66, pp. 1887–1935, 2003.

[13] M. Capiluppi, G. Ciullo, M. Contalbrigo, P. F. Dalpiaz, P. Lenisa, M. Stancari, and M. Statera 2003. http://www.fe.infn.it/spinfe/MolPol2003/talks/stancari.ps.

[14] S. Atutov, L. Barion, M. Contalbrigo, G. Ciullo, P. F. Dalpiaz, F. Giordano, P. Lenisa, M. Statera, M. Stancari, and M. Wang, "Estimate of intra beam stancari," *SPIN04 proceedings*, 2005.

[15] W. Haeberli, "Sources of polarized ions," *Ann. Rev. Nucl. Part. Sci.*, vol. 17, pp. 373–426, 1967.

[16] N. Koch, *A study on the production of intense cold atomic beams for polarized hydrogen and deuterium targets*. PhD thesis, 1999.

[17] P. J. Lee, "Superconducting materials development - current status and future directions: Lts," *Applied Superconductivity Conference 2004, short course*, 2004.

[18] N. Reali, "Realizzazione di un magnete sestupolare superconduttore da inserirsi nel sistema ottico di un bersaglio di protoni polarizzati ad alta intensitá," Master's thesis, 1995.

[19] R. A. Haerfer, *Cryopumping: theory and practice*. Oxford science publications, 1981.

[20] G. K. White, *experimental techniques in low temperature physics*. Oxford, 1979.

[21] M. Capiluppi *et al.*, "A test bench for small multipolar magnets for a high-intensity superconducting atomic beam source," *IEEE Transactions on Applied Superconductivity*, 2006. Accepted. Poster presented by Marco Statera at MT19.

[22] R. Fabbri, M. Stancari, and M. Statera, "Measurement of a superconducting magnet," Tech. Rep. INFN-FE-02-01, INFN, 2002.

[23] V. Fields, "User manual," see also http://www.vectorfields.com.

[24] M. Capiluppi, G. Ciullo, M. Contalbrigo, P. F. Dalpiaz, D. Reggiani, M. Statera, and M. Stancari, "Sextupole room temperature field measurement," tech. rep.

[25] S. Eidelman *et al.*, "Review of Particle Physics," *Physics Letters B*, vol. 592, 2004.

[26] M. Statera, "First studies on a gaseous polarized hydrogen target magnet for the hermes recoil detector:conceptual design," tech. rep., INFN, 2004.

[27] A. Airapetian *et al.*, "The hermes polarized hydrogen and deuterium gas target in the hera electron storage ring," *Nucl. Instrum. Meth.*, vol. A540, pp. 68–101, 2005.

[28] A. Kugler *et al.*, "Particle identification at hades," *Nucl. Phys.*, vol. A734, pp. 78–81, 2004.

[29] A. J. Street *et al.*, "Final site assembly and testing of the superconducting toroidal magnet for the cebaf large acceptance spectrometer (clas)," *IEEE Trans. Magnetics*, vol. 32, pp. 2074–2076, 1996.

[30] R. Alarcon, "The mit-bates large acceptance spectrometer toroid," *Nucl. Phys.*, vol. A721, pp. 1075–1078, 2003.

[31] ATLAS collaboration, "Atlas end-cap toroids: Technical design report," CERN-LHCC-97-20.

[32] ATLAS collaboration, "Atlas barrel toroid: Technical design report," CERN-LHCC-97-19.

[33] A. Kawachi *et al.*, "The superconducting toroidal spectrometer for hypernuclear studies at kek-ps," *Nucl. Instrum. Meth.*, vol. A416, pp. 253–262, 1998.

[34] K. Okuno, A. Shikov, and N. Koizumi, "Superconducting magnet system in a fusion reactor," *Journal of Nuclear Materials*, vol. Volumes 329-333, pp. 141–147, August 2004.

[35] Y. Lee, H. Ahn, C. Choi, J. Sa, and S. Lee, "Structural analysis of the kstar toroidal field magnet system," *Fusion Engineering and Design*, vol. Volumes 66-68, pp. 1195–1199, 2003.

[36] H. Hayashi, K. Tsutsumi, K. Funaki, M. Iwakuma, K. Tasaki, Y. Sumiyoshi, and M. Tezuka, "Design study of a 1 gj class hts-smes (1): Conceptual design of a magnet system," *Physica C: Superconductivity*, pp. Pages 1327–1331, August 2001.

[37] C. A. Luongo, "Optimization of toroidal superconducting magnetic energy storage magnets," *Physica C: Superconductivity*, pp. Pages 110–114, May 2001.

[38] R. M. Scanlan, D. R. Dietderich, and S. A. Gourlay, "A new generation nb_3sn wire, and the prospects for its use in particle accelerators," *AIP Conf. Proc.*, vol. 711, pp. 349–358, 2004.

[39] J. Parrell, M. Field, Y. Zhang, and S. Hong, "nb_3sn conductor development for fusion and particle accelerator applications," *Advances in Cryogenic Engineering: Transaction of the International Cryogenics Materials Conference - ICMC*, vol. 50, pp. 369–375, 2004.

[40] T. Kate, "The atlas superconducting magnet system: Status of integration and installation," *IEEE Transaction on Applied Superconductivity.* in pubblication.

[41] B. Maddock and G. James in *IEEE Proceedings*, vol. 115(4), p. 543, 1968.

[42] R. F. Barron, *Cryogenics Systems.* Oxford science, 1985.

[43] B. Adeva *et al.*, "Spin asymmetries a(1) of the proton and the deuteron in the low x and low q**2 region from polarized high energy muon scattering," *Phys. Rev.*, vol. D60, p. 072004, 1999.

[44] K. Abe *et al.*, "Measurements of the proton and deuteron spin structure functions g1 and g2," *Phys. Rev.*, vol. D58, p. 112003, 1998.

[45] P. L. Anthony *et al.*, "Measurements of the q**2 dependence of the proton and neutron spin structure functions g1(p) and g1(n)," *Phys. Lett.*, vol. B493, pp. 19–28, 2000.

[46] K. P. C. et al, "Spin-exchange optical pumping as a source of spin-polarized atomic deuterium," *Phys. Rev. Lett.*, vol. 68, pp. 174–177, 1992.

[47] V. Barone, A. Drago, and P. G. Ratcliffe, "Transverse polarisation of quarks in hadrons," *Phys. Rept.*, vol. 359, pp. 1–168, 2002.

[48] M. Anselmino, V. Barone, A. Drago, and N. N. Nikolaev, "Accessing transversity via j/psi production in polarized p(pol.) anti-p(pol.) interactions," *Phys. Lett.*, vol. B594, pp. 97–104, 2004.

[49] A. V. Efremov, K. Goeke, and P. Schweitzer, "Transversity distribution function in hard scattering of polarized protons and antiprotons in the pax experiment," *Eur. Phys. J.*, vol. C35, pp. 207–210, 2004.

[50] G. P. Ramsey and D. W. Sivers, "Spin observables for n n $\rightarrow$ n n at large momentum transfer," *Phys. Rev.*, vol. D45, pp. 79–91, 1992.

[51] J. C. Collins, "Fragmentation of transversely polarized quarks probed in transverse momentum distributions," *Nucl. Phys.*, vol. B396, pp. 161–182, 1993.

[52] A. Airapetian *et al.*, "Observation of a single-spin azimuthal asymmetry in semi-inclusive pion electro-production," *Phys. Rev. Lett.*, vol. 84, pp. 4047–4051, 2000.

[53] K. Abe *et al.*, "Search for time-dependent b/s0 anti-b/s0 oscillations using a vertex charge dipole technique," *Phys. Rev.*, vol. D67, p. 012006, 2003.

[54] A. Airapetian *et al.*, "Single-spin azimuthal asymmetries in electroproduction of neutral pions in semi-inclusive deep-inelastic scattering," *Phys. Rev.*, vol. D64, p. 097101, 2001.

[55] A. Airapetian *et al.*, "Single-spin asymmetries in semi-inclusive deep-inelastic scattering on a transversely polarized hydrogen target," *Phys. Rev. Lett.*, vol. 94, p. 012002, 2005.

[56] J. C. Collins, "Leading-twist single-transverse-spin asymmetries: Drell-yan and deep-inelastic scattering," *Phys. Lett.*, vol. B536, pp. 43–48, 2002.

[57] J. Gao *et al.*, "Dynamical relativistic effects in quasielastic 1p shell knockout," *Phys. Rev. Lett.*, vol. 84, pp. 3265–3269, 2000.

[58] O. Gayou *et al.*, "Measurements of the elastic electromagnetic form factor ratio mu pgep/gmp via polarization transfer," *Phys. Rev.*, vol. C64, p. 038202, 2001.

[59] A. Z.Dubnickova, S. Dubnicka, and M. P. Rekalp *Nuovo. Cim.*, vol. A 109, p. 241, 1966.

[60] S. J. Brodsky, C. E. Carlson, J. R. Hiller, and D. S. Hwang, "Single-spin polarization effects and the determination of timelike proton form factors," *Phys. Rev.*, vol. D69, p. 054022, 2004.

[61] D. G. Crabb *et al.*, "Spin dependence of high p-transverse**2 elastic p p scattering," *Phys. Rev. Lett.*, vol. 41, p. 1257, 1978.

[62] M. Matveev *et al. Lett. Nuovo Cimento*, vol. 7, p. 719, 1972.

[63] S. J. Brodsky and G. R. Farrar, "Scaling laws at large transverse momentum," *Phys. Rev. Lett.*, vol. 31, pp. 1153–1156, 1973.

[64] S. J. Brodsky, J. Rathsman, and C. Merino, "Odderon-pomeron interference," *Phys. Lett.*, vol. B461, pp. 114–122, 1999.

[65] T. A. Armstrong *et al.*, "Precision measurements of anti-proton proton forward elastic scattering parameters in the 3.7-gev/c to 6.2-gev/c region," *Phys. Lett.*, vol. B385, pp. 479–486, 1996.

[66] P. Kroll and W. Schweiger, "Analysis of low-energy anti-proton - proton forward scattering," *Nucl. Phys.*, vol. A503, p. 865, 1989.

[67] A. D. Krisch, A. M. T. Lin, and O. Chamberlain, "Polarized beams at ssc. proceedings, workshop, ann arbor, usa, june 10-15, 1985. polarized anti-protons. proceedings, workshop on polarized anti-proton sources, bodega bay, usa, april 18-21, 1985," NEW YORK, USA: AIP (1986) 251 P. (AIP CONFERENCE PROCEEDINGS, 145). (PARTICLES AND FIELDS SERIES, 34).

[68] D. P. Grosnick *et al.*, "The design and performance of the fnal high-energy polarized beam facility," *Nucl. Instrum. Meth.*, vol. A290, p. 269, 1990.

[69] D. L. Adams *et al.*, "Measurement of single spin asymmetry for direct photon production in p p collisions at 200-gev/c," *AIP Conf. Proc.*, vol. 343, pp. 404–411, 1995.

[70] T. O. Niinikoski and R. Rossmanith, "Selfpolarization of protons in storage rings," *Nucl. Instrum. Meth.*, vol. A255, pp. 460–465, 1987.

[71] P. Cameron *et al.*, "The relativistic stern-gerlach interaction as a tool for attaining the spin separation," *AIP Conf. Proc.*, vol. 675, pp. 781–785, 2003.

[72] F. Rathmann *et al.*, "New method to polarize protons in a storage ring and implications to polarize anti-protons," *Phys. Rev. Lett.*, vol. 71, pp. 1379–1382, 1993.

[73] F. Rathmann *et al.*, "A method to polarize stored antiprotons to a high degree," *Phys. Rev. Lett.*, vol. 94, p. 014801, 2005.

[74] F. Rathmann and P. Lenisa, "Spin physics at gsi," 2004.

[75] V. Barone *et al.*, "Antiproton proton scattering experiments with polarization," 2005.

[76] H. O. Meyer", "Effect of a polarized hydrogen target on the polarization of a stored proton beam," *"Phys. Rev."*, vol. E50, 1994.

[77] C. J. Horowitz and H. O. Meyer", "Polarizing stored beams by interaction with polarized electrons," *"Phys. Rev. Lett."*, vol. 72.

[78] A. I. Milstein and V. M. Strakhovenko, "Polarizing mechanisms for stored p and anti-p beams interacting with a polarized target," *Phys. Rev.*, vol. E72, p. 066503, 2005.

[79] M. Ambrogiani *et al.*, "Measurements of the magnetic form factor of the proton in the timelike region at large momentum transfer," *Phys. Rev.*, vol. D60, p. 032002, 1999.

[80] G. Bardin *et al.*, "A large solid angle magnetic detector for precision studies of e.m. processes in low-energy anti-p interactions," *Nucl. Instrum. Meth.*, vol. A259, pp. 376–388, 1987.

[81] C. G. White *et al.*, "Comparison of 20 exclusive reactions at large t," *Phys. Rev.*, vol. D49, pp. 58–78, 1994.

[82] B. Aubert *et al.*, "Search for d0 - anti-d0 mixing using semileptonic decay modes," *Phys. Rev.*, vol. D70, p. 091102, 2004.

[83] A. Airapetian *et al.*, "The hermes polarized hydrogen and deuterium gas target in the hera electron storage ring," *Nucl. Instrum. Meth.*, vol. A540, p. 68, 2005.

[84] C. Baumgarten *et al.*, "The hermes polarized atomic beam source," *Nucl. Instrum. Meth.*, vol. A505, p. 633, 2003.

[85] C. Baumgarten *et al.*, "The storage cell of the polarized h/d internal gas target of the hermes experiment at hera," *Nucl. Instrum. Meth.*, vol. A496, p. 277, 2003.

[86] C. Baumgarten *et al.*, "An atomic beam polarimeter to measure the nuclear polarization in the hermes gaseous polarized hydrogen and deuterium target," *Nucl. Instrum. Meth.*, vol. A482, pp. 606–618, 2002.

[87] C. Baumgarten *et al.*, "A gas analyzer for the internal polarized target of the hermes experiment," *Nucl. Instrum. Meth.*, vol. A508, p. 268, 2003.